ISSN 1881-7815 Online ISSN 1881-7823

BST BioScience Trends

Volume 16, Number 4
August, 2022

IRCA BSSA

IACMHR

www.biosciencetrends.com

BST
BioScience Trends

ISSN: 1881-7815
Online ISSN: 1881-7823
CODEN: BTIRCZ
Issues/Year: 6
Language: English
Publisher: IACMHR Co., Ltd.

BioScience Trends is one of a series of peer-reviewed journals of the International Research and Cooperation Association for Bio & Socio-Sciences Advancement (IRCA-BSSA) Group. It is published bimonthly by the International Advancement Center for Medicine & Health Research Co., Ltd. (IACMHR Co., Ltd.) and supported by the IRCA-BSSA.

BioScience Trends devotes to publishing the latest and most exciting advances in scientific research. Articles cover fields of life science such as biochemistry, molecular biology, clinical research, public health, medical care system, and social science in order to encourage cooperation and exchange among scientists and clinical researchers.

BioScience Trends publishes Original Articles, Brief Reports, Reviews, Policy Forum articles, Communications, Editorials, News, and Letters on all aspects of the field of life science. All contributions should seek to promote international collaboration.

Editorial Board

Editor-in-Chief:

Norihiro KOKUDO
National Center for Global Health and Medicine, Tokyo, Japan

Co-Editors-in-Chief:

Xue-Tao CAO
Nankai University, Tianjin, China
Takashi KARAKO
National Center for Global Health and Medicine, Tokyo, Japan

Senior Editors:

Tetsuya ASAKAWA
The Third People's Hospital of Shenzhen, Shenzhen, China
Xunjia CHENG
Fudan University, Shanghai, China
Yoko FUJITA-YAMAGUCHI
Beckman Research Institute of the City of Hope, Duarte, CA, USA
Jianjun GAO
Qingdao University, Qingdao, China
Na HE
Fudan University, Shanghai, China
Hongen LIAO
Tsinghua University, Beijing, China
Misao MATSUSHITA
Tokai University, Hiratsuka, Japan
Fanghua QI
Shandong Provincial Hospital, Ji'nan, China
Ri SHO
Yamagata University, Yamagata, Japan
Yasuhiko SUGAWARA
Kumamoto University, Kumamoto, Japan
Ling WANG
Fudan University, Shanghai, China

Web Editor:

Yu CHEN
The University of Tokyo, Tokyo, Japan

Proofreaders:

Curtis BENTLEY
Roswell, GA, USA
Thomas R. LEBON
Los Angeles, CA, USA

Editorial and Head Office

Pearl City Koishikawa 603,
2-4-5 Kasuga, Bunkyo-ku, Tokyo 112-0003, Japan
E-mail: office@biosciencetrends.com

BioScience Trends

Editorial and Head Office

Pearl City Koishikawa 603, 2-4-5 Kasuga, Bunkyo-ku,
Tokyo 112-0003, Japan

E-mail: office@biosciencetrends.com
URL: www.biosciencetrends.com

Editorial Board Members

Girdhar G. AGARWAL
(Lucknow, India)
Hirotsugu AIGA
(Geneva, Switzerland)
Hidechika AKASHI
(Tokyo, Japan)
Moazzam ALI
(Geneva, Switzerland)
Ping AO
(Shanghai, China)
Hisao ASAMURA
(Tokyo, Japan)
Michael E. BARISH
(Duarte, CA, USA)
Boon-Huat BAY
(Singapore, Singapore)
Yasumasa BESSHO
(Nara, Japan)
Generoso BEVILACQUA
(Pisa, Italy)
Shiuan CHEN
(Duarte, CA, USA)
Yi-Li CHEN
(Yiwu, China)
Yuan CHEN
(Duarte, CA, USA)
Naoshi DOHMAE
(Wako, Japan)
Zhen FAN
(Houston, TX, USA)
Ding-Zhi FANG
(Chengdu, China)
Xiao-Bin FENG
(Beijing, China)
Yoshiharu FUKUDA
(Ube, Japan)
Rajiv GARG
(Lucknow, India)
Ravindra K. GARG
(Lucknow, India)
Makoto GOTO
(Tokyo, Japan)
Demin HAN
(Beijing, China)
David M. HELFMAN
(Daejeon, Korea)
Takahiro HIGASHI
(Tokyo, Japan)
De-Fei HONG
(Hangzhou, China)
De-Xing HOU
(Kagoshima, Japan)
Sheng-Tao HOU
(Guanzhou, China)
Xiaoyang HU
(Southampton, UK)
Yong HUANG
(Ji'ning, China)
Hirofumi INAGAKI
(Tokyo, Japan)
Masamine JIMBA
(Tokyo, Japan)
Chun-Lin JIN
(Shanghai, China)
Kimitaka KAGA
(Tokyo, Japan)
Michael Kahn
(*Duarte, CA, USA*)
Kazuhiro KAKIMOTO
(Osaka, Japan)
Kiyoko KAMIBEPPU
(Tokyo, Japan)
Haidong KAN
(Shanghai, China)
Bok-Luel LEE
(Busan, Korea)
Mingjie LI
(St. Louis, MO, USA)
Shixue LI
(Ji'nan, China)
Ren-Jang LIN
(Duarte, CA, USA)
Lianxin LIU
(Hefei, China)
Xinqi LIU
(Tianjin, China)
Daru LU
(Shanghai, China)
Hongzhou LU
(Guanzhou, China)
Duan MA
(Shanghai, China)
Masatoshi MAKUUCHI
(Tokyo, Japan)
Francesco MAROTTA
(Milano, Italy)
Yutaka MATSUYAMA
(Tokyo, Japan)
Qingyue MENG
(Beijing, China)
Mark MEUTH
(Sheffield, UK)
Michihiro Nakamura
(*Yamaguchi, Japan*)
Munehiro NAKATA
(Hiratsuka, Japan)
Satoko NAGATA
(Tokyo, Japan)
Miho OBA
(Odawara, Japan)
Xianjun QU
(Beijing, China)
John J. ROSSI
(Duarte, CA, USA)
Carlos SAINZ-FERNANDEZ
(Santander, Spain)
Yoshihiro SAKAMOTO
(Tokyo, Japan)
Erin SATO
(Shizuoka, Japan)
Takehito SATO
(Isehara, Japan)
Akihito SHIMAZU
(Tokyo, Japan)
Zhifeng SHAO
(Shanghai, China)
Sarah Shuck
(*Duarte, CA, USA*)
Judith SINGER-SAM
(Duarte, CA, USA)
Raj K. SINGH
(Dehradun, India)
Peipei SONG
(Tokyo, Japan)
Junko SUGAMA
(Kanazawa, Japan)
Zhipeng SUN
(Beijing, China)
Hiroshi TACHIBANA
(Isehara, Japan)
Tomoko TAKAMURA
(Tokyo, Japan)
Tadatoshi TAKAYAMA
(Tokyo, Japan)
Shin'ichi TAKEDA
(Tokyo, Japan)
Sumihito TAMURA
(Tokyo, Japan)
Puay Hoon TAN
(Singapore, Singapore)
Koji TANAKA
(Tsu, Japan)
John TERMINI
(Duarte, CA, USA)
Usa C. THISYAKORN
(Bangkok, Thailand)
Toshifumi TSUKAHARA
(Nomi, Japan)
Kohjiro UEKI
(Tokyo, Japan)
Masahiro UMEZAKI
(Tokyo, Japan)
Junming WANG
(Jackson, MS, USA)
Xiang-Dong Wang
(Boston, MA, USA)
Hisashi WATANABE
(Tokyo, Japan)
Jufeng XIA
(Tokyo, Japan)
Jinfu XU
(Shanghai, China)
Lingzhong XU
(Ji'nan, China)
Masatake YAMAUCHI
(Chiba, Japan)
Aitian YIN
(Ji'nan, China)
George W-C. YIP
(Singapore, Singapore)
Xue-Jie YU
(Galveston, TX, USA)
Rongfa YUAN
(Nanchang, China)
Benny C-Y ZEE
(Hong Kong, China)
Yong ZENG
(Chengdu, China)
Wei ZHANG
(Shanghai, China)
Wei ZHANG
(Tianjin, China)
Chengchao ZHOU
(Ji'nan, China)
Xiaomei ZHU
(Seattle, WA, USA)

(*as of August, 2022*)

CONTENTS

Volume 16, Number 4, 2022

Editorial

Review

Original Article

Brief Report

Correspondence

Editorial

DOI: 10.5582/bst.2022.01343

Monkeypox – A danger approaching Asia

Xiaoning Liu[1,2,§], Zheng Zhu[3,4,§], Qiqi Miao[1], Jia Wen Lim[2], Hongzhou Lu[1,*]

[1] Department of Infectious Diseases and Nursing research institution, National Clinical Research Center for Infectious Diseases, The Third People's Hospital of Shenzhen , Shenzhen, Guangdong, China;
[2] National Heart & Lung Institute, Faculty of Medicine, Imperial College London, London, United Kingdom;
[3] School of Nursing, Fudan University, Shanghai, China;
[4] NYU Rory Meyers College of Nursing, New York University, NY, USA.

SUMMARY Since the end of June 2022, there has been a dramatic increase in the number of monkeypox cases worldwide. Given the potential spread of this epidemic, WHO has declared the monkeypox epidemic a global public health emergency. In the face of the changing epidemiology during this monkeypox outbreak, vaccines and preventive measures are being researched around the world in response to this emerging disease. Recently, confirmed cases were reported in South Korea and Japan; as connections between countries around the world resume, imported cases may be inevitable. China is also concerned and prepared for the danger approaching Asia. In response to this risk, China issued the "Monkeypox Diagnosis and Treatment Guidelines" and the General Administration of Customs of China announced that travelers from countries reporting monkeypox cases and with suspected symptoms should be identified to customs upon entry. Chinese researchers have recently generated two pseudovirus reference materials for the monkeypox viral wild-type *B6R* gene and mutant *F3L* gene. Moreover, monkeypox as a communicable disease can be added to the current COVID-19 tracking system for better surveillance and management.

Keywords monkeypox, Asia, vaccine, preventive measures

Monkeypox, a zoonotic disease, was first identified in humans in the Democratic Republic of the Congo in 1970. In the 50 years since its inception, the monkeypox endemic was concentrated in Central and West Africa. Sporadic cases reported in Europe and North America were linked to imported cases (*1*). On May 7, 2022, a confirmed case of monkeypox was first reported in the United Kingdom, and several countries subsequently reported cases of monkeypox, spanning the globe from Europe to North America, Africa, and Asia. Since the end of June 2022, cases have tended to sharply increase globally (*2*). Given the risk of this epidemic spreading, the WHO declared the monkeypox epidemic a global public health emergency, which is the WHO's highest level of public health alert (Figure 1).

The changing epidemiology of monkeypox

During the 2022 monkeypox outbreak, cases were reported from all five continents in less than three months. More than 90% of the known cases were in men who have sex with men (MSM). More importantly, none of the patients had a clear history of travel to the site of the epidemic. This aspect is very different from before and has attracted the attention of researchers globally. An etiologic and epidemiologic study (*3*) published in the New England Journal of Medicine (NEJM) reported that 95% of the patients reported in the current monkeypox outbreak were infected via sexual contact and that monkeypox virus DNA was detected in the semen of 95% of patients. However, more clinical evidence needs to be gathered to corroborate whether monkeypox can be transmitted sexually.

A systematic review (*4*) reported that confirmed and suspected cases of monkeypox have clearly tended to increase since the 21st century. Over 19,000 cases were reported from 2000-2019. However, the current outbreak is spreading even more rapidly, with 80 countries worldwide reporting monkeypox infections since May 2022 and more than 17,000 cases have been confirmed as of July 23, 2022 (Figure 2). The number of confirmed cases in less than 3 months is comparable to the number over the last 20 years. A key reason for the rapid increase is the lack of protection from smallpox. Studies have indicated that the vaccine used for smallpox provides about 85% protection against monkeypox due to cross-immunization, which can prevent the occurrence of monkeypox or reduce the severity of symptoms (*5*).

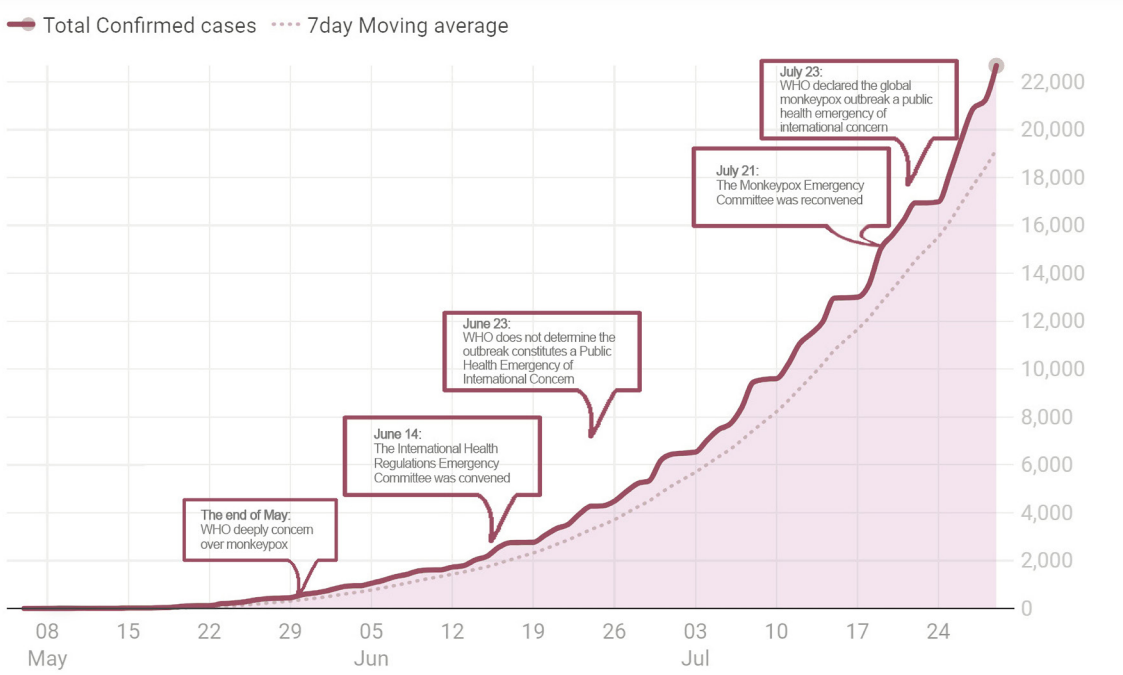

Figure 1. Timeline of WHO's responses to monkeypox outbreak. Data source: *https://ourworldindata.org/monkeypox*; *https://www.who.int/news-room/fact-sheets/detail/monkeypox*

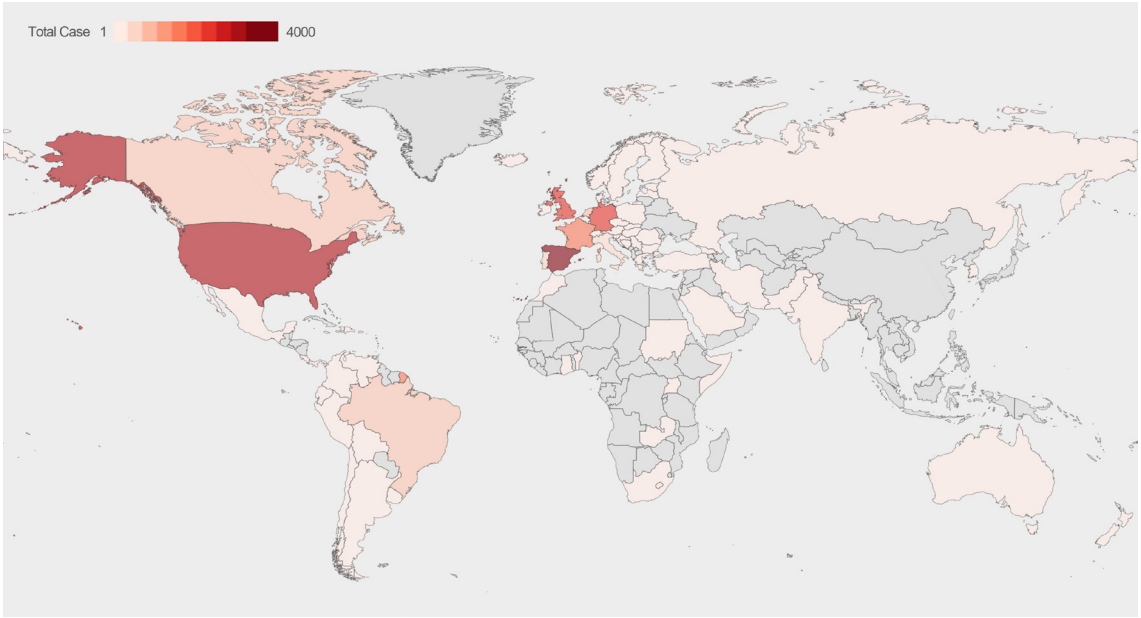

Figure 2. Global distribution of monkeypox cases. Data source: *https://ourworldindata.org/monkeypox*

Since the WHO declared the eradication of smallpox in 1980, smallpox vaccination has been discontinued worldwide (*6*). According to Thornhill *et al*. (*3*), the median age of patients during this outbreak was 38 years, so one can reasonably infer that most of this population lacks protection from smallpox. In addition, the relaxation of preventive and control measures for COVID-19 in many European countries has led to more frequent movement and travel of people. This is also one of the possible reasons for the rapid spread of the epidemic.

Genetic mutation of the monkeypox virus is also a concern. The general understanding is that monkeypox viruses are unlikely to undergo sudden mutations that would cause a substantial increase in human-to-human transmission because they are DNA viruses and are better at detecting and repairing mutations than RNA viruses. However, a study (*7*) found that MPXV B.1, a post-April strain of the monkeypox virus, has an APOBEC3 escape mutation. This strain has mutated more, making the virus

more adaptable to the human environment compared to a closely related virus (MPVX A.1.1) identified in 2018-2019.

Vaccine stockpile and vaccination

To date, there is no specific vaccine for monkeypox virus. The vaccines that exist for the prevention of monkeypox in high-risk groups or post-exposure prophylaxis are still smallpox-specific vaccines. Thus far, the third generation of smallpox vaccines has been developed. The effectiveness of the second-generation vaccine ACAM2000 and the third-generation vaccine IMVAMUNE at preventing monkeypox infection and for post-exposure vaccination has been partially corroborated by the results of preclinical and clinical studies (*8,9*).

Currently, the use of smallpox vaccine for monkeypox prevention is still mainly restricted to high-risk groups or health personnel who treat the disease. Given the risk of an outbreak, the United Kingdom has begun offering the smallpox vaccine to some medical personnel or people at risk of exposure to the monkeypox virus. On July 22, the European Medicines Agency recommended that the European Union approve an expanded indication for smallpox vaccines to prevent monkeypox and interrupt transmission of the virus. However, mass vaccination against monkeypox is not required or recommended at this time.

Immunodeficiency may lead to worse clinical outcomes of a monkeypox infection (*10*). Liu *et al*. (*11*) suggested that an advanced or poorly virally controlled HIV infection may lead to more severe outcomes after monkeypox infection. According to Thornhill *et al*. (*3*), there were no differences in clinical manifestation or outcomes between patients infected or not infected with HIV, but that study only included (people living with HIV) PLWH whose viral load was well-controlled. Therefore, awareness of the potentially serious outcomes of monkeypox infection is crucial for people with advanced or poorly virally controlled HIV. Mass vaccination of MSM, the main at-risk population, is not recommended at this time but enhanced monitoring of their HIV infection status is strongly recommended.

Risk of monkeypox outbreaks in mainland China

Confirmed cases of monkeypox in countries neighboring China such as South Korea and Japan have been reported. Although most cases during this outbreak involve MSM, they also include a small number of children with no known epidemiological link to those cases. This indicates that close contact, droplets, and aerosols can still pose a considerable risk of transmission. Non-sexual close contact transmission still needs to be considered seriously to prevent and control the epidemic.

With the gradual restoration of connections between countries around the world, imported cases may be inevitable in China (*12*). In response to this risk, China issued the "Monkeypox Diagnosis and Treatment Guidelines" (*13*) in June; on July 24, the General Administration of Customs of China announced that travelers from countries reporting monkeypox cases or with suspected symptoms should be reported to customs upon entry. In fact, monkeypox as a communicable disease can be added to the current COVID-19 tracking system for better surveillance and management. Chinese researchers have recently generated two pseudovirus reference materials for the monkeypox viral wild-type *B6R* gene and mutant *F3L* gene. These two reference materials can be used to develop monkeypox virus detection kits, to verify their performance confirmation, to validate their methodology, to control quality in the laboratory, and to provide a "biological scale" for monkeypox virus diagnostic results, providing technical support to effectively reduce "false negatives" (*14*).

In light of the current strategy of "dynamic zero COVID-19" in China, the risk of monkeypox spreading in China is still low. Despite these favorable conditions, the harm caused to the population and society by the monkeypox epidemic should not be underestimated. The average symptomatic period after infection with monkeypox is three weeks, and the proportion of asymptomatic patients is low. At least 3 weeks of isolation are required for people infected with the monkeypox virus. COVID-19 is still rampant around the world. The spread of the monkeypox epidemic will have a negative impact on the labor supply and the provision of goods and services.

Conclusion

We are now faced with high inflation globally, which will also have a huge impact on overall social efficiency. The risk of imported monkeypox cases should be kept in mind by the government. Public education about monkeypox prevention and related knowledge for the general public, including MSM, can help with early detection and reporting of cases and reduce transmission. The establishment of a comprehensive disease surveillance system, and particularly the establishment of sentinel sites in relevant institutions such as dermatology and sexual health clinics, will facilitate the early detection of monkeypox cases and close contact tracing.

Acknowledgements

The authors wish to acknowledge and thank all of the participants and the authors for their contributions.

Funding: This work was supported by a grant for the "Study of the activation and intervention strategies of the IL-6/NF-KB inflammatory signalling pathway induced by SARS-CoV-2".

Conflict of Interest: The authors have no conflicts of interest to disclose.

References

1. Moore MJ, Rathish B, Zahra F. Monkeypox. *https://www.ncbi.nlm.nih.gov/books/NBK574519/* (accessed on July 23, 2022).
2. UN News. Monkeypox not presently a global public health emergency: WHO. *https://news.un.org/en/story/2022/06/1121362/* (accessed on July 25, 2022).
3. Thornhill JP, Barkati S, Walmsley S, *et al*. Monkeypox virus infection in humans across 16 countries - April-June 2022. N Engl J Med. 2022; doi:10.1056/NEJMoa2207323.
4. Bunge EM, Hoet B, Chen L, Lienert F, Weidenthaler H, Baer LR, Steffen R. The changing epidemiology of human monkeypox-A potential threat? A systematic review. PLoS Negl Trop Dis. 2022; 16:e0010141.
5. Fine PE, Jezek Z, Grab B, Dixon H. The transmission potential of monkeypox virus in human populations. Int J Epidemiol. 1988; 17:643-650.
6. World Health Organization. Monkeypox. *https://www.who.int/news-room/fact-sheets/detail/monkeypox* (accessed July 25, 2022).
7. Isidro J, Borges V, Pinto M, *et al*. Phylogenomic characterization and signs of microevolution in the 2022 multi-country outbreak of monkeypox virus. Nat Med. 2022; doi:10.1038/s41591-022-01907-y.
8. Petersen BW, Kabamba J, McCollum AM, Lushima RS, Wemakoy EO, Muyembe Tamfum JJ, Nguete B, Hughes CM, Monroe BP, Reynolds MG. Vaccinating against monkeypox in the Democratic Republic of the Congo. Antiviral Res. 2019; 162:171-177.
9. Keckler MS, Salzer JS, Patel N, Townsend MB, Nakazawa YJ, Doty JB, Gallardo-Romero NF, Satheshkumar PS, Carroll DS, Karem KL, Damon IK. IMVAMUNE® and ACAM2000® provide different protection against disease when administered postexposure in an intranasal monkeypox challenge prairie dog model. Vaccines (Basel). 2020; 8:396.
10. Liu X, Jiang XQ, Zhu Z, Sun L, Lu HZ. The novel monkeypox outbreak: What should we know and reflect on?. Zoonoses. 2022; DOI: 10.15212/ZOONOSES-2022-0022.
11. Liu X, Zhu Z, He Y, Lim JW, Lane B, Wang H, Peng Q, Sun L, Lu H. Monkeypox claims new victims: The outbreak in men who have sex with men. Infect Dis Poverty. 2022; 11:84.
12. Wei Q. Is China ready for monkeypox? Animal Model Exp Med. 2022 Jul 27. doi: 10.1002/ame2.12259.
13. Monkeypox Diagnosis and Treatment Guidelines. *https://baijiahao.baidu.com/s?id=1735900860873446404&wfr=spider&for=pc* (accessed July 29, 2022). (in Chinese)
14. China Institute of Metrology successfully developed monkeypox virus pseudovirus standard material. *https://www.cqn.com.cn/zgzlb/content/2022-07/28/content_8846463.htm* (accessed July 29, 2022).

Received July 23, 2022; Revised July 29, 2022; Accepted July 31, 2022.

[§]These authors contributed equally to this work.
**Address correspondence to:*
Hongzhou Lu, Department of Infectious Diseases, National Clinical Research Center for Infectious Diseases, Shenzhen Third People's Hospital, Shenzhen 518112, Guangdong Province, China.
E-mail: luhongzhou@szsy.sustech.edu.cn

Released online in J-STAGE as advance publication August 2, 2022.

Review

DOI: 10.5582/bst.2022.01352

Can kynurenine pathway be considered as a next-generation therapeutic target for Parkinson's disease? An update information

Wei Qin[1], Yirong Shi[2], Weimei Chen[2], Xiaokang Jia[3,*], Tetsuya Asakawa[4,*]

[1] Department of Rehabilitation, Enshi Central Hospital, Enshi, Hubei, China;
[2] Department of Nursing, the Third People's Hospital of Shenzhen, Shenzhen, Guangdong, China;
[3] Department of Neurology, the Eighth Affiliated Hospital, Sun Yat-Sen University, Shenzhen, Guangdong, China;
[4] Institute of Neurology, the Third People's Hospital of Shenzhen, Shenzhen, Guangdong, China.

SUMMARY By far, no revolutionary breakthrough in the treatment of Parkinson's disease (PD) was found. It is indeed a knotty problem to select a satisfactory strategy for treating some patients with advanced stage PD. Development of novel therapeutic targets against PD has been an urgent task faced by global PD researchers. Targets in the tryptophan–kynurenine pathway (KP) were then considered. Metabolites in the KP are liposoluble. Some neurotoxic metabolites, including 3-hydroxykynurenine and its downstream 3-hydroxyanthranilic acid and quinolinic acid, are mainly produced peripherally. They can easily cross the blood–brain barrier (BBB) and exert their neurotoxic effects in the central neuron system (CNS), which is considered as a potential pathophysiological mechanism of neurodegenerative diseases. Hence, agents against the targets in the KP have two characteristics: (1) being independent from the dopaminergic system and (2) being seldom affected by the BBB. Inspiringly, one agent, namely, the inhibitor of indoleamine 2,3-dioxygenase 1, has been currently reported to present satisfactory efficacy comparable to levodopa, implying that the KP might be a potential novel target for PD. This review collected and summarized the updated information regarding the association of the KP with PD, which is helpful for understanding the clinical value of the KP in the PD scenario.

Keywords Tryptophan-kynurenine pathway, Parkinson's disease, Indoleamine 2,3-dioxygenase 1 (IDO1), Dopaminergic medication, Blood-brain barrier

1. Introduction

Parkinson's disease (PD) is the second most common neurodegenerative disease (NDD) (*1,2*). Approximately 10 million people are suffering from PD, and the number of cases is expected to be more than doubled in the next 20 years (*3*). PD remarkably affects the patients' activity of daily living (ADL), particularly for those who are in the advanced stage, whose daily living has to depend on the caregiver. This situation reduces the patients' quality of life (QOL). Moreover, it significantly enhanced the financial burden not only for the government but also for each involved family. With the aging of population, PD has gradually become an important global public health concern. Hence, development of novel treatments against PD has been an urgent task faced by global PD clinicians and scientists. Understanding PD pathogenesis, particularly elucidating the involved molecular mechanisms, is the key to explore the potential new therapeutic targets in treating PD.

Unfortunately, by far, all treatments against PD are far from satisfactory (*4*). Dopaminergic medication is the mainstream therapy, where levodopa (L-dopa) is the mainstay agent for PD. Dopaminergic agents combined with non-dopaminergic agents are commonly prescribed clinically. Nevertheless, only few kinds of non-dopaminergic drugs are available for clinical use, such as amantadine (promoting the release of dopamine and neuroprotective effects), anticholinergic drugs (such as benzhexol), whose efficacy along with indications have noticeable limitations. Finding new agents whose mechanisms are independent from the dopaminergic system is challenging. Additionally, by far, all the mainstream agents recommended by the PD guidelines worldwide are remarkably affected by the blood–brain barrier (BBB) along with their peripheral metabolism. In case of an agent, which is seldom affected by the BBB, it can influence the central neuron system (CNS) peripherally and will be convenient for clinical use. In this regard, the keywords "non-dopaminergic" as well as "seldom affected by the BBB" should be a novel direction in exploring new agents for PD.

Our previous study reported that electrical stimulation of the peripheral tissue may improve the striatal dopamine levels, indicating that intervention in the peripheral tissue (other than in the CNS) may affect the dopamine content in the CNS (*5*). Meanwhile, our preliminary experiments found that the plasma tryptophan levels in PD animal models significantly reduced, whereas the plasma kynurenine levels increased (Figure 1). These preliminary data suggest that the tryptophan–kynurenine pathway (KP) might be involved in the regulation of PD pathogenesis. Moreover, it is known that indoleamine 2,3-dioxygenase 1 (IDO1), the key enzyme of the KP, is very lowly expressed in the CNS. However, it is highly expressed in the peripheral organs such as the lung, kidney, and liver. IDO1 regulation is mainly in the periphery, rather than in the CNS. Therefore, the KP regulated by IDO1 has two major characteristics, namely, independent of neural dopaminergic systems and seldom affected by the BBB, thereby are considered as a novel therapeutic target for PD. The elements of the KP, particularly IDO1, are reported to be closely associated with neurological diseases, including depression (*6-8*), Alzheimer's disease (AD) (*9*), multiple sclerosis (*10*), stroke (*11*), and PD (*12-14*).

Several reviews have discussed the role of the KP in the CNS disorders. Mazarei *et al.* reviewed the special role of the KP in Huntington's disease. They pointed out that although most of the previous the KP studies focused on depression, CNS tumors, and multiple sclerosis, the role of IDO in the NDDs cannot be ignored (*15*). Later, Lovelace reviewed the role of the KP and IDO1 in multiple sclerosis (*10*). Kennedy *et al.* reported that the KP metabolism may affect the CNS function and relate to the CNS disorders *via* the microbiota–gut–brain axis (*16*). A recent review study discussed the relationship between PD and the KP from the angles of microbiota–gut–brain, genetic link, and enzyme. They believe that the KP might be considered as a promising biomarker as well as therapeutic target for PD (*17*). Based on the abovementioned information and the current progress in the experimental studies of IDO1 on PD, we were motivated to conduct this review, focusing on the potential therapeutic role of the KP, particularly IDO1, in treating PD. We believe that this review will be beneficial in deepening insights regarding the effects of the KP on PD and helpful for developing novel therapeutic targets against PD, which are independent from the dopaminergic system and less affected by the BBB.

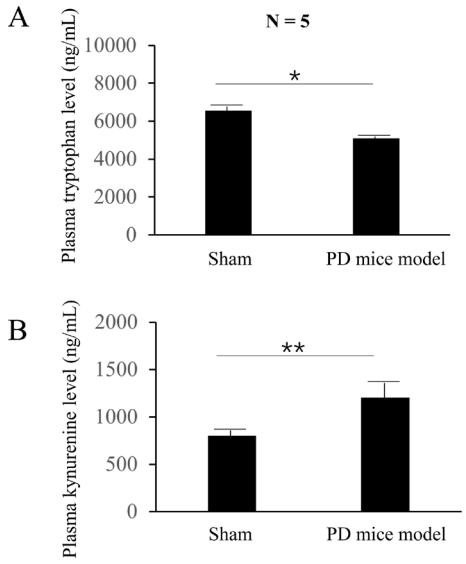

Figure 1. Preliminary data of the changes of plasma tryptophan and kynurenine in PD mice model. (A). Plasma tryptophan levels in 1-methyl-4-phenyl-1, 2, 3, 6-tetrahydropyridine (MPTP)-induced PD mouse models significantly reduced (*vs*. sham group). **(B)**. Plasma kynurenine levels in MPTP-induced PD mouse models significantly increased (*vs*. sham group). $n = 5$ in each group; *represents $p < 0.05$; **represents $p < 0.01$.

2. Status quo of PD treatment

The etiology and pathogenesis of PD are very complex and, presently, remain unclear, particularly the underlying causes of dopaminergic neuron apoptosis in the nigrostriatal pathway. Indeed, this may delay the development of efficacious treatments against PD since therapies focused on PD etiology cannot be created. Since the emergence of L-dopa in 1967 and the development of deep brain stimulation (DBS) in 1993, no revolutionary breakthrough regarding the treatment of PD has been reported (*4*). Dopaminergic medication and DBS still remain the mainstay treatments against PD. However, these treatments cannot stop dopaminergic neuron apoptosis, and hence, cannot halt PD progression either. Due to this, the PD treatments that are available nowadays are symptomatic. Our previous studies confirmed that both L-dopa and DBS can significantly improve PD symptoms in patients (*18-20*) and rodent PD (*21-23*) and primate PD (*24,25*) models. However, these treatments cannot halt the progression of PD and depletion of dopaminergic neurons. Currently, the first-line therapies for PD, including L-dopa, dopamine receptor agonists, monoamine oxidase inhibitors, or catechol-O-methyltransferase inhibitors, all act on the dopaminergic system and are collectively associated with the principle of dopamine replacement. However, the efficacy of these dopaminergic medications is far from satisfactory. For example, with PD progression, the decline of L-dopa efficacy (well known as the "wearing-off phenomenon") and side effects caused by the drug itself (such as dyskinesia; "on-off phenomenon") are becoming predominant problems following the long-term prescription of L-dopa. Surgical treatment, including DBS, also exhibits several limitations. For example, DBS is effective only for those patients who respond suitably to L-dopa. Additionally, DBS is a symptomatic treatment, which cannot stop PD progression. As an invasive surgery, the long-term efficacy of DBS remains

controversial and its mechanisms have never been clarified (*4,18-20,24,25*). Hence, selecting a satisfactory strategy for treating patients with advanced stage PD, particularly the selection of appropriate drugs, is indeed a difficult quandary. For some patients in the end stage, clinicians might be in a dilemma since no suitable drugs are available. In other words, the development of effective therapies against PD is urgently required, particularly the development of new agents with novel mechanisms (such as a mechanism of action independent of the dopaminergic system). This is where the KP system comes into the picture.

3. Roles of the KP in the CNS

Tryptophan, one of the eight essential amino acids in humans, plays indispensable roles in maintaining human growth, metabolism, and positive nitrogen balance. Approximately, over 95% of tryptophan is metabolized *via* the KP, while less than 5% of tryptophan generates 5-hydroxytryptamine (5-HT) (Figure 2). Under normal physiological conditions, tryptophan is found in almost all mammalian tissues, but mainly in the liver. The KP involves a series of steps by which tryptophan is finally converted to nicotinamide adenine dinucleotide + (NAD +) in the liver (Figure 2). The process of the KP is as follows: first, tryptophan is converted into n-formyl-kynurenine by two groups of rate-limiting enzymes, namely, IDO and tryptophan 2,3-dioxygenase (TDO). IDO is divided into two subtypes: IDO1 and IDO2. N-formyl-kynurenine is unstable and quickly converts into kynurenine. Kynurenine is nontoxic and forms the core of the KP. Kynurenine is then catalyzed by kynurenine-3-monooxidase (KMO) and converted into toxic 3-hydroxykynurenine (3-HK). Subsequently, 3-HK is converted into toxic 3-hydroxyanthranilic acid (3-HAA) catalyzed by kynureninase. Simultaneously, kynurenine can also be converted into anthranilic acid under the action of kynureninase. Anthranilic acid is also further converted into 3-HAA by monohydroxylase. Then, 3-HAA is converted into toxic quinolinic acid (QUIN), which is catalyzed by the kynurenine aminotransferase family. QUIN forms nicotine, which is converted into the end products (NAD +/NADP +) under the action of transamination. Additionally, there is another pathway where kynurenine is converted into a neuroprotective kynurenic acid (KA) catalyzed by kynurenic aminotransferase (*26-28*) (Figure 2).

In this review, the term "kynurenine-ergic substances (KESs)" was used for the metabolites generated in the KP, which exhibit multifold biological activities and are liposoluble. Of these KESs, only KA is neuroprotective. The remaining substances, including 3-HK, downstream 3-HAA, and further downstream QUIN, are neurotoxic (Figure 2). The KP mainly activates in the liver and most of the KESs are derived from the peripheral tissues. Nevertheless, under certain physiological (aging) or some pathological (BBB damage) conditions, these liposoluble substances may cross the BBB and affect the CNS. The KESs might be important "neurotoxins" that contribute to neuronal apoptosis in NDDs. Early in 1981, Stone and Perkins reported the agonistic effects of QUIN on central N-methyl-D-aspartic acid (NMDA) (*29*). Subsequently, Kessler *et al*. discovered the antagonistic effects of KA on the NMDA receptor (*30*). Till date, numerous studies have elucidated the physiological and pathological effects of these KESs from multiple dimensions: (1) IDO1, IDO2, and TDO act as the first rate-limiting enzymes in the KP. TDO is mainly expressed in the liver, whereas IDO is widely expressed in several organs, including the brain, liver, and kidney, and several cells, including monocytes and dendritic immune cells. IDO is

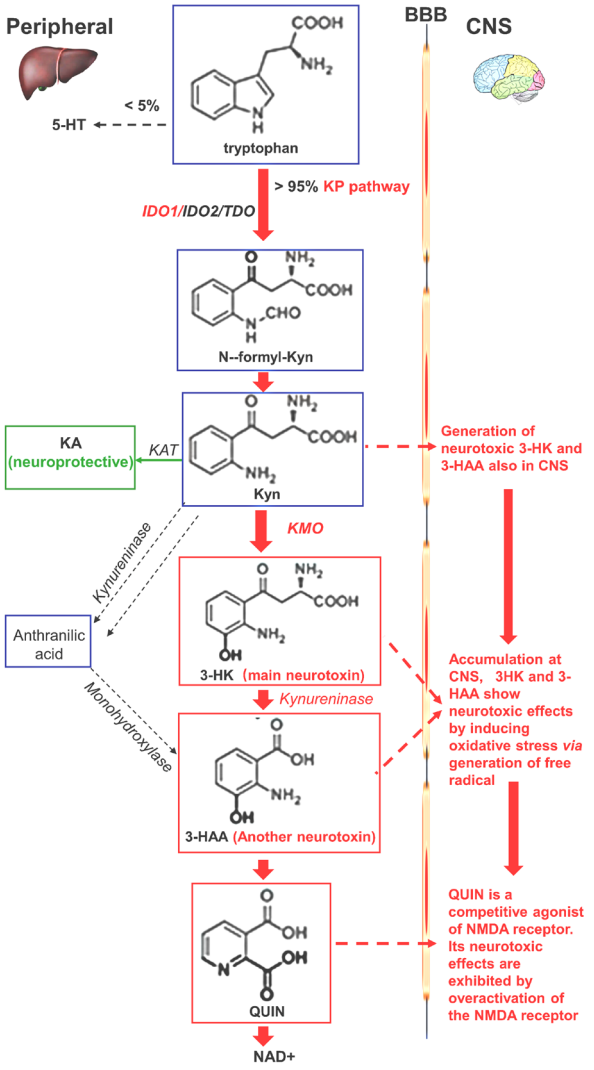

Figure 2. Metabolic processes of the tryptophan–kynurenine pathway and its pathophysiological roles in the CNS. 3-HAA: 3-hydroxyanthranilic acid; 3-HK: 3-hydroxykynurenine; 5-HT: 5-hydroxytryptamine; BBB: blood–brain barrier; CNS: central neuron system; KA: kynurenic acid; KAT: kynurenic aminotransferase; KMO: kynurenine-3-monooxidase; KP: tryptophan–kynurenine pathway; Kyn: kynurenine; IDO: indoleamine 2,3-dioxygenase; NAD: nicotinamide adenine dinucleotide; TDO: tryptophan 2,3-dioxygenase; QUIN: quinolinic acid.

commonly considered the predominant catalytic enzyme produced under inflammatory and/or stressful conditions (*31*). IDO1 can activate both anti-inflammatory and proinflammatory cytokines. Moreover, the activated T-cells, along with numerous inflammatory signaling pathways (such as NF-κB and TLR4), play a role in IDO1 activation (*31*). Although both peripheral and brain cytokines can induce IDO activation, IDO regulation mainly occurs in the peripheral tissues rather than in the CNS (*32*). (2) Kynurenine is subsequently regulated by the second rate-limiting enzyme KMO. KMO contributes to the regulation of 3-HK expression and can be stimulated by inflammatory factors, subsequently increasing the production of downstream 3-HK and QUIN, which exhibit neurotoxicity (*33*). KMO displays functions analogous to IDO. (3) Neurotoxins produced in the KP include 3-HK, 3-HAA, and QUIN. A large amount of 3-HK produced by the peripheral tissue may easily cross the BBB and accumulate in the CNS due to its high liposolubility. Microglia and astrocytes in the CNS produce a small amount of indigenous 3-HK. Even in healthy circumstances, 3-HK and 3-HAA can produce a number of free radicals, subsequently causing oxidative stress and mitochondrial damage, which may directly induce CNS disorders. Moreover, in an inflammatory circumstance, the overexpression of KMO and 3-HK enhances downstream QUIN levels and causes more severe neurological damage (*17*). QUIN is an agonist of the NMDA receptor, which exhibits the same effects on the NR2A and NR2B subtypes. Although QUIN may promote the release of glutamate in neurons, it simultaneously also suppresses glutamate uptake by glial cells. These effects induce the overactivation of the NMDA receptor, further inducing excessive calcium influx (*34*). In other words, the overactivation of the NMDA receptor may generate superabundant reactive oxygen species. These effects finally result in comprehensive neuronal damage. Additionally, QUIN plays a role in triggering local CNS inflammation. It has been reported that QUIN is closely associated with a series of inflammatory processes in the CNS (*17*). Briefly, the neurotoxic effects of the KP are due to 3-HK, 3-HAA, and QUIN. (4) As the sole neuroprotective component of the KP, KA acts as an antagonist for three endogenous glutamate receptors, particularly for the NMDA receptor. The neuroprotective action of KA is due to the suppression of the neurotoxicity that is produced by the activation of the NMDA receptor by QUIN overactivation (*35*). Moreover, KA can also antagonize the noncompetitive α7-nicotinic acetylcholine receptor (α7-nAChR) and reduce the extracellular levels of glutamate and dopamine in the CNS (*36*). In this regard, the QUIN/KA ratio is commonly used as an index of glutamate receptor activation and neurotoxicity.

Reportedly, KESs, particularly IDO1, are closely associated with the neurological disease. Some previous studies reported that IDO1 overexpression enhances the ratio of kynurenine/tryptophan, thereby inducing depression-like behaviors in animals (*6-8*). Conversely, the suppression of IDO1 expression may alleviate such depression-like symptoms (*6*). Leraci *et al*. revealed that the activation of the KP induces cognitive impairment in rats, the mechanisms of which might be related to the decline in the levels of brain-derived neurotrophic factor (*37*). Other studies have reported that the KP is associated with stroke (*11*) and multiple sclerosis (*10*). Widner *et al*. found that the ratios of serum kynurenine/tryptophan and IDO1 increased and the activation of IDO1 is relevant to the cognitive impairment observed in patients with AD (*9*). Duan *et al*. found that IDO1 inhibitor can alleviate neurotoxicity associated with amyloid β and tau proteins in animal models of AD (*38*). They hypothesized that IDO1 inhibitor might exhibit neuroprotective effects on PD since PD is also an NDD with protein depositions (*38*). Currently, the effects of the KP on CNS diseases are complicated and remain unclear. Recently, Park *et al*. reported that antioxidant stress might be an essential mechanism underlying this effect. As a key enzyme in the KP, IDO1 plays a crucial role in the regulation of the KP. Hence, IDO1 should be considered a potential therapeutic target for neurological diseases (*39*).

4. Association between the KP and PD

Our preliminary data demonstrates that the tryptophan levels in the animal models of PD decreased, while the kynurenine levels enhanced, indicating the involvement of the KP in the pathophysiology of PD. These data implied that during the PD state, the KP is activated, which might be associated with a battery of neurotoxic effects. Early in 1992, Ogawa *et al*. reported that the levels of neurotoxic 3-HK in the putamen and substantia nigra significantly increased, while those of neuroprotective KA decreased in patients with PD (*40*). Later, Miranda *et al*. reported that the enhancement of the KA levels in animal brains resulted in resistance toward QUIN-mediated neurotoxicity and the protection of the dopamine neurons (*41*). Zadori *et al*. reported that the induction of KA production in the KP serves a neuroprotective function, contributing to the amelioration of PD symptoms (*42*). Recently, Perez Pardo *et al*. verified that TDO inhibitors can significantly improve PD symptoms and CNS inflammation in rotenone-induced PD models. These results provided further evidence concerning a key link between the KP and inflammatory mechanisms of PD (*12*). The aforementioned results prove that the KP is closely associated with the development and progression of PD.

Two factors, namely, aging and gut microbiota, are involved in the relationship between the KP and PD. Aging is the most important factor that affects the development and progression of PD; meanwhile, aging also plays a key role in the disorders of the KP.

Reportedly, the cerebral IPO activity increases with aging (*43*). Sustained stimuli from a low degree of inflammation and the IDO upregulation may influence some aging-related disease. For example, aging-related inflammation might trigger the activation of the KP and increase the risk of developing NDDs (*44,45*). Commonly, due to the existence of the BBB, inflammatory factors present in the peripheral organs and tissues have diminished direct influence on the CNS. However, in terms of the liposoluble nature of the KESs in the KP, they have the remarkable ability to affect the CNS by crossing the BBB. Therefore, we believe that the KP plays a key role in "delivering aging signal" from the periphery to the CNS, thereby contributing to the regulation of inflammatory processes in the CNS (*46,47*).

Another factor involved in the relationship between the KP and PD is the disturbance of the gut microbiota. From the viewpoint of the microbiota-gut-brain axis, the KP acts as a bridge between α-synuclein (α-syn) deposition and the gut microbiome. It is well established that α-syn accumulation Lewy body formation in dopaminergic neurons are the most important neuropathological characteristics of PD. α-Syn deposition has been reported to occur not only in the CNS but also in the intestine in patients with PD, as well as in older individuals without PD (*48*). Bu *et al*. reported α-syn deposition in the enteric nerves of older people without PD (*49*). Moreover, Devos *et al*. revealed that kynurenine present in the gut can easily cross the BBB and affect the KP metabolism in the brain (*50*). Some gut microbiota can even directly produce kynurenine and 3-HAA (*51*), which possibly cross the BBB and introduce neurotoxic effects in the CNS. Evidence indicates that the disturbance of the gut microbiota can affect the plasma concentration of KESs (*17*). Moreover, high QUIN levels in the abnormal KP under certain pathological conditions has been reported to be associated with α-syn deposition in the gut (*52*). A recent study suggested that α-syn deposition originates in the digestive tract and affects the brain *via* the vagus nerve pathway (*53*). These aforementioned reports seem to imply that the microbiota–gut–brain axis affects α-syn deposition *via* the KP; however, unfortunately, to the best of our knowledge, no studies so far have provided evidence indicating the direct association between the abnormal KP and α-syn deposition in the CNS and that the abnormal KP causes PD. Therefore, we speculate that aging, along with other pathological factors, may induce gut microbiota disturbance, subsequently activating the KP and producing a number of toxic KESs, which cross the BBB, ultimately inducing α-syn deposition (Figure 3).

5. IDO1 is a key target for regulation of the KP and PD

Compared with TDO, IDO is more widely distributed. IDO1 is widely expressed in the peripheral organs and tissues including the lung, blood vessels, and fat. IDO1 expression is upregulating with age. Moreover, the expression level of IDO1 is also positively correlated with the expression of aging markers, including p16 and p21 (*54*), as well as the expression of aging-related secretory phenotypes, including IL-6 and TNF-α (*55*). In the aging animal models, the expression level of IDO1 is also significantly upregulated, which accelerated the aging processes in these animals (*56*). Evidence shows that stimuli of low-degree sustained inflammation can induce IDO1 upregulation, which activate the KP and further increase the risk of NDDs (*44,45*). These

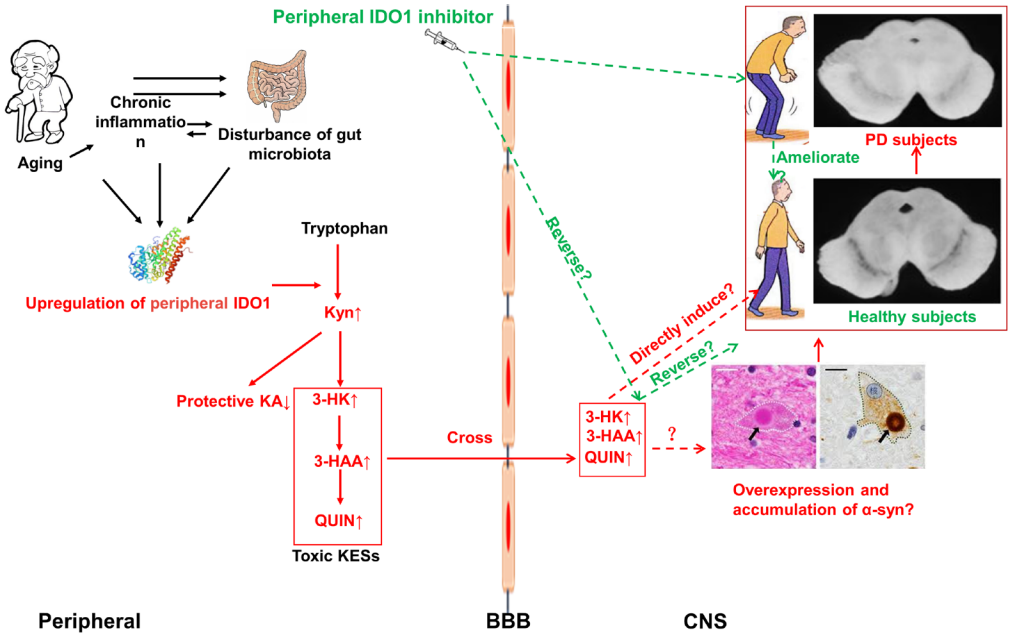

Figure 3. Potential mechanisms involved in the interactions between the KP and PD. Red represents the pathological changes induced by the KP, and green represents the protective effects conducted by the intervention of the KP with an IDO1 inhibitor.

studies confirmed that IDO1 is highly correlated with inflammation. However, presently, there is only direct evidence concerning increased IDO1 expression in AD (*17*), but not reported in PD. In terms of the indirect evidence, currently, Ning *et al*. employed a co-inhibitor of IDO1 and TDO to treat the rat PD models. They found that IDO1 suppression reduced the levels of inflammatory factors, increased the neuroprotective KA level, and alleviated the depletion of dopamine neurons in the rats' brain. Importantly, administration of IDO1 inhibitor significantly improved the motor symptoms in PD animals, and its efficacy is comparable to L-dopa (*13*). Sodhi *et al*. directly administrated an IDO1 inhibitor in the traditional 6-hydroxydopamine-induced PD rat models. They found that the behavioral performance in PD animals was significantly improved. The degrees of oxidative stress, inflammation, and mitochondrial damage in the CNS were also improved (*14*). These investigations suggest that IDO1 can be considered as a potential key target in the KP, which is closely involved in the development of PD. Hence, we hypothesize that the peripheral IDO1 activity increased with aging or under certain pathological conditions (like inflammation). Such activated IDO1 may stimulate the KP metabolism, resulting in the production of more toxic KESs, which might cross the BBB and cause neuronal damage in the CNS (*43*) (Figure 3). However, so far, several evidences in this hypothesis remain absent: (1) No direct evidence has elucidated that upregulation of IDO1 will affect cerebral α-syn deposition and dopamine neuron apoptosis in the PD subjects. (2) With respect to efficacy, only two studies verified the efficacy of IDO1 suppression against PD symptoms. However, these studies employed the simplest behavioral assessments in rodent PD animal. Investigations with more rigorous experimental design to verify the efficacy of IDO1 suppression are indispensable, for example, effects of IDO1 inhibitor on different stage of PD model, on nonmotor symptoms, and on different sorts of PD model (mouse, rat, and nonhuman primates). (3) What are the interactions between IDO1 suppression and conventional dopaminergic therapeutics; synergistic effects or canceling effects? To uncover the roles of the KP, particularly IDO1, in PD, several further investigations are expected to clarify these issues.

6. Concluding remarks

In this review, updated information regarding the roles of the KP in PD was provided. The results of Ning's study (*13*) got an inspiring result, that is, IDO1 inhibitor might achieve a "comparable" efficacy versus L-dopa, which is now still regarded as the golden standard medication for PD. We believe the KESs, particularly IDO1, are promising novel targets against PD, which are independent from the dopaminergic system and are seldom affected by the BBB. Once these novel targets are successfully verified and developed, they are the next-generation medications in treating PD. Clinicians can have more options other than the dopaminergic medications. Moreover, administration and regulation of such medicines will be very convenient, since they mainly act in the periphery and are seldom influenced by the BBB. Hence, the effects of the KP, KESs, particularly IDO1, on PD warrant further notice and investigation since it might bring a revolutionary progress in the PD treatment.

However, to uncover the secrets of the KP on PD, panoramic understanding and insights are indispensable. The following concerns should be fully addressed:

i) Expression and distribution of all the KP members, including KESs in the peripheral organs, and the CNS should be thoroughly clarified, particularly under the PD pathological conditions.

ii) Can KESs affect α-syn expression and deposition and further affect the apoptosis of dopamine neurons?

iii) Clinically, can intervention of KESs achieve amelioration of the PD symptoms, including motor and nonmotor symptoms? Finally, can it stop the PD progression?

iv) What are the interactions between intervention of KESs and conventional dopaminergic therapy? Can patients benefit from combining these two different medications, for example, achieve improvement of QOL and ADL?

Undoubtedly, at present, researches clarifying the effects of the KP on PD remain in the exploratory stage. Verifying the effects of the KP will still take a long time, even though the first light has risen.

Funding: None.

Conflict of Interest: The authors have no conflicts of interest to disclose.

References

1. Tysnes OB, Storstein A. Epidemiology of Parkinson's disease. J Neural Transm (Vienna). 2017; 124:901-905.
2. Asakawa T, Fang H, Sugiyama K, Nozaki T, Kobayashi S, Hong Z, Suzuki K, Mori N, Yang Y, Hua F, Ding G, Wen G, Namba H, Xia Y. Human behavioral assessments in current research of Parkinson's disease. Neurosci Biobehav Rev. 2016; 68:741-772.
3. Schapira AH. Recent developments in biomarkers in Parkinson disease. Curr Opin Neurol. 2013; 26:395-400.
4. Asakawa T, Sugiyama K, Nozaki T, Sameshima T, Kobayashi S, Wang L, Hong Z, Chen S, Li C, Namba H. Can the Latest Computerized Technologies Revolutionize Conventional Assessment Tools and Therapies for a Neurological Disease? The Example of Parkinson's Disease. Neurol Med Chir (Tokyo). 2019; 59:69-78.
5. Asakawa T, Fang H, Hong Z, Sugiyama K, Nozaki T, Namba H. Peripheral stimulation in treating Parkinson's disease: Is it a realistic idea or a romantic whimsicality? Intractable Rare Dis Res. 2012; 1:144-150.

6. Xie W, Cai L, Yu Y, Gao L, Xiao L, He Q, Ren Z, Liu Y. Activation of brain indoleamine 2,3-dioxygenase contributes to epilepsy-associated depressive-like behavior in rats with chronic temporal lobe epilepsy. J Neuroinflammation. 2014; 11:41.
7. Expanded programme on immunization. Formulation of Pasteur BCG vaccine. Wkly Epidemiol Rec. 1990; 65:99.
8. Kim H, Chen L, Lim G, Sung B, Wang S, McCabe MF, Rusanescu G, Yang L, Tian Y, Mao J. Brain indoleamine 2,3-dioxygenase contributes to the comorbidity of pain and depression. J Clin Invest. 2012; 122:2940-2954.
9. Widner B, Leblhuber F, Fuchs D. Increased neopterin production and tryptophan degradation in advanced Parkinson's disease. Journal of neural transmission (Vienna, Austria : 1996). 2002; 109:181-189.
10. Lovelace MD, Varney B, Sundaram G, Franco NF, Ng ML, Pai S, Lim CK, Guillemin GJ, Brew BJ. Current Evidence for a Role of the Kynurenine Pathway of Tryptophan Metabolism in Multiple Sclerosis. Front Immunol. 2016; 7:246.
11. Chen C, Chencheng Z, Cuiying L, Xiaokun G. Plasmacytoid Dendritic Cells Protect Against Middle Cerebral Artery Occlusion Induced Brain Injury by Priming Regulatory T Cells. Front Cell Neurosci. 2020; 14:8.
12. Perez-Pardo P, Grobben Y, Willemsen-Seegers N, *et al*. Pharmacological validation of TDO as a target for Parkinson's disease. The FEBS journal. 2021; 288:4311-4331.
13. Ning XL, Li YZ, Huo C, *et al*. X-ray Structure-Guided Discovery of a Potent, Orally Bioavailable, Dual Human Indoleamine/Tryptophan 2,3-Dioxygenase (hIDO/hTDO) Inhibitor That Shows Activity in a Mouse Model of Parkinson's Disease. J Med Chem. 2021; 64:8303-8332.
14. Sodhi RK, Bansal Y, Singh R, Saroj P, Bhandari R, Kumar B, Kuhad A. IDO-1 inhibition protects against neuroinflammation, oxidative stress and mitochondrial dysfunction in 6-OHDA induced murine model of Parkinson's disease. Neurotoxicology. 2021; 84:184-197.
15. Mazarei G, Leavitt BR. Indoleamine 2,3 Dioxygenase as a Potential Therapeutic Target in Huntington's Disease. J Huntingtons Dis. 2015; 4:109-118.
16. Kennedy PJ, Cryan JF, Dinan TG, Clarke G. Kynurenine pathway metabolism and the microbiota-gut-brain axis. Neuropharmacology. 2017; 112:399-412.
17. Venkatesan D, Iyer M, Narayanasamy A, Siva K, Vellingiri B. Kynurenine pathway in Parkinson's disease-An update. eNeurologicalSci. 2020; 21:100270.
18. Nozaki T, Sugiyama K, Asakawa T, Namba H, Yokokura M, Terada T, Bunai T, Ouchi Y. Increased anteroventral striatal dopamine transporter and motor recovery after subthalamic deep brain stimulation in Parkinson's disease. J Neurosurg. 2021; 1-11.
19. Nozaki T, Asakawa T, Sugiyama K, Koda Y, Shimoda A, Mizushima T, Sameshima T, Namba H. Effect of Subthalamic Deep Brain Stimulation on Upper Limb Dexterity in Patients with Parkinson Disease. World Neurosurg. 2018; 115:e206-e217.
20. Nozaki T, Sugiyama K, Yagi S, Yoshikawa E, Kanno T, Asakawa T, Ito T, Terada T, Namba H, Ouchi Y. Effect of subthalamic nucleus stimulation during exercise on the mesolimbocortical dopaminergic region in Parkinson's disease: a positron emission tomography study. J Cereb Blood Flow Metab. 2013; 33:415-421.
21. Fang X, Sugiyama K, Akamine S, Namba H. The stepping test and its learning process in different degrees of unilateral striatal lesions by 6-hydroxydopamine in rats. Neurosci Res. 2006; 55:403-409.
22. Fang X, Sugiyama K, Akamine S, Namba H. Improvements in motor behavioral tests during deep brain stimulation of the subthalamic nucleus in rats with different degrees of unilateral parkinsonism. Brain Res. 2006; 1120:202-210.
23. Sun W, Sugiyama K, Fang X, Yamaguchi H, Akamine S, Magata Y, Namba H. Different striatal D2-like receptor function in an early stage after unilateral striatal lesion and medial forebrain bundle lesion in rats. Brain Res. 2010; 1317:227-235.
24. Kobayashi S, Asakawa T, Nozaki T, Sugiyama K, Sameshima T, Kurozumi K. Development of a novel gripping test for the evaluation of the finger fine motor ability in MPTP-treated monkeys. J Integr Neurosci. 2020; 19:209-215.
25. Asakawa T, Sugiyama K, Akamine S, Yokoyama C, Shukuri M, Mizuma H, Tsukada H, Onoe H, Namba H. The food reaching test: a sensitive test of behavioral improvements by deep brain stimulation in MPTP-treated monkey. Neurosci Res. 2012; 74:122-128.
26. Jiang X, Wang J, Chang H, Zhou Y. Recombinant expression, purification and crystallographic studies of the mature form of human mitochondrial aspartate aminotransferase. Biosci Trends. 2016; 10:79-84.
27. Shishikura M, Hakariya H, Iwasa S, Yoshio T, Ichiba H, Yorita K, Fukui K, Fukushima T. Evaluation of human D-amino acid oxidase inhibition by anti-psychotic drugs *in vitro*. Biosci Trends. 2014; 8:149-154.
28. Kozaki A, Iwasa S, Hosoda S, Nishiguchi Y, Nakayama M, Ichiba H, Fukushima T. Fluorimetric assay for D-amino acid oxidase activity in rat brain homogenate by using D-kynurenine as a substrate. Biosci Trends. 2012; 6:241-247.
29. Stone TW, Perkins MN. Quinolinic acid: a potent endogenous excitant at amino acid receptors in CNS. Eur J Pharmacol. 1981; 72:411-412.
30. Kessler M, Terramani T, Lynch G, Baudry M. A glycine site associated with N-methyl-D-aspartic acid receptors: characterization and identification of a new class of antagonists. J Neurochem. 1989; 52:1319-1328.
31. Bahraoui E, Serrero M, Planes R. HIV-1 Tat - TLR4/MD2 interaction drives the expression of IDO-1 in monocytes derived dendritic cells through NF-kappaB dependent pathway. Sci Rep. 2020; 10:8177.
32. Kang A, Hao H, Zheng X, Liang Y, Xie Y, Xie T, Dai C, Zhao Q, Wu X, Xie L, Wang G. Peripheral anti-inflammatory effects explain the ginsenosides paradox between poor brain distribution and anti-depression efficacy. J Neuroinflammation. 2011; 8:100.
33. Huang YS, Ogbechi J, Clanchy FI, Williams RO, Stone TW. IDO and Kynurenine Metabolites in Peripheral and CNS Disorders. Front Immunol. 2020; 11:388.
34. Santiago-Lopez D, Vazquez-Roman B, Perez-de La Cruz V, Barrera D, Rembao D, Salinas-Lara C, Pedraza-Chaverri J, Galvan-Arzate S, Ali SF, Santamaria A. Peroxynitrite decomposition catalyst, iron metalloporphyrin, reduces quinolinate-induced neurotoxicity in rats. Synapse. 2004; 54:233-238.
35. Stone TW. Neuropharmacology of quinolinic and kynurenic acids. Pharmacol Rev. 1993; 45:309-379.
36. Bratek-Gerej E, Ziembowicz A, Godlewski J, Salinska E. The Mechanism of the Neuroprotective Effect of Kynurenic Acid in the Experimental Model of Neonatal Hypoxia-Ischemia: The Link to Oxidative Stress.

Antioxidants (Basel). 2021; 10.
37. Ieraci A, Beggiato S, Ferraro L, Barbieri SS, Popoli M. Kynurenine pathway is altered in BDNF Val66Met knock-in mice: Effect of physical exercise. Brain Behav Immun. 2020; 89:440-450.
38. Duan Z, Zhang S, Liang H, Xing Z, Guo L, Shi L, Du L, Kuang C, Takikawa O, Yang Q. Amyloid beta neurotoxicity is IDO1-Kyn-AhR dependent and blocked by IDO1 inhibitor. Signal Transduct Target Ther. 2020; 5:96.
39. Park JH, Kim DW, Shin MJ, *et al*. Tat-indoleamine 2,3-dioxygenase 1 elicits neuroprotective effects on ischemic injury. BMB Rep. 2020; 53:582-587.
40. Ogawa T, Matson WR, Beal MF, Myers RH, Bird ED, Milbury P, Saso S. Kynurenine pathway abnormalities in Parkinson's disease. Neurology. 1992; 42:1702-1706.
41. Miranda AF, Boegman RJ, Beninger RJ, Jhamandas K. Protection against quinolinic acid-mediated excitotoxicity in nigrostriatal dopaminergic neurons by endogenous kynurenic acid. Neuroscience. 1997; 78:967-975.
42. Zadori D, Klivenyi P, Plangar I, Toldi J, Vecsei L. Endogenous neuroprotection in chronic neurodegenerative disorders: with particular regard to the kynurenines. J Cell Mol Med. 2011; 15:701-717.
43. Braidy N, Guillemin GJ, Mansour H, Chan-Ling T, Grant R. Changes in kynurenine pathway metabolism in the brain, liver and kidney of aged female Wistar rats. The FEBS journal. 2011; 278:4425-4434.
44. Pérez-De La Cruz V, Carrillo-Mora P, Santamaría A. Quinolinic Acid, an endogenous molecule combining excitotoxicity, oxidative stress and other toxic mechanisms. Int J Tryptophan Res. 2012; 5:1-8.
45. Sas K, Szabó E, Vécsei L. Mitochondria, Oxidative Stress and the Kynurenine System, with a Focus on Ageing and Neuroprotection. Molecules (Basel, Switzerland). 2018; 23.
46. Mithaiwala MN, Santana-Coelho D, Porter GA, O'Connor JC. Neuroinflammation and the Kynurenine Pathway in CNS Disease: Molecular Mechanisms and Therapeutic Implications. Cells. 2021; 10.
47. Lovelace MD, Varney B, Sundaram G, Lennon MJ, Lim CK, Jacobs K, Guillemin GJ, Brew BJ. Recent evidence for an expanded role of the kynurenine pathway of tryptophan metabolism in neurological diseases. Neuropharmacology. 2017; 112:373-388.
48. Mulak A, Bonaz B. Brain-gut-microbiota axis in Parkinson's disease. World J Gastroenterol. 2015; 21:10609-10620.
49. Bu LL, Huang KX, Zheng DZ, Lin DY, Chen Y, Jing XN, Liang YR, Tao EX. Alpha-Synuclein Accumulation and Its Phosphorylation in the Enteric Nervous System of Patients Without Neurodegeneration: An Explorative Study. Front Aging Neurosci. 2020; 12:575481.
50. Bottner M, Zorenkov D, Hellwig I, Barrenschee M, Harde J, Fricke T, Deuschl G, Egberts JH, Becker T, Fritscher-Ravens A, Arlt A, Wedel T. Expression pattern and localization of alpha-synuclein in the human enteric nervous system. Neurobiol Dis. 2012; 48:474-480.
51. Gao J, Xu K, Liu H, Liu G, Bai M, Peng C, Li T, Yin Y. Impact of the Gut Microbiota on Intestinal Immunity Mediated by Tryptophan Metabolism. Front Cell Infect Microbiol. 2018; 8:13.
52. Wikoff WR, Anfora AT, Liu J, Schultz PG, Lesley SA, Peters EC, Siuzdak G. Metabolomics analysis reveals large effects of gut microflora on mammalian blood metabolites. Proc Natl Acad Sci U S A. 2009; 106:3698-3703.
53. Kubicova L, Hadacek F, Bachmann G, Weckwerth W, Chobot V. Coordination Complex Formation and Redox Properties of Kynurenic and Xanthurenic Acid Can Affect Brain Tissue Homeodynamics. Antioxidants (Basel). 2019; 8.
54. Eleftheriadis T, Pissas G, Filippidis G, Liakopoulos V, Stefanidis I. The Role of Indoleamine 2,3-Dioxygenase in Renal Tubular Epithelial Cells Senescence under Anoxia or Reoxygenation. Biomolecules. 2021; 11.
55. Burassakarn A, Srisathaporn S, Pientong C, Wongjampa W, Vatanasapt P, Patarapadungkit N, Ekalaksananan T. Exosomes-carrying Epstein-Barr virus-encoded small RNA-1 induces indoleamine 2, 3-dioxygenase expression in tumor-infiltrating macrophages of oral squamous-cell carcinomas and suppresses T-cell activity by activating RIG-I/IL-6/TNF-alpha pathway. Oral Oncol. 2021; 117:105279.
56. Salminen A. Role of indoleamine 2,3-dioxygenase 1 (IDO1) and kynurenine pathway in the regulation of the aging process. Ageing Res Rev. 2022; 75:101573.

Received August 8, 2022; Revised August 19, 2022; Accepted August 22, 2022.

**Address correspondence to:*
Tetsuya Asakawa, Institute of Neurology, The Third People's Hospital of Shenzhen, 29 Buji Bulan Road, Shenzhen, Guangdong Province 518112, China.
E-mail: asakawat1971@gmail.com

Xiaokang Jia, Department of Neurology, The Eighth Affiliated Hospital, Sun Yat-Sen University. Shennanzhong Road 3025, Shenzhen, Guangdong Province 518033, China.
E-mail: jaxk1107581673@163.com

Released online in J-STAGE as advance publication August 24, 2022.

Original Article

DOI: 10.5582/bst.2022.01242

Development of an *in vitro* insulin resistance dissociated model of hepatic steatosis by co-culture system

Jiangwei Xiao[1,2,3,§], Xiang Li[4,§], Zongbao Zhou[1,2,3], Shuwen Guan[1,2,3], Lingjian Zhuo[4,*], Botao Gao[1,2,3,*]

[1] Institute of Biological and Medical Engineering, Guangdong Academy of Sciences, Guangzhou, China;
[2] National Engineering Research Center for Healthcare Devices, Guangzhou, China;
[3] Guangdong Key Lab of Medical Electronic Instruments and Polymer Material Products, Guangzhou, China;
[4] Department of Emergency Medicine, Nanfang Hospital, Southern Medical University, Guangzhou, China.

SUMMARY The evidence shows that there is an associated relationship between hepatosteatosis and insulin resistance. While some existing genetic induction animal and patient models challenge this relationship, indicating that hepatosteatosis is dissociated from insulin resistance. However, the molecular mechanisms of this dissociation remain poorly understood due to a lack of available, reliable, and simplistic setup models. Currently, we used primary rat hepatocytes (rHPCs), co-cultured with rat hepatic stellate cells (HSC-T6) or human foreskin fibroblast cells (HFF-1) in stimulation with high insulin and glucose, to develop a model of steatosis charactered as dissociated lipid accumulation from insulin resistance. Oil-Red staining significantly showed intracellular lipid accumulated in the developed model. Gene expression of sterol regulatory element-binding protein 1c (*SREBP1c*) and elongase of very-long-chain fatty acids 6 (*ELOVL6*), key genes responsible for lipogenesis, were detected and obviously increased in this model. Inversely, the insulin resistance related genes expression included phosphoenolpyruvate carboxykinase 1 (*PCK1*), pyruvate dehydrogenase lipoamide kinase isozyme 4 (*PDK4*), and glucose-6-phosphatase (*G6pase*) were decreased, suggesting a dissociation relationship between steatosis and insulin resistance in the developed model. As well, the drug metabolism of this developed model was investigated and showed up-regulation of cytochrome P450 3A (*CYP3A*) and down-regulation of cytochrome P450 2E1 (*CYP2E1*) and cytochrome P450 1A2 (*CYP1A2*). Taken together, those results demonstrate that the in vitro model of dissociated steatosis from insulin resistance was successfully created by our co-cultured cells in high insulin and glucose medium, which will be a potential model for investigating the mechanism of insulin resistance dissociated steatosis, and discovering a novel drug for its treatment.

Keywords hepatic steatosis, *in vitro* model, co-culture, dissociation, insulin resistance

1. Introduction

Nonalcoholic fatty liver disease (NAFLD) is a chronic liver disease, with a worldwide prevalence of 25% (*1,2*), which is the spectrum from hepatic steatosis to nonalcoholic steatohepatitis (NASH), which eventually leads to liver cirrhosis and hepatocellular carcinoma (HCC) (*3*). Hepatic steatosis, the initial and benign reversible event of NAFLD, is characterized by the accumulation of fat in at least 5% of hepatocytes and becomes the main feature of all stages of NAFLD from Nonalcoholic fatty liver (NAFL) progressing to NASH (*4*). Importantly, previously accumulated evidence showed that 10-25% of hepatic steatosis patients progress to NASH (*3*). While at the initial stage of NAFLD, modification of lifestyles such as exercise and diet can effectively reverse hepatic steatosis, subsequently protecting hepatic steatosis progress to NASH (*5*). In conclusion, hepatic steatosis is a major concern stage of NAFLD, and dealing with it as early as possible can effectively protect its progress to NASH.

Insulin resistance is a basically pathogenic mechanism of NAFLD, obesity, and type 2 diabetes. Many epidemiology studies have shown that hepatosteatosis is strongly associated with obesity and type 2 diabetes mellitus, indicating that there is a mutual cause-and-effect relationship between hepatosteatosis and insulin resistance (*3,6,7*). For instance, existing

insulin resistance may drive hepatic lipogenesis and subsequently cause steatosis (*8*). Also, the accumulation of lipid species in intracellular hepatocytes can disrupt insulin signaling, leading to cause insulin resistance (*9,10*). In addition, all this cause-and-effect relationship between hepatosteatosis and insulin resistance was evidently confirmed by various genetic or environmental induction animal or *in vitro* models of hepatic steatosis (*3,11-14*). However, there were several genetic or environmental induction animal models challenging this association of hepatosteatosis with insulin resistance. For instance, liver-specific knock out of insulin receptor (*15*), phosphoinositide 3-kinases (*PI3Ks*) (*16,17*), and protein kinase B (*AKT*) (*18*) or liver-specific deletion of phosphatase and tensin homolog (*PTEN*) (*19*) mice clearly display dissociation of hepatosteatosis from insulin resistance. Although the dissociation relationship is apparently displayed by those genetic animal models, the exact mechanism of this dissociation is still largely unknown. Therefore, for clearly elucidating the molecular mechanism of this dissociation relationship between hepatosteatosis and insulin resistance, a new experimental approach, animal model, or even an *in vitro* cell model will be urgently needed to explore or develop.

In general, for understanding the mechanism of NAFLD, animal models were first considered to be used and became the most common application experiment method in laboratory research. However, it is currently acknowledged that NAFLD is a complex multiple hit disease, and the developed *in vivo* animal models could not fully recapitulate the complexity of disease characteristics, thus hindering elucidation of the disease mechanism. In addition, the complex environment *in vivo* obstructs exploration of the exact disease mechanism. Therefore, *in vitro* models of fatty liver disease have been considered and continuously developed during the last few decades. For instance, immortalized cell lines or primary hepatocytes were cultured to develop models and well-established to be used for NAFLD research (*13,20*). Unfortunately, the above models developed from single cell cultures still failed to model the complex NAFLD pathogenesis because *in vivo* NAFLD pathogenesis is caused by numerous cellular communications between hepatocytes and nonparenchymal cells including HSCs, endothelial cells, or Kupffer cells. Hence, co-culture of two or more different cells is an interesting method to model continuous NAFLD pathogenesis, and it succeeded by culture of hepatocytes and HSC, which further found that co-culture with HSC can promote differentiation of the hepatocyte to maintain liver-specific functions and structure (*21*). Moreover, contrary to animal models developed in a hyperglycemic-hyperinsulinemic environment, there are rare and unsuccessful high concentration insulin-glucose induced *in vitro* cell culture models of hepatic steatosis. Consequently, for mimicking the pathogenesis of animal or human NAFLD, developing an *in vitro* hepatosteatosis model by co-culturing cells with a high concentration of insulin-glucose should be further explored, thus helping to investigate the exact molecular mechanisms involved in pathogenesis of NAFLD.

Therefore, in this study, we used rHPCs, co-cultured with HSC-T6 or HFF-1 cells under a high concentration of insulin-glucose conditions to develop an *in vitro* model of hepatic steatosis, which dissociated from insulin resistance for potentially investigating the dissociation mechanism. The developed model displayed obvious intracytoplasmatic lipid droplet accumulation and gradual growth into macrovesicular lipid vacuoles. Notably, the analysis of genes of *de novo* lipogenesis (DNL) significantly showed that the infiltrated fatty was caused by up-regulating *SREBP1c* and *ELOVL6*. Furthermore, the *CYPs*, *PCK1*, *PDK4*, and *G6pase* gene analysis suggested that rHPCs' drug-metabolism function was altered in the co-culture system, and the developed hepatosteatosis was dissociated from insulin resistance. Together, the results indicate that the co-culture system used is an effective approach to develop an *in vitro* insulin resistance dissociated hepatic steatosis model, which will potentially be used to investigate the dissociation mechanism and develop a novel drug for its treatment.

2. Materials and Methods

2.1. Isolation of primary rat hepatocytes

A two-step collagenase perfusion method was used to isolate primary hepatocytes from Wister rats. Briefly, after anesthetizing and sterilizing, the abdominal cavity of rats was opened to expose the portal vein and the inferior vena cava. Sequentially, the catheter was placed into the portal vein, and continuously pre-warmed Hank's Balanced Salt Solution (Gibco, New York, USA) containing EGTA (Coolaber, Beijing, China) and Digestion Medium including Type IV collagenase (Coolaber, Beijing, China) were perfused at 25-30 mL/min. After perfusion, the liver was carefully and integrally gathered and transferred to a culture dish containing Digestion Medium. Then, the liver capsule was torn by ophthalmic forceps and constantly shaked to dissociate liver cells into the medium. After dissociation, the hepatocyte suspension was filtered through a 70 μm filter and separated by centrifugation at a speed of 50 g for 2 min. Finally, Percoll gradient centrifugation was performed to purify the isolated hepatocytes.

2.2. Cells cultures

Isolated hepatocytes were stained with trypan blue and subsequently counted to calculate the number of alive

hepatocytes. After counting, 8×10^5 hepatocytes were seeded on a culture dish and cultured in an adherent medium, which contained DMEM (Gibco, New York, USA), 10% fetal bovine serum (FBS, Gibco, New York, USA), 1% penicillin-streptomycin (Gibco, New York, USA), 1% ITS (Insulin, Transferrin, and Selenium) (Cyagen, Guangzhou, China), 15mM HEPES (1M, Gibco, New York, USA) and 1 μM dexamethasone (Solarbio, Beijing, China). After 4h adhesion, the rat hepatic primary cells (rHPCs) were washed with PBS twice to remove non adhering rHPCs. Then the adhering rHPCs were subsequently cultured for another 20h with an adherent medium. For co-culture with rHPCs, HSC-T6 (rat hepatic stellate cells, purchased from Conservation Genetics CAS Kunming Cell Bank, Kunming, China) and HFF-1(human foreskin fibroblasts, purchased from Stem Cell Bank, Chinese Academy of Sciences, Shanghai, China) were previously cultured in DMEM (Gibco, New York, USA) containing 10% or 15% fetal bovine serum and 1% penicillin-streptomycin. Then HSC-T6 or HFF-1 cells were added into the cultured rHPCs while the medium was switched to steatosis-inducing medium containing DMEM, 10% fetal bovine serum, 1% penicillin-streptomycin, 1% ITS, 15 mM HEPEs, 1 μM dexamethasone and 0.002 μM glucagon (Yuanye Biotechnology, Shanghai, China) for 10d to induce fat accumulation in hepatocytes.

2.3. Hepatocyte Function assessment

To evaluate the function of hepatocytes in the co-culture system, the enzyme-linked immunosorbent assay kit (Ruixin Biotech, Fujian, China) and a biochemical assay kit (Jiancheng bioengineering, Nanjing, China) were used to detect and measure albumin and urea nitrogen. First, the cultured supernatant was collected and centrifuged at 4,000 rpm for 20 min. Then the centrifuged supernatant was used to detect albumin and urea nitrogen following the assay kits manufacturer's recommendations. Finally, the concentration of albumin and urea nitrogen were calculated according to a standard curve and established regression equation.

2.4. Oil Red O staning

For detecting accumulated lipid in intrahepatocytes, the Oil Red O stain kit (Solarbio, Beijing, China) was chosen. Following the kit manufacturer's instructions, the co-cultured cell models were washed twice with PBS, fixed in ORO Fixative solution for 30 min, washed twice again with PBS and 60% isopropanol, stained with ORO stain for 20 min and counterstained with Mayer hematoxylin for 2 min, and then washed with ORO buffer for 1 min. Finally, the images were captured using a light microscope (Leica Microsystems, Wetzlar, Germany). Representative photomicrographs are shown.

Table 1. Primer sequences used for PCR

Genes	Sequences
CYP2E1	F: 5'-TGTTTCTGCTCCTGTCTGCTATTCTG-3'
	R: 5'- TGGGATACTGCCAAAGCCAACTG-3'
CYP1A2	F: 5'- ACCATCTAATCAGCAAGTTCCAGAAGC-3'
	R: 5'- CCGATGACATTAGCCACCGATTCC-3'
CYP3A	F: 5'- CCGATGACATTAGCCACCGATTCC-3'
	R: 5'- TCCTCGTGCTCCTGTATCTGTATGG-3'
G6pase	F: 5'- AGGTGGTGGCTGGAGTCTTGTC-3'
	R: 5'- CTCTGGAGGCTGGCATTGTAGATG-3'
PDK4	F: 5'- GTTCTGAGGCTGATGACTGGTGTATC-3'
	R: 5'- GCACTGCCGTAGACCCACTTTG-3'
PCK1	F: 5'- GTGGAAAGTTGAATGTGTGGGTGATG -3'
	R: 5'- GTCTTAATGGCGTTCGGATTTGTCTTC -3'
Fads2	F: 5'- GAAGAAGACTGCTGAGGACATGAACC -3'
	R: 5'- CCATTGCCGAAGTACGAGAGGATG -3'
FASN	F: 5'- GTGTGGTAGGCTTGGTGAACTGTC-3'
	R: 5'- GTGAGATGTGCTGCTGAGGTTGG-3'
Dgat2	F: 5'- ACTCCTCTTCTCCAATCTGAGCCTAC-3'
	R: 5'- TGTGTTCACGATGCCAATCTCCAG-3'
ACC2	F: 5'- GAGTCCATCTTCCTGTCAGCCATTG -3'
	R: 5'- CGCCATACAGACGACCTTGTTAGC -3'
SCD1	F: 5'- TGTCAAAGAGAAGGGCGGAAAGC -3'
	R: 5'- CAGGATGAAGCACATGAGCAGGAG -3'
SREBP1	F: 5'- GCCTCATCTGATTGCCATCCTTCC-3'
	R: 5'- TCAACATACCGCACAAGGCAGAAG-3'
ELOVL6	F: 5'- CTTCCTCTTCCTCAACTTCTACACTCG-3'
	R: 5'- TTCTCTGACTTGTTCACACCGTTCG-3'
ChREBP	F: 5'- GCTGAACAACGCCATCTGGAGAG-3'
	R: 5'- GCAGAGGAGTTACGAAGCCACATAC-3'
GAPDH	F: 5'- TCTCTGCTCCTCCCTGTTCT -3'
	R: 5'- CCGATACGGCCAAATCCGTT -3'

F, Forward, R, Reverse.

2.5. RNA isolation and qRT-PCR

Total RNAs of cell models were extracted using TRIZOL reagent (Invitrogen, California, USA) according to the manufacturer's instructions. Then 1μg of extracted RNA was reverse transcribed into cDNA following the manufacturer's instructions of RevertAid First Stand cDNA Synthesis Kit (Thermo Scientific, Massachusetts, USA). Then, the cDNAs were quantified by performing quantitative real-time PCR using SYBR Green Master Mix (Genstar, Beijing, China) on ABI StepOnePlus real-time PCR system (Applied Biosystems, Waltham Mass, USA). All sense and antisense primers used for the PCR assays are provided in Table 1. All q-PCR data was collected and calculated as described previously (*22*).

2.6. Statistical analysis

SPSS ver. 20.0 (IBM, Armonk, New York, USA) software was used to perform One-way ANOVA Test for multiple comparisons. Statistical analysis data is displayed as bar graph using GraphPad prism5 (GraphPad Software, California, USA). Also, the data is shown as mean ± standard deviation. Meanwhile, statistically significant values of all the data were set as $P < 0.05$.

3. Results

3.1. rHPCs and HSC-T6 or HFF-1 cells (5:1 ratio) co-culture promotes lipid droplets accumulation

For optimizing co-culture system to develop hepatocyte steatosis, different ratios of rHPCs and HSC-T6 or HFF-1 cells were co-cultured. As shown in Figure 1, the intracellular rHPCs appeared with fat deposition on day 3 and significantly increased with time. However, the proportion of accumulation lipid droplets in a ratio of 3:1 and 4:1 was obviously lower than 5:1 and 6:1 groups, which means that greater hepatocyte numbers in the co-culture system will promote lipid droplets accumulation in hepatocytes. Meanwhile, the optical microscope results showed that the micro lipid droplets gradually grew into macro lipid droplets with increased co-culture time, especially in the ratio 5:1 group. (Figure 1) In line with optical microscope results, Oil Red O staining also showed that the fat deposition gradually increased in intracellular rHPCs (Figure 2A) and continuedly grew into a macro lipid droplet, particularly in the ratio 5:1 group. (Figure 2B) Together, the results indicate that the rHPCs and HSC-T6 or HFF-1 cells (5:1 ratio) co-culture can significantly promote rHPCs intracellular lipid droplets accumulation.

3.2. rHPCs and HSC-T6 or HFF-1 cells co-culture protects hepatocellular functions and alters cytochrome P450s genes expression

Maintaining hepatocellular functions *in vitro* plays a pivotal role in developing liver disease models. Therefore, in order to confirm that the functions of the isolated rHPCs were kept in this developed steatosis model, the secreted albumin, urea nitrogen and gene expression of *CYP3A* were measured. The results showed that the albumin was stably secreted until day 7 in the rHPCs and HSC-T6 cells co-culture model, and then it was significantly decreased on day 10 compared to day 0. (Figure 3A) Similarly, in the rHPCs and HFF-1 cells co-culture model, the secreted albumin did not show a significant decline on days 3, 5, 7 or even 10 when compared to day 0. (Figure 3B) Contrary to albumin, the secretion of urea nitrogen was significantly increased on days 3, 5, 7 and 10 when compared to normal hepatocytes (day 0) (Figure 4) In line with urea nitrogen secretion, the gene expression of *CYP3A*,

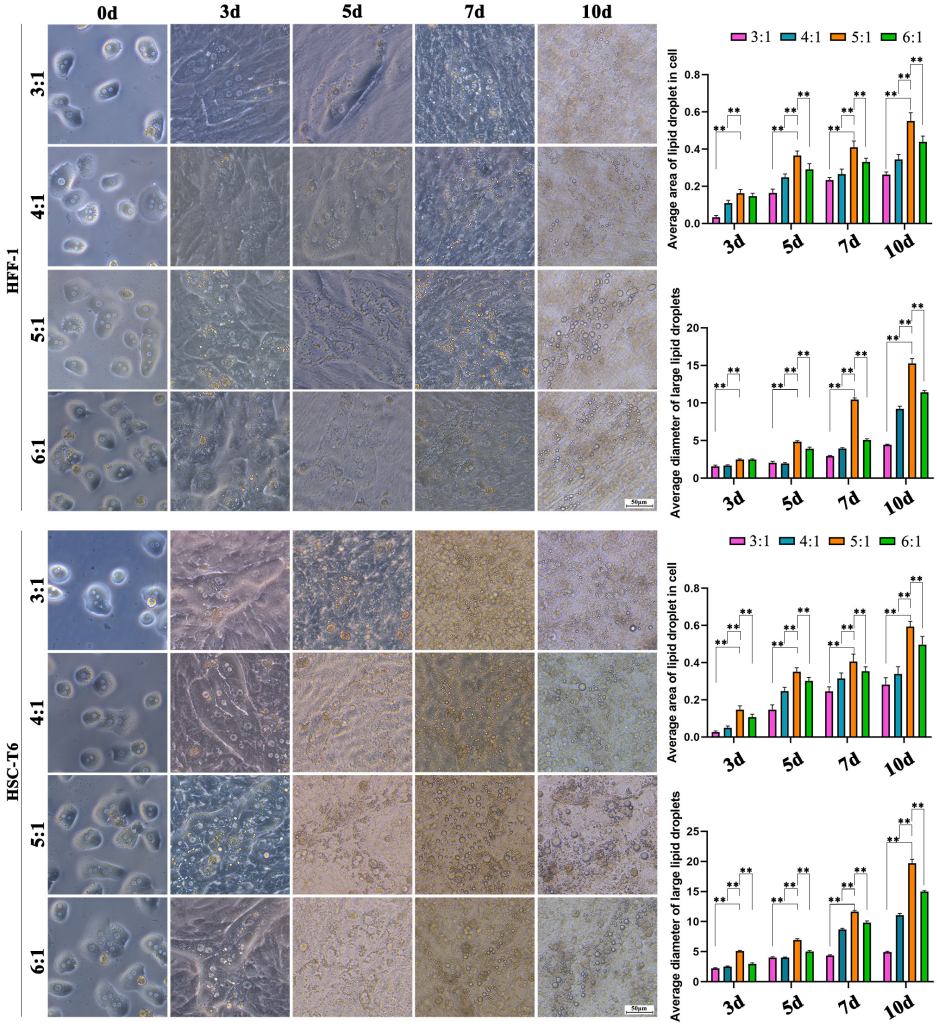

Figure 1. Optical microscope observation of fat deposition on different hepatocytes: HSC-T6 / HFF groups. All values are shown as mean ± standard deviation. ($^{*}P < 0.05$, $^{**}P < 0.01$). Bar = 50μm.

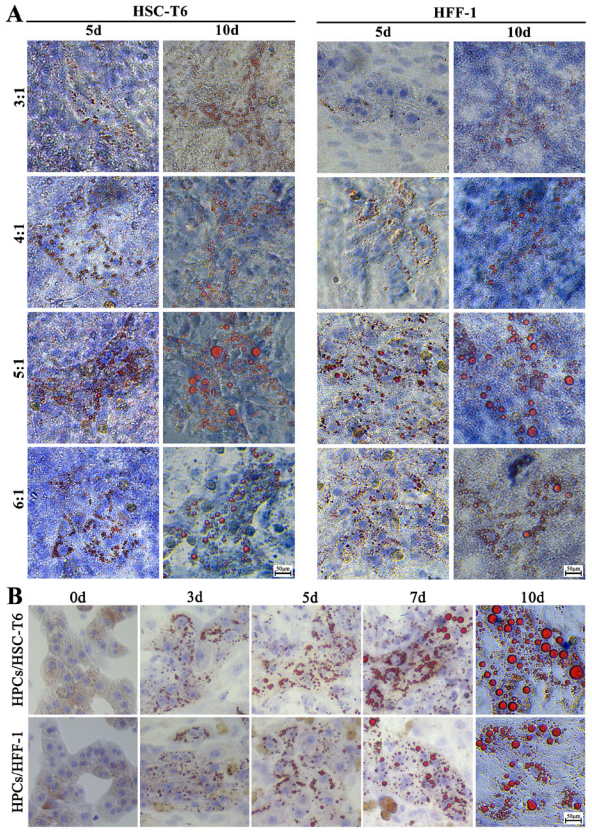

Figure 2. Oil Red O staining for developed steatosis model. A: Effect of hepatocytes ratio on fat deposition. **B**: Oil Red O staining detects the fat deposition and the change in lipid droplet size in ratio of 5:1 group (hepatocytes: HSC-T6 / HFF). Bar = 50μm.

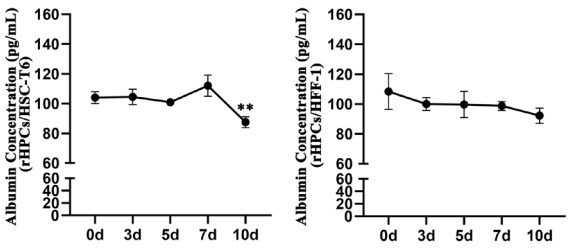

Figure 3. The secretion of albumin from hepatocytes in the developed steatosis model. All values are shown as mean ± standard deviation. ($^{*}P < 0.05$, $^{**}P < 0.01$).

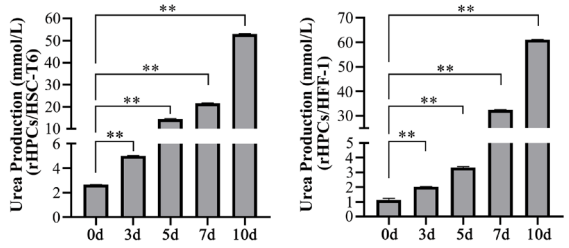

Figure 4. The secretion of urea nitrogen from hepatocytes in developed steatosis model. All values are shown as mean ± standard deviation. ($^{*}P < 0.05$, $^{**}P < 0.01$).

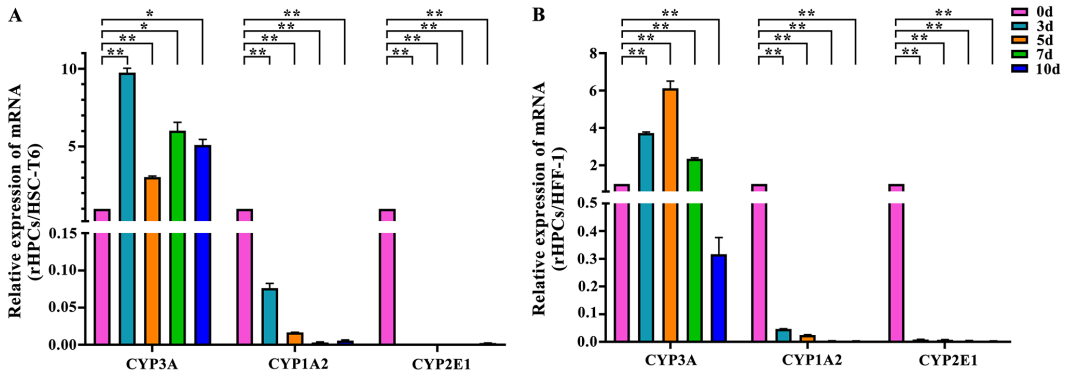

Figure 5. The genes expression of *CYP3A*, *CYP1A2* and *CYP1E* in developed steatosis model. All values are shown as mean ± standard deviation. ($^{*}P < 0.05$, $^{**}P < 0.01$).

quantitatively the most abundant component of human P-450, was also increased. The result showed that it was significantly up-regulated with intracellular lipid accumulation, and reached the highest level on day 3, after which its expression was decreased but higher than normal hepatocytes (day 0). (Figure 5A) However, in the HFF-1 co-culture system, although the *CYP3A* mRNA expression level was also increased, its highest level s appeared on day 5, then began to decrease and significantly was down-regulated compared to normal hepatocytes on day 10. (Figure 5B) In conclusion, the above results suggest that HSC-T6 or HFF-1 cells co-cultured with rHPCs can maintain or even enhance hepatocellular functions *in vitro*.

Furthermore, in humans, CYPs, which function as powerful detox enzymes play a vital role in drug metabolism and bioactivation. Therefore, in addition to CYP3A, other CYPs genes expression such as CYP1A2, which constitutes approximately 15% of total hepatic CYP enzymes, and *CYP2E1*, a major hepatic CYP enzyme involved in the metabolism and bioactivation of several drugs and toxicants, were also analyzed in this

study developed models. Hence the results showed that they were continually and obviously decreased in all HSC-T6 or HFF-1 developed models. (Figure 5A and B) Thus the results suggest that although the hepatocellular functions were protected in developed models, the related drug metabolism CYPs genes expression was altered.

3.3. The lipogenesis gene of *SREBP1c* and *ELOVL6* contributes to hepatosteatosis

Previous studies have reported that liver fat accumulation was linked to DNL (*23*). Therefore, in our developed model, we observed whether the DNL affects contributes to develop hepatosteatosis. To better understand that, the lipogenesis genes expression in the steatotic rHPCs were analyzed, and the results showed that only *SREBP1c*, generally recognized as master activator of lipid synthesis, and *ELOVL6*, an enzyme catalyzing the elongation of palmitate to stearate, were up-regulated. (Figure 6A, B) The up-regulation of *SREBP1c* was basically consistent between the HSC-T6 co-culture system and the HFF-1 system, while the *ELOVL6* up-regulation state was distinctly different between the two cells co-culture system. Because in the HSC-T6 system, *ELOVL6* was sustainably up-regulated from the initial to the day of 10, but in the HFF-1 system, *ELOVL6* genes expression was decreased on days of 3 and 5, and then it continued to increase. On the contrary, other DNL genes including carbohydrate responsive element binding protein (*ChREBP*), diacylglycerol acetyltransferase 2 (*Dgat2*), stearyl CoA desaturase 1 (*SCD1*), sstearyl CoA carboxylase 2 (*ACC2*), fatty acid synthase (*FASN*), and fatty acid desaturase 2 (*Fads2*) were down-regulation in all rHPCs and HSC-T6 or HFF-1 co-culture system. (Figure 6C) Consequently, expression of the above genes demonstrates that *SREBP1c* and *ELOVL6* were correlated with rHPCs steatosis development in the HSC-T6 or HFF-1 co-culture system.

3.4. The hepatosteatosis is dissociated from insulin resistance

Steatosis is strongly associated with insulin resistance and there is a mutual cause-and-effect relationship between hepatosteatosis and insulin resistance (*24*). Therefore, to better understand the relationship between hepatosteatosis and insulin resistance in our co-culture model, we examined the level of genes of *PCK1*, encoding the main checkpoint enzyme for the control of gluconeogenesis, *PDK4*, and G6pase, encoding an important enzyme for glycogenolysis and glucose production. The analysis results showed that gene expression of *PCK1*, *PDK4*, and *G6pase* were significantly decreased compared to normal hepatocytes in all rHPCs and HSC-T6 or HFF-1 co-culture systems, (Figure 7) suggesting that in those developed models, the

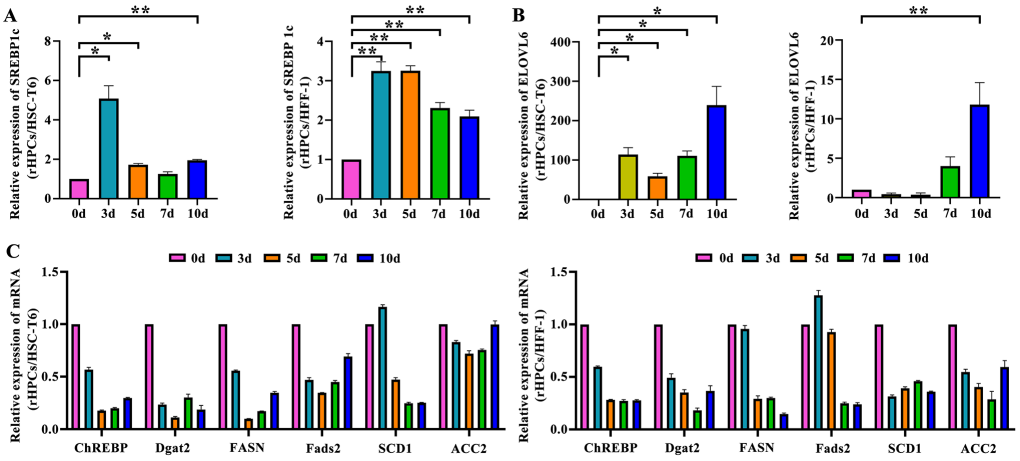

Figure 6. The *de novo* lipogenesis genes expression in developed steatosis model. A, B: the mRNA levels of *SREBP1c* and *ELOVL6* gene, as quantified by qRT-PCR, in hepatocytes. **C**: the other genes expression, including *ChREBP*, *Dgat2*, *FASN*, *Fads2*, *SCD1* and *ACC2*, in hepatocytes. All values are shown as mean ± standard deviation. ($^{*}P < 0.05$, $^{**}P < 0.01$).

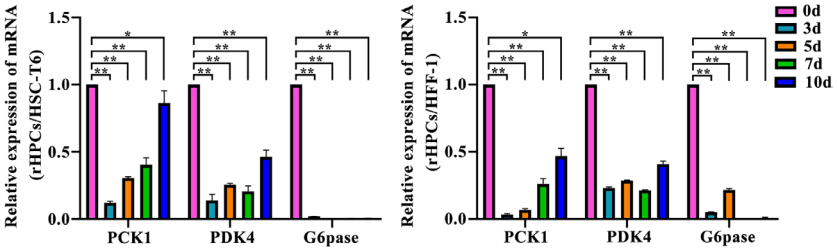

Figure 7. The genes expression of *PCK1*, *PDK4* and *G6pase* in developed steatosis model. All values are shown as mean ± standard deviation. ($^{*}P < 0.05$, $^{**}P < 0.01$).

hepatosteatosis is dissociated from insulin resistance.

4. Discussion

Epidemiology studies have reported that there is a mutual cause-and-effect relationship between hepatosteatosis and insulin resistance (*3,11-14*). However, this relationship in NAFLD was challenged by some genetic animal models and clinical patients (*15-19,25,26*), and the exact mechanistic basis of this dissociation relationship is still incompletely understood due to the lack of an ideal and simplistic setup model to elucidate this dissociation mechanism. Therefore, in this study, we used a co-culture system to develop an *in vitro* hepatic steatosis cell culture model. We found that the rHPCs and HSC-T6 or HFF-1 cells (5:1 ratio) co-culture can protect hepatocytes function and significantly promote rHPCs intracellular lipid droplets accumulation. Also, the developed hepetasteatosis was correlated with gene expression of *SREBP1c* and *ELOVEL6* and, importantly, was dissociated from insulin resistance due to the down-regulation of gene expression of *PCK1*, *PDK4* and *G6pase*. All results suggest that our approach used would be an ideal and simplistic method to develop an insulin resistance dissociated hepatosteatosis model, which will be a suitable *in vitro* model to elucidate the dissociation mechanism.

Generally, the disease of NAFLD happening and progression is a complex and multicellular event, because the liver fat accumulation, and inflammation or fibrosis is a result of the interaction between two or more cells (*13*). Therefore, in this study, we cultured rHPCs and HSC-T6 to develop steatosis and explore this interaction. As well to declare that the induced results such as the gene expression of DNL, *PCK1*, *PDK4*, *G6pase*, and CYPs were not coming from HSC-T6 cells, the heterogenous HFF-1cells were cultured with rHPCs and set as a control for HSC-T6 developed models. Then the results showed that the co-culture can prolong rHPCs culture *in vitro* to 15d compared to rHPCs culture alone (data not shown). In addition, the co-culture can protect hepatocyte functions, which may be due to cell contact and soluble factors production from HSC-T6 or HFF-1. Previous studies have proved that co-culture hepatocytes with HSC can maintain hepatocyte liver-specific functions and structure through cell contact and soluble factors (*21,27*). Similarly, previous study also showed that HFF-1 was a feeder cell that can maintain stem cell features (*i.e.*, pluripotency, immortality, and unlimited undifferentiated proliferation capability) when they were cultured with stem cells (*28*). Moreover, in this study we used high insulin and glucose medium, not free fatty acid (*13,29,30*), to develop steatosis, which was enlightened by developing animal NAFLD models through dieting low fat/high carbohydrate to mimic clinical patients hyperglycemic-hyperinsulinemic pathogenicity environment, and also to avoid free fatty acid to cause a negative effect on hepatocytes by generating cytotoxicity and caspase-dependent apoptosis (*31,32*).

Hepatic DNL plays a vital role in contributing to steatosis. As well, in this successful developed model, we proved that its steatosis development was regulated by gene expression of *SREBP1c* and *ELOVL6*, which is in line with previous reports, which showed that *SREBP1c* is a key transcription factor regulating lipid metabolism (*33,34*). However, those studies have shown that its regulation is through increasing its downstream fatty acid synthesis genes including *ACC, FASN*, *SCD1* and *ELOVL6* (*35,36*). While in our model, we only found the *ELOVL6* gene was up-regulated, and the other lipogenesis genes such as *ACC*, *FASN*, *SCD1*, *Fasd* and *Dgat2* were not increased. Consistent with those gene expressions, *ChREBP*, another major factor that regulates fatty acid synthesis, also showed down-regulation, which means that the down-regulation of *ACC*, *FASN*, *SCD1*, *Fasd* and *Dgat2* may be regulated by *ChREBP*. Because previous studies have reported that *ChREBP* is also the upstream regulator of *ACC*, *FASN*, *SCD1* and *Fasd* (*35,36*). Therefore, in our model, hepatosteatosis development may be regulated through *SREBP1c* and *ELOVL6* gene expression, not *ChREBP*, *ACC*, *FASN*, *SCD1* and *Fasd*. While its exact mechanism needs to be further explored.

Insulin resistance has been characterized as the crucial pathophysiological factor and tightly associated with every stage of NAFLD (*3,6-8*). However, this association was challenged by clinical and genetic animal studies (*15-19,25,26*), showing that hepatosteatosis is dissociated from insulin resistance. As well, in this study, we used the co-culture system successfully to develop hepatosteatosis, and further gene detection of *SREBP1c*, *ELOVEL6*, *PCK1*, *PDK4* and *G6pase* evidence confirmed that hepatosteatosis was dissociated from insulin resistance. The dissociation in this model was strongly confirmed by down-regulation of *DGAT2*. Because in previous studies, they found overexpression of *DGAT2* can cause hepatic insulin resistance in mice models of severe hepatic steatosis (*37,38*). Moreover, in insulin resistance obesity, the study also found that mice with deletion of X-box-binding protein-1(*XBP-1*) can lead to develop insulin resistance in HFD-dieted conditions (*39*), and the other study further found that the up-regulation of IκB kinase beta (IKKβ) activity in the liver of obese mice can increase XBP1s activity and reduce ER stress, resulting in a significant improvement in insulin sensitivity (*40*). In line with the above results, we also found that the gene expression of *XBP-1s* was up-regulated and the other ER stress-related genes were down-regulated in our developed model (data not shown). Therefore, we hypothesize that the mechanism of this insulin resistance dissociated from

hepatosteatosis might be caused by up-regulated XBP-1 or even by XBP-1 regulating its downstream pathways. Hence, the exact mechanism of this developed model should be further investigated in subsequent studies.

Cytochrome P450, mainly in families CYP1, CYP2, and CYP3, is the majority of enzymes in the liver to metabolize hepatically cleared drugs (*41*). Noteworthily, 75% of enzymatic reactions that occur in the metabolism of drugs are related to cytochrome P450s. As well, five genes of P450 are involved in the metabolism of more than 90% of the small-molecule drugs in use today (*42*), which suggests that P450s play a crucial role in considering new drug development. Therefore, in this study, we detected the genes expression of P450 including *CYP3A*, *CYP1A2*, and *CYP2E1*. The results showed that the expression of *CYP3A* was up-regulated, which was in line with the Onni Niemela et. al. clinical study results (*43*). However, this result is contrary to other recent clinical studies (*44*), leading to this opposite finding which may potentially be due to the two cells co-culture or insulin used in the culture system. Because previous studies have reported that co-cultured hepatocytes with endothelial cells can provide an optimal trophic support for the hepatocytes, which can improve functionality of hepatocytes such as cytochrome P450 activity and albumin secretion (*45,46*). As well, the other studies also have reported that the increase of *CYP3A* was caused by up-regulating of *NR1I2* (nuclear receptor subfamily 1, group I, member 2, also known as pregnane X receptor or *PXR)* transcript which could be overexpressed by induced insulin (*47,48*). Hence, the *CYP3A* increased in our developed model may be due to HSC-T6 of HFF-1 cells support or overexpression of *PXR* by induced insulin. On the contrary to expression of *CYP3A*, *CYP1A2* and *CYP2E1* were significantly down-regulated, and this result is in line with *in vitro* and clinical studies which showed that mRNA levels of *CYP1A2* and *CYP2E1* were decreased in hepatocytes or humans with progressive stages of NAFLD (*29,30,49*). Therefore, the expression characteristics of P450 in this developed model could guide development of novel therapeutic drugs for treating NAFLD, which is dissociated fatty accumulation from insulin resistance.

5. Conclusion

This study describes a co-culture approach to develop an *in vitro* model of steatosis, and validates that the hepatosteatosis was dissociated from insulin resistance. By co-culture rHPCs with HSC-T6 or HFF-1 in high insulin and glucose medium, we developed a simplistic set up of an *in vitro* hepatosteatosis model, and genes expression of *SREBP1c*, *ELOVL6*, *PCK1*, *PDK4* and *G6pase* validated that the model is successful and deeply shows that the steatosis is dissociated from insulin resistance. Taken together, these studies evidence that a high insulin and glucose stimulated co-culture system is a valuable approach for developing an *in vitro* hepatosteatosis model, which is dissociated from insulin resistance. In addition, this developed model will be a potential tool for investigating the molecular mechanism of the case of NAFLD, which dissociated from insulin resistance, thereby finding an effective and accurate therapeutic target for treatment.

Funding: This study was supported by Guangdong Basic and Applied Basic Research Foundation (2020A1515110054), Guangdong Academy of Sciences (Grant No. 2020GDASYL-20200102005; Grant No. 2021GDASYL-20210102004), China Postdoctoral Science Foundation (Grant No.2021M690746) and President Fund of Nanfang Hospital (2021C024; 2021C040).

Conflict of Interest: The authors have no conflicts of interest to disclose.

References

1. Luci C, Bourinet M, Leclere PS, Anty R, Gual P. Chronic Inflammation in Non-Alcoholic Steatohepatitis: Molecular Mechanisms and Therapeutic Strategies. Front Endocrinol (Lausanne). 2020; 11:597648.
2. Younossi ZM, Golabi P, de Avila L, Paik JM, Srishord M, Fukui N, Qiu Y, Burns L, Afendy A, Nader F. The global epidemiology of NAFLD and NASH in patients with type 2 diabetes: A systematic review and meta-analysis. J Hepatol. 2019; 71:793-801.
3. Willebrords J, Pereira IV, Maes M, Crespo Yanguas S, Colle I, Van Den Bossche B, Da Silva TC, de Oliveira CP, Andraus W, Alves VA, Cogliati B, Vinken M. Strategies, models and biomarkers in experimental non-alcoholic fatty liver disease research. Prog Lipid Res. 2015; 59:106-125.
4. Wang XJ, Malhi H. Nonalcoholic Fatty Liver Disease. Ann Intern Med. 2018; 169:ITC65-ITC80.
5. Thyfault JP, Rector RS. Exercise Combats Hepatic Steatosis: Potential Mechanisms and Clinical Implications. Diabetes. 2020; 69:517-524.
6. Sun Z, Lazar MA. Dissociating fatty liver and diabetes. Trends in endocrinology and metabolism: Trends Endocrinol Metab. 2013; 24:4-12.
7. Watt MJ, Miotto PM, De Nardo W, Montgomery MK. The Liver as an Endocrine Organ-Linking NAFLD and Insulin Resistance. Endocr Rev. 2019; 40:1367-1393.
8. Moore DD. Nuclear receptors reverse McGarry's vicious cycle to insulin resistance. Cell Metab. 2012; 15:615-622.
9. Samuel VT, Shulman GI. Mechanisms for insulin resistance: common threads and missing links. Cell. 2012; 148:852-871.
10. Chavez JA, Summers SA. A ceramide-centric view of insulin resistance. Cell Metab. 2012; 15:585-594.
11. Kumashiro N, Erion DM, Zhang D, Kahn M, Beddow SA, Chu X, Still CD, Gerhard GS, Han X, Dziura J, Petersen KF, Samuel VT, Shulman GI. Cellular mechanism of insulin resistance in nonalcoholic fatty liver disease. Proc Natl Acad Sci U S A. 2011; 108:16381-16385.

12. Samuel VT, Petersen KF, Shulman GI. Lipid-induced insulin resistance: unravelling the mechanism. Lancet. 2010; 375:2267-2277.
13. Gomez-Lechon MJ, Donato MT, Martinez-Romero A, Jimenez N, Castell JV, O'Connor JE. A human hepatocellular *in vitro* model to investigate steatosis. Chem Biol Interact. 2007; 165:106-116.
14. Peng C, Stewart AG, Woodman OL, Ritchie RH, Qin CX. Non-Alcoholic Steatohepatitis: A Review of Its Mechanism, Models and Medical Treatments. Front Pharmacol. 2020; 11:603926.
15. Biddinger SB, Hernandez-Ono A, Rask-Madsen C, Haas JT, Aleman JO, Suzuki R, Scapa EF, Agarwal C, Carey MC, Stephanopoulos G, Cohen DE, King GL, Ginsberg HN, Kahn CR. Hepatic insulin resistance is sufficient to produce dyslipidemia and susceptibility to atherosclerosis. Cell Metab. 2008; 7:125-134.
16. Taniguchi CM, Kondo T, Sajan M, Luo J, Bronson R, Asano T, Farese R, Cantley LC, Kahn CR. Divergent regulation of hepatic glucose and lipid metabolism by phosphoinositide 3-kinase *via* Akt and PKClambda/zeta. Cell Metab. 2006; 3:343-353.
17. Sopasakis VR, Liu P, Suzuki R, Kondo T, Winnay J, Tran TT, Asano T, Smyth G, Sajan MP, Farese RV, Kahn CR, Zhao JJ. Specific roles of the p110alpha isoform of phosphatidylinsositol 3-kinase in hepatic insulin signaling and metabolic regulation. Cell Metab. 2010; 11:220-230.
18. Leavens KF, Easton RM, Shulman GI, Previs SF, Birnbaum MJ. Akt2 is required for hepatic lipid accumulation in models of insulin resistance. Cell Metab. 2009; 10:405-418.
19. Stiles B, Wang Y, Stahl A, Bassilian S, Lee WP, Kim YJ, Sherwin R, Devaskar S, Lesche R, Magnuson MA, Wu H. Liver-specific deletion of negative regulator Pten results in fatty liver and insulin hypersensitivity [corrected]. Natl Acad Sci U S A. 2004; 101:2082-2087.
20. Gori M, Simonelli MC, Giannitelli SM, Businaro L, Trombetta M, Rainer A. Investigating Nonalcoholic Fatty Liver Disease in a Liver-on-a-Chip Microfluidic Device. PloS One. 2016; 11:e0159729.
21. Krause P, Saghatolislam F, Koenig S, Unthan-Fechner K, Probst I. Maintaining hepatocyte differentiation *in vitro* through co-culture with hepatic stellate cells. In Vitro Cell Dev Biol Anim. 2009; 45:205-212.
22. Gu R, Huang T, Xiao J, Liao Z, Li J, Lan H, Ouyang J, Hu J, Liao H. The IRE1alpha Arm of UPR Regulates Muscle Cells Immune Characters by Restraining p38 MAPK Activation. Front Physiol. 2019; 10:1198.
23. Lambert JE, Ramos-Roman MA, Browning JD, Parks EJ. Increased de novo lipogenesis is a distinct characteristic of individuals with nonalcoholic fatty liver disease. Gastroenterology. 2014; 146:726-735.
24. Khan RS, Bril F, Cusi K, Newsome PN. Modulation of Insulin Resistance in Nonalcoholic Fatty Liver Disease. Hepatology. 2019; 70:711-724.
25. Kantartzis K, Peter A, Machicao F, Machann J, Wagner S, Konigsrainer I, Konigsrainer A, Schick F, Fritsche A, Haring HU, Stefan N. Dissociation between fatty liver and insulin resistance in humans carrying a variant of the patatin-like phospholipase 3 gene. Diabetes. 2009; 58:2616-2623.
26. Peter A, Kovarova M, Nadalin S, Cermak T, Konigsrainer A, Machicao F, Stefan N, Haring HU, Schleicher E. PNPLA3 variant I148M is associated with altered hepatic lipid composition in humans. Diabetologia. 2014; 57:2103-2107.
27. Thomas RJ, Bhandari R, Barrett DA, Bennett AJ, Fry JR, Powe D, Thomson BJ, Shakesheff KM. The effect of three-dimensional co-culture of hepatocytes and hepatic stellate cells on key hepatocyte functions *in vitro*. Cells Tissues Organs. 2005; 181:67-79.
28. Amit M, Margulets V, Segev H, Shariki K, Laevsky I, Coleman R, Itskovitz-Eldor J. Human feeder layers for human embryonic stem cells. Biol Reprod. 2003; 68:2150-2156.
29. Donato MT, Jimenez N, Serralta A, Mir J, Castell JV, Gomez-Lechon MJ. Effects of steatosis on drug-metabolizing capability of primary human hepatocytes. Toxicol In Vitro. 2007; 21:271-276.
30. Donato MT, Lahoz A, Jimenez N, Perez G, Serralta A, Mir J, Castell JV, Gomez-Lechon MJ. Potential impact of steatosis on cytochrome P450 enzymes of human hepatocytes isolated from fatty liver grafts. Drug Metab Dispos. 2006; 34:1556-1562.
31. Malhi H, Bronk SF, Werneburg NW, Gores GJ. Free fatty acids induce JNK-dependent hepatocyte lipoapoptosis. J Biol Chem. 2006; 281:12093-12101.
32. Gentile CL, Pagliassotti MJ. The role of fatty acids in the development and progression of nonalcoholic fatty liver disease. J Nutr Biochem. 2008; 19:567-576.
33. Goldstein JL, DeBose-Boyd RA, Brown MS. Protein sensors for membrane sterols. Cell. 2006; 124:35-46.
34. Han Y, Hu Z, Cui A, *et al*. Post-translational regulation of lipogenesis *via* AMPK-dependent phosphorylation of insulin-induced gene. Nat Commun. 2019; 10:623.
35. Hodson L, Gunn PJ. The regulation of hepatic fatty acid synthesis and partitioning: the effect of nutritional state. Nat Rev Endocrinol. 2019; 15:689-700.
36. Sanders FW, Griffin JL. De novo lipogenesis in the liver in health and disease: more than just a shunting yard for glucose. Biol Rev Camb Philos Soc. 2016; 91:452-468.
37. Zhang Q, Huang Y, Li X, Liu H, He B, Wang B, Ma Y, Zhou X, Liu Y, Wu S. Tangduqing Granules Attenuate Insulin Resistance and Abnormal Lipid Metabolism through the Coordinated Regulation of PPARgamma and DGAT2 in Type 2 Diabetic Rats. J Diabetes Res. 2019; 2019:7403978.
38. Jornayvaz FR, Birkenfeld AL, Jurczak MJ, Kanda S, Guigni BA, Jiang DC, Zhang D, Lee HY, Samuel VT, Shulman GI. Hepatic insulin resistance in mice with hepatic overexpression of diacylglycerol acyltransferase 2. Natl Acad Sci U S A. 2011; 108:5748-5752.
39. Ozcan U, Cao Q, Yilmaz E, Lee AH, Iwakoshi NN, Ozdelen E, Tuncman G, Gorgun C, Glimcher LH, Hotamisligil GS. Endoplasmic reticulum stress links obesity, insulin action, and type 2 diabetes. Science. 2004; 306:457-461.
40. Liu J, Ibi D, Taniguchi K, Lee J, Herrema H, Akosman B, Mucka P, Salazar Hernandez MA, Uyar MF, Park SW, Karin M, Ozcan U. Inflammation Improves Glucose Homeostasis through IKKbeta-XBP1s Interaction. Cell. 2016; 167:1052-1066 e1018.
41. Tornio A, Backman JT. Cytochrome P450 in Pharmacogenetics: An Update. Adv Pharmacol. 2018; 83:3-32.
42. Guengerich FP, Waterman MR, Egli M. Recent Structural Insights into Cytochrome P450 Function. Trends Pharmacol Sci. 2016; 37:625-640.
43. Niemela O, Parkkila S, Juvonen RO, Viitala K, Gelboin HV, Pasanen M. Cytochromes P450 2A6, 2E1, and 3A

and production of protein-aldehyde adducts in the liver of patients with alcoholic and non-alcoholic liver diseases. J Hepatol. 2000; 33:893-901.
44. Jamwal R, de la Monte SM, Ogasawara K, Adusumalli S, Barlock BB, Akhlaghi F. Nonalcoholic Fatty Liver Disease and Diabetes Are Associated with Decreased CYP3A4 Protein Expression and Activity in Human Liver. Mol Pharm. 2018; 15:2621-2632.
45. Lasli S, Kim HJ, Lee K, Suurmond CE, Goudie M, Bandaru P, Sun W, Zhang S, Zhang N, Ahadian S, Dokmeci MR, Lee J, Khademhosseini A. A Human Liver-on-a-Chip Platform for Modeling Nonalcoholic Fatty Liver Disease. Adv Biosyst. 2019; 3:e1900104.
46. Beckwitt CH, Clark AM, Wheeler S, Taylor DL, Stolz DB, Griffith L, Wells A. Liver 'organ on a chip'. Exp Cell Res. 2018; 363:15-25.
47. Davidson MD, Ballinger KR, Khetani SR. Long-term exposure to abnormal glucose levels alters drug metabolism pathways and insulin sensitivity in primary human hepatocytes. Sci Rep. 2016; 6:28178.
48. Yang X, Zhang X, Liu Y, Xi T, Xiong J. Insulin transcriptionally down-regulates carboxylesterases through pregnane X receptor in an Akt-dependent manner. Toxicology. 2019; 422:60-68.
49. Fisher CD, Lickteig AJ, Augustine LM, Ranger-Moore J, Jackson JP, Ferguson SS, Cherrington NJ. Hepatic cytochrome P450 enzyme alterations in humans with progressive stages of nonalcoholic fatty liver disease. Drug Metab Dispos. 2009; 37:2087-2094.

Received June 1, 2022; Revised July 25, 2022; Accepted August 5, 2022.

[§]These authors contributed equally to this work.
*Address correspondence to:
Botao Gao, Institute of Biological and Medical Engineering, Guangdong Academy of Sciences, Guangzhou 510632, China.
E-mail: gaobotao1984@outlook.com

Lingjian Zhuo, Department of Emergency Medicine, Nanfang Hospital, Southern Medical University, Guangzhou 510515, China.
E-mail: 277682948@qq.com

Released online in J-STAGE as advance publication August 13, 2022.

Original Article

DOI: 10.5582/bst.2022.01281

Hepatic stellate cell exosome-derived circWDR25 promotes the progression of hepatocellular carcinoma *via* the miRNA-4474-3P-ALOX-15 and EMT axes

Lei Liu[1,2,§], Rui Liao[1,§,*], Zhongjun Wu[1,§], Chengyou Du[1,§], Yu You[3,4,§], Keting Que[3,4], Yuxin Duan[1], Kunli Yin[1], Wentao Ye[1]

[1] Department of Hepatobiliary Surgery, the First Affiliated Hospital of Chongqing Medical University, Chongqing, China;
[2] Department of Hepatobiliary Surgery, the People's Hospital of Yubei District of Chongqing City, Chongqing, China;
[3] Chongqing Key Laboratory of Hepatobiliary Surgery, The Second Affiliated Hospital of Chongqing Medical University, Chongqing, China;
[4] Department of Hepatobiliary Surgery, the Second Affiliated Hospital of Chongqing Medical University, Chongqing, China.

SUMMARY Recently, the emerging role of circular RNAs (circRNAs) in tumor development and progression has been a topic of great interest. Nevertheless, the effects of hepatic stellate cell (HSC)-derived exosomes in hepatocellular carcinoma (HCC) remain unclear. Here, we aim to explore the potential effect of HSC exosome-derived circWDR25 on the aggressiveness of HCC. Firstly, a microarray analysis of circRNAs was performed to profile and identify the differentially expressed circRNAs derived from HSC exosomes activated by HCC cells. Subsequently, the roles of circWDR25 in HCC tumor growth and aggressiveness were confirmed through *in vitro* and *in vivo* functional experiments. Moreover, RNA pull-down, dual-luciferase reporter assays, and fluorescent in situ hybridization (FISH) were performed to determine interactions in the circWDR25-miR-4474-3p-ALOX15 loop. Immunohistochemical analysis was also performed on a microarray of HCC tissues and peritumoral tissues. We found that overexpressed peritumoral circWDR25 was associated with survival and recurrence in patients with HCC and promoted the progression of HCC cells both *in vitro* and *in vivo*. Mechanistically, both exogenous and HSC exosomal-derived circWDR25 regulated the expression of ALOX15 by sponging miR-4474-3p and ultimately inducing an epithelial-to-mesenchymal transition (EMT) in HCC cells. Moreover, exogenous and HSC exosomal-derived circWDR25 promoted the expression of CTLA-4 in HSCs and PD-L1 in HCC cells. In conclusion, circWDR25 facilitated HCC cell proliferation and invasion *via* the circWDR25/miR-4474-3p/ALOX15 and EMT axes and it promoted the expression of CTLA-4 in HSCs and PD-L1 in HCC cells, thus providing insights into the mechanism of tumor aggressiveness mediated by HSC-derived exosomal circWDR25.

Keywords liver cancer, mesenchymal cells, extracellular vesicles, circular RNA, prognosis

1. Introduction

Hepatocellular carcinoma (HCC) is one of the most malignant tumors, accounting for approximately 90% of all cases of primary liver cancer, and it is gradually becoming the second deadliest tumor globally (*1-3*). Although rational approaches to the diagnosis and treatment of HCC have been developed, the long-term outcomes are unfortunately still generally poor due to its high metastatic ability as well as its high recurrence rate (*4-6*). Thus, understanding the molecular mechanisms of HCC, and especially the inflammatory/immune response or genetic regulatory networks in HCC microenvironments, is of paramount importance.

During HCC progression, activated hepatic stellate cells (HSCs) are thought to accelerate hepatocarcinogenesis by producing extracellular matrix proteins and inflammatory cytokines (*7*). Current studies have revealed the potential mechanisms involving activated HSCs driving hepatocarcinogenesis by affecting cell autophagy (*8*), proliferation (*9*), migration and invasion (*10*), and tumor angiogenesis (*11*). The current authors previously reported that the secretion of HSCs, such as IF-6-, TNF-α-, and TREM-1-mediated crosstalk with hepatoma cells, induces a fertile environment favoring HCC (*12-14*). That said, the current authors also found that the balancing relationship between HSCs and different infiltrating lymphocytes (*e.g.*, Th17 cells (*15*)

and γδT cells (*16*)) contributes to the aggressiveness and recurrence of HCC. However, the crucial role of HSCs in dictating the immunologic reaction to the tumor in an immunosuppressive network is still unclear.

Exosomes, a subset of small extracellular vesicles (EVs) with an average size of 100 nm (range: 40-160 nm), are important media for intercellular communication (*17*). Recently, a vast array of studies have suggested that in various tumor types, tumor-derived exosomes play an important role in information transmission between tumor cells and the corresponding microenvironment during tumor progression (*18,19*). In addition, exosomes derived from other different types of cells, such as macrophages (*20*), mast cells (*21*), fibroblasts (*22*), and mesenchymal stem cells (*23*), mediate bidirectional crosstalk with tumor cells. In HCC, tumor-derived exosomes have the power to activate HSCs by triggering Hedgehog (*24*) and PDK1/AKT signalling (*25*) to promote tumor progression. However, the roles of HSC-derived exosomes in tumor cells and the molecular mechanisms of exosomal HSCs in the oncogenesis and development of HCC are still unknown.

Circular RNAs (circRNAs) are newly classified endogenously expressed regulatory noncoding RNA (ncRNA) members with a single-stranded circular structure that contribute to cell growth, angiogenesis, unlimited replicative potential, and cancer development by sponging different miRNA sequesters (*26*). Mounting evidence corroborates the fact that circRNAs induce aberrant functions in the HCC tumor microenvironment and mediate tumor biology. For instance, circPABPC1 can inhibit tumor cell adhesion and migration by downregulating ITGB1 (β_1 integrin) in HCC (*27*). Intriguingly, a recent study revealed that circPSD3 inhibited the activation and proliferation of HSCs and subsequently alleviated hepatic fibrogenesis (*28*). However, the underlying function and mechanism of HSC exosome-derived circRNAs in cancer remain elusive.

Based on a microarray analysis of circRNA, the current study identified an HSC-derived exosomal oncogenic circRNA, termed circWDR25. Moreover, the current authors found that a high level of expression of peritumoral circWDR25 was associated with a poor prognosis for patients with HCC. Moreover, circWDR25 sponges miR-4474-3p to upregulate ALOX15 expression. Exogenous circWDR25 or HSC-derived exosomal circWDR25 promoted hepatoma cell proliferation, migration, and invasion and it induced EMT in hepatoma cells. Significantly, the current authors found that HSC-derived exosomal circWDR25 participated in the immune response in HCC microenvironments by increasing PD-L1 expression in hepatoma cells and CTLA-4 expression in activated HSCs. To the extent known, this study is the first to demonstrate that HSC-derived exosomal circWDR25 and its downstream target gene miR-4474-3p/ALOX15 play a considerable role in HCC progression and to provide novel potential targets and approaches for treating HCC.

2. Materials and Methods

2.1. Patients and specimens

All archival specimens were obtained from 348 patients who were pathologically confirmed to have HCC after R0 curative hepatectomy from January 2011 to December 2014. None of the patients had received prior anticancer therapy or had other malignancies. All patients were followed up until June 2021. This study was specifically approved by the Ethics Review Committee of the First Hospital Affiliated with Chongqing Medical University, and written informed consent was obtained from all participants.

2.2. Tissue microarray design, immunohistochemistry, and H&E staining

A tissue microarray (TMA) was constructed as described previously (*14*). Immunohistochemistry (IHC) was performed according to the manufacturer's instructions (Invitrogen, Zymed Polymer Detection System). Positively stained cells were observed under high-power magnification (400×).

2.3. Survival and correlation analysis

Recurrence-free survival (RFS) and overall survival (OS) in patients with HCC were analyzed using Kaplan-Meier's method and the log-rank test. A multivariate Cox proportional hazards regression model was used to identify independent prognostic factors. Correlations between circWDR25, miR-4474-3p, and ALOX15 expression and various clinicopathological or serological variables were analyzed using the Mann-Whitney *U* test.

2.4. Cell lines and transfection of lentiviral vectors

The human HCC cell lines SMMC-7721, hep3B (Academy of Life Sciences of Chongqing Medical University) and HCCLM3 (Liver Cancer Institute, Zhongshan Hospital) were cultured in Dulbecco's modified Eagle's medium (DMEM) supplemented with 10% foetal bovine serum and 1% penicillin/streptomycin. In some experiments, to detect the effects of ALOX15 on the expression of PD-L1 in HCC cells, HCC cells were cultured in the presence of 1 μmol/mL or 10 μmol/mL ALOX15 inhibitors (PD146176, MedChemExpress, USA) for 24 h. In some experiments, to assess the expression of CTLA-4 in HSCs, HSCs were cultured 10 ng/mL or 100 ng/mL LPS (L2880, Sigma-Aldrich) for 24 h.

A lentiviral vector for circWDR25-overexpression

(circWDR25OE) or a lentiviral vector containing shRNA-circWDR25 to knockdown circWDR25 (circWDR25KD), and miR-44474-3p mimics were synthesized (Shanghai Genechem Co. Ltd., Shanghai, China). Stable transfectants were characterized using a quantitative real-time polymerase chain reaction (qRT–PCR).

2.5. Isolation and identification of exosomes

The culture medium of HSCs was collected. Isolation of exosomes from HSCs in all experiments was performed by ultracentrifugation as described previously with minor modifications (*29*). Briefly, supernatant fractions were collected from HSC cell cultures by centrifugation at 500 g for 5 min. The supernatant was centrifuged at 2,000 g for 10 min, and then the supernatant was collected and centrifuged at 10,000 g for 30 min again. Exosomes were then centrifuged at 100,000 g for 70 min to remove shed microvesicles. The supernatant was filtered with a 0.22-μm membrane filter (Merck Millipore). Finally, the exosome pellet was resuspended in 10 ml of PBS and collected by ultracentrifugation at 100,000 g for 70 min. Then, the exosome size and particle number were analyzed and verified using a DS500 nanoparticle characterization system (NanoSight) and electron microscopy.

In some experiments, before isolation of exosomes, HSCs were transfected with circWDR25KD or circWDR25OE lentivirus or a blank vector (circWDR25NC) in order to obtain HSC exosome-derived circWDR25KD or circWDR25OE.

2.6. Microarray analysis of circRNA

Total RNA was extracted from HSC-derived exosomes for microarray analysis (untreated HSC-derived exosomes and HSC-derived exosomes cocultured with three HCC cell lines). The labelled circRNAs were hybridized onto an Arraystar Human circRNA Array V2 (8 × 15K, Arraystar) based on the manufacturer's standard protocol. circRNAs that were significantly differentially expressed in two samples were identified through fold-change filtering ≥ 2.0 and a p value of < 0.05.

2.7. In situ hybridization and fluorescence in situ hybridization (FISH) testing

TMAs were dewaxed and rehydrated. Then, 3% hydrogen peroxide was used to treat the slices for 10 minutes to inactivate endogenous enzymes. Proteinase K was applied to the slices to expose nucleic acid segments at 37°C for 30 minutes. After prehybridization at 37°C for 2 h, TMAs were hybridized with specific DIG-labelled probes at 37°C overnight. After blocking, biotinylated anti-digoxin was added to the slices for reaction at 37°C for 1 h. After washing, the slides were reacted with streptavidin-biotin complex peroxidase at 37°C for 30 minutes and stained with DAB and hematoxylin. The method for counting positive cells was the same as that for IHC. The procedures for the FISH assay were similar to those for the ISH assay except that specific FAM-labelled circWDR25 probes and Cy3-labelled miR-4474-3p probes were used and stained with DAPI. Slides were photographed under a fluorescence microscope. The probe sequences are shown in Table S1 (*http://www.biosciencetrends.com/action/getSupplementalData.php?ID=107*).

2.8. Dual-luciferase reporter gene detection assay

A luciferase reporter plasmid was generated using a Mutagenesis Kit (QIAGEN, California, USA). The targeted sequence (wild type) of ALOX15 or circWDR25 was added downstream of firefly luciferase; Renilla luciferase was used as an internal reference. The mutant reporter was also used as a control. After cotransfection with the reporter plasmid and miR-4474-3p mimics or an inhibitor or NC oligos, 293T cells were cultured in 96-well plates for 48 h. Finally, the cells were extracted, and firefly and Renilla luciferase activity was quantified with a dual-luciferase reporter assay (Promega, USA).

2.9. RNA pull-down assay

A circWDR25 probe was designed and synthesized (Shanghai Genechem Co. Ltd., Shanghai, China). Hep3B cells were harvested and lysed. M280 streptavidin Dynabeads (Invitrogen) were incubated with the circWDR25 probe to generate probe-coated beads, which were incubated with the cell lysates at 4°C overnight. Then, the RNA complexes bound to the beads were eluted and extracted with a RNeasy Mini Kit (Qiagen) for qRT-PCR analysis.

2.10. qRT-PCR

Total RNA was isolated using TRIzol Reagent (Life Technologies, Carlsbad, CA, USA) according to the manufacturer's instructions. The qRT-PCR primer sequences are provided in Table S1 (*http://www.biosciencetrends.com/action/getSupplementalData.php?ID=107*).

2.11. Western blotting

The proteins were electrophoresed using SDS-containing polyacrylamide gels, transferred onto polyvinylidene fluoride (PVDF) membranes (Millipore Corp., Billerica, MA, USA), and blocked with 5% nonfat dry milk in 0.1% Tween (TBST) buffer at room temperature for 2 h. The membranes were incubated at 4°C overnight with the appropriate primary antibody. Antibodies were detected

using HRP-conjugated secondary antibody (Abcam) for 2 h at room temperature. All of the antibodies used in this study are listed in Table S2 (*http://www.biosciencetrends.com/action/getSupplementalData.php?ID=107*).

2.12. Cell proliferation, migration, and Matrigel invasion assays

Cell proliferation was measured using the Cell Counting Kit 8 (CCK-8, Dojindo, Japan) assay as described previously (*30*). A total of 5×10^3 cells were maintained in 96-well plates. At 0, 24, 48 and 72 h after treatment, cell viability was measured.

As described previously (*13*), for transwell migration assays, HCC cells were prestarved for 24 h prior to running the assay, and HCC cells (1×10^5/well) in serum-free medium were placed in an 8-μm pore upper chamber (24-well insert, Millipore, USA). Complete medium was added to the lower chambers. For invasion assays, HCC cells (1×10^5/well) were placed in the upper chamber with a Matrigel-coated membrane (BD, USA). After 24 h of incubation, cells were fixed with methanol and stained with crystal violet.

2.13. Wound healing assay

After incubation for 24 h, HCC cells were seeded and cultured in 6-well plates (1×10^6/well) to 90% confluence. Cell monolayers were scratched with a sterile 200-μL pipette tip to form a wound. Cell migration was quantified by measuring the relative area of the wound at 0, 24 and 48 h using inversion microscopy (Olympus, Japan).

2.14. Xenograft model

Balb/c-nude mice were purchased from the National Laboratory Animal Center (6-8 weeks old, Shanghai, China). As described previously (*31,32*), six mice per group were used for xenograft experiments, and cell suspensions in 100 μL phosphate-buffered saline (PBS) containing 1×10^7 HCC cells (SMMC-7721 and Hep3B) were injected subcutaneously into the right flank. Tumor growth was monitored and measured weekly, and tumor volume was calculated. Tumor bulk was calculated according to the following formula: volume = (width^2 × length)/2. When the tumors reached a volume of approximately 100 mm^3, the mice were randomly assigned to three groups, and mice with tumors were injected weekly with 100 μL of PBS at 5 μg per dose of HSC-derived exosomes with circWDR25 knockdown or blank vector for 4 weeks. Afterward, the animals were sacrificed. All animal care and experimental protocols were performed in line with the guidelines of the Animal Ethics Committee of Chongqing Medical University.

2.15. Statistical analysis

Values are expressed as the mean ± standard deviation (SD). Student's *t* test was used for comparisons between groups. Categorical data were analyzed using a chi-squared test and Fisher's exact probability test. Correlations between circWDR25, miR-4474-3p, and ALOX15 expression and various clinicopathological or serological variables were analyzed using the Mann-Whitney *U* test. RFS and OS in patients with HCC were analyzed using Kaplan-Meier's method and the log-rank test. A multivariate Cox proportional hazards regression model was used to identify independent prognostic factors. The "minimum *p* value" approach (*33*) was used to obtain an optimal cut-off for RFS.

3. Results

3.1. CircWDR25 is highly expressed in activated HSC exosomes induced by hepatoma cells

After coculturing with HCC cells (Figure 1A), HSC-derived exosomes were successfully isolated and identified using electron microscopy, a nanoparticle characterization system, and exosomal biomarkers (Figure 1B-D). According to circRNA microarray analysis, the levels of expression of various exosomal circRNAs from activated HSCs changed (Table S3, *http://www.biosciencetrends.com/action/getSupplementalData.php?ID=108*). Among the circRNAs that changed significantly (≥ 2-fold change and $p < 0.05$), 152, 145, and 124 circRNAs were upregulated and 144, 213, and 75 circRNAs were downregulated in HSC exosomes after stimulation with SMMC-7721, Hep3B, or HCCLM3 compared to untreated HCC cells (Figure 1E). Notably, hsa_circRNA_004310 (GeneSymbol: WDR25) was the most significantly and consistently upregulated exosomal circRNA in the HSC-derived exosomes cocultured with the three HCC cell lines (Figure 1F).

3.2. High levels of peritumoral circWDR25 and α-SMA expression correlate with a poor prognosis for patients with HCC

To further investigate the clinical relevance of circWDR25 and activated HSCs in patients with HCC, in situ hybridization (Figure 2A) was used to analyze the expression of circWDR25 and α-SMA (an activated HSC marker) in a TMA consisting of 348 HCC tissues. Interestingly, the levels of circWDR25 and α-SMA expression decreased significantly in peritumoral liver tissues compared to paired intratumoral tissues from the same patient (Figure S1, *http://www.biosciencetrends.com/action/getSupplementalData.php?ID=106*), and the expression was mainly localized in the cytoplasm. Kaplan-Meier survival analysis revealed that both intratumoral circWDR25 and intratumoral α-SMA could not predict outcomes for patients with HCC. However, levels of both peritumoral circWDR25 and

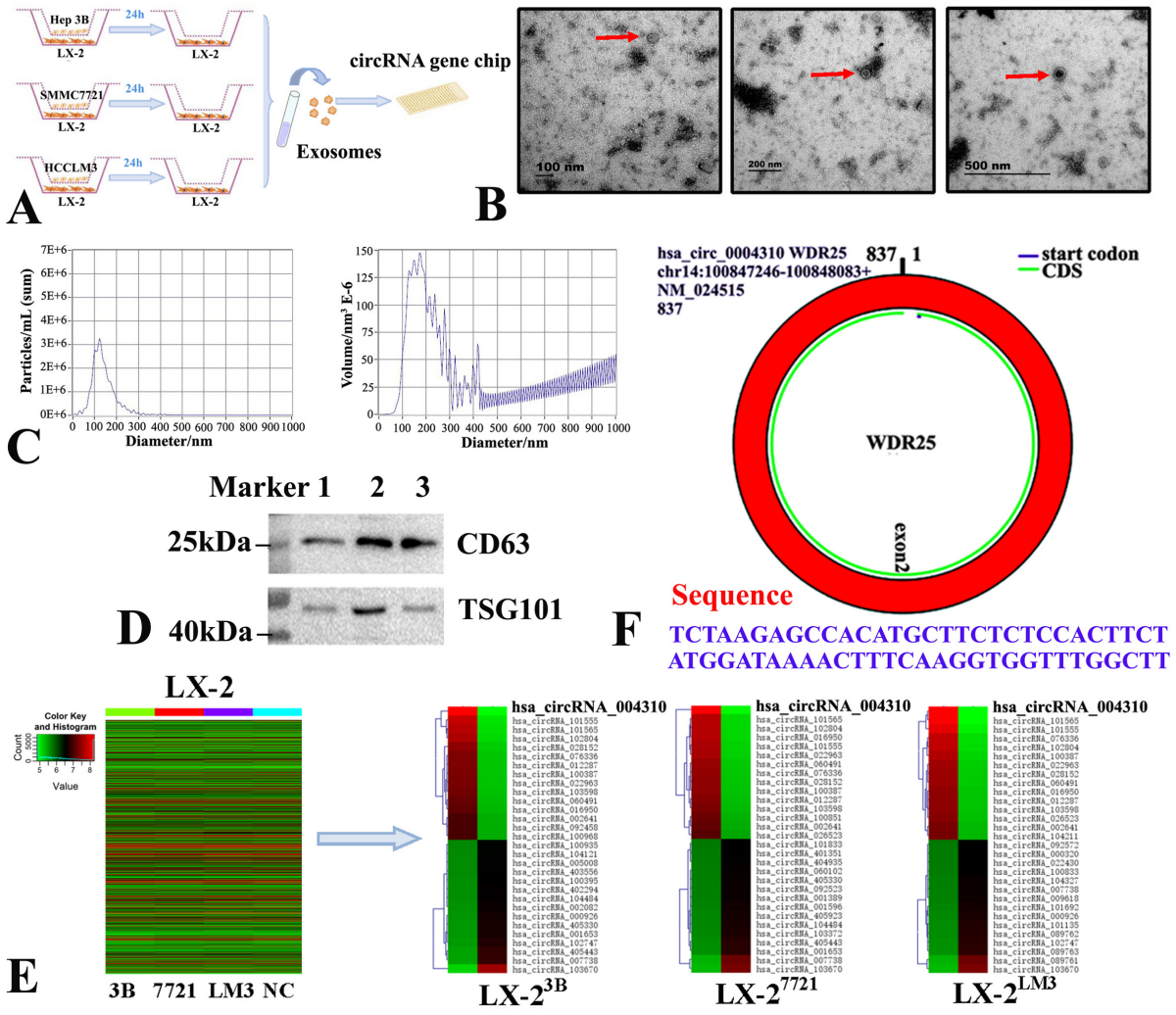

Figure 1. Identification of circWDR25 in hepatic stellated cell (HSC)-derived exosomes. A: Diagram showing the procedure to obtain HSC-derived exosomes for circRNA gene chip analyses. **B:** Transmission electron microscopy image of exosomes from HSCs indicated with red arrows. **C:** Nanoparticle tracking analysis of HSC-derived exosomes, confirming that more than 95% of the detected particles ranged in size from 30-200 nm in diameter. **D:** Exosome markers (CD63 and TSG101) in HSC-derived exosomes detected with Western blot analysis. **E:** Each panel of 2 separate LX-2 exosomes per group (LX-2 *vs*. LX-2 cocultured with the three HCC cell lines, respectively) displayed hierarchical clustering based on differential expression of circRNA genes represented as a heat map. **F:** Diagram of the genomic location of circWDR25 and the circularization of WDR25 exon 2 forming circWDR25.

peritumoral α-SMA expression were associated with OS and RFS. Patients with high levels of expression of both peritumoral circWDR25 and peritumoral α-SMA had a poorer prognosis (Figure 2B). Multivariate analysis indicated that both circWDR25 and α-SMA were independent predictors for OS and RFS in patients with HCC (Table S4, *http://www.biosciencetrends.com/action/getSupplementalData.php?ID=107*). Together, these results corroborated the circRNA microarray data, which revealed increased exosomal circWDR25 expression in tumor-activated HSCs. Moreover, these data indicated that elevated circWDR25 expression in HSC-derived exosomes may contribute to the progression of HCC.

Furthermore, a high level of expression of peritumoral circWDR25 was only significantly correlated with total bilirubin ($p = 0.038$). Patients with HCC and α-SMA overexpression had larger tumors ($p = 0.030$, Table S5, *http://www.biosciencetrends.com/action/getSupplementalData.php?ID=107*). The level of expression of peritumoral circWDR25 was positively correlated with that of peritumoral α-SMA ($r = 0.212$, $p < 0.001$; Figure 2C).

3.3. HSC exosome-derived circWDR25 promotes HCC tumor growth *in vivo* and *in vitro*

To investigate the biological functions of HSC exosome-derived circWDR25 in HCC, a lentiviral vector for circWDR25OE or a lentiviral vector containing circWDR25KD was successfully constructed to transfect HSCs (Figure 2D), and a xenograft mouse model was created (Figure 2E-F). The two HCC cell-induced tumors indicated that tumors implanted with HSC-derived exosomes had a larger tumor burden and grew faster than

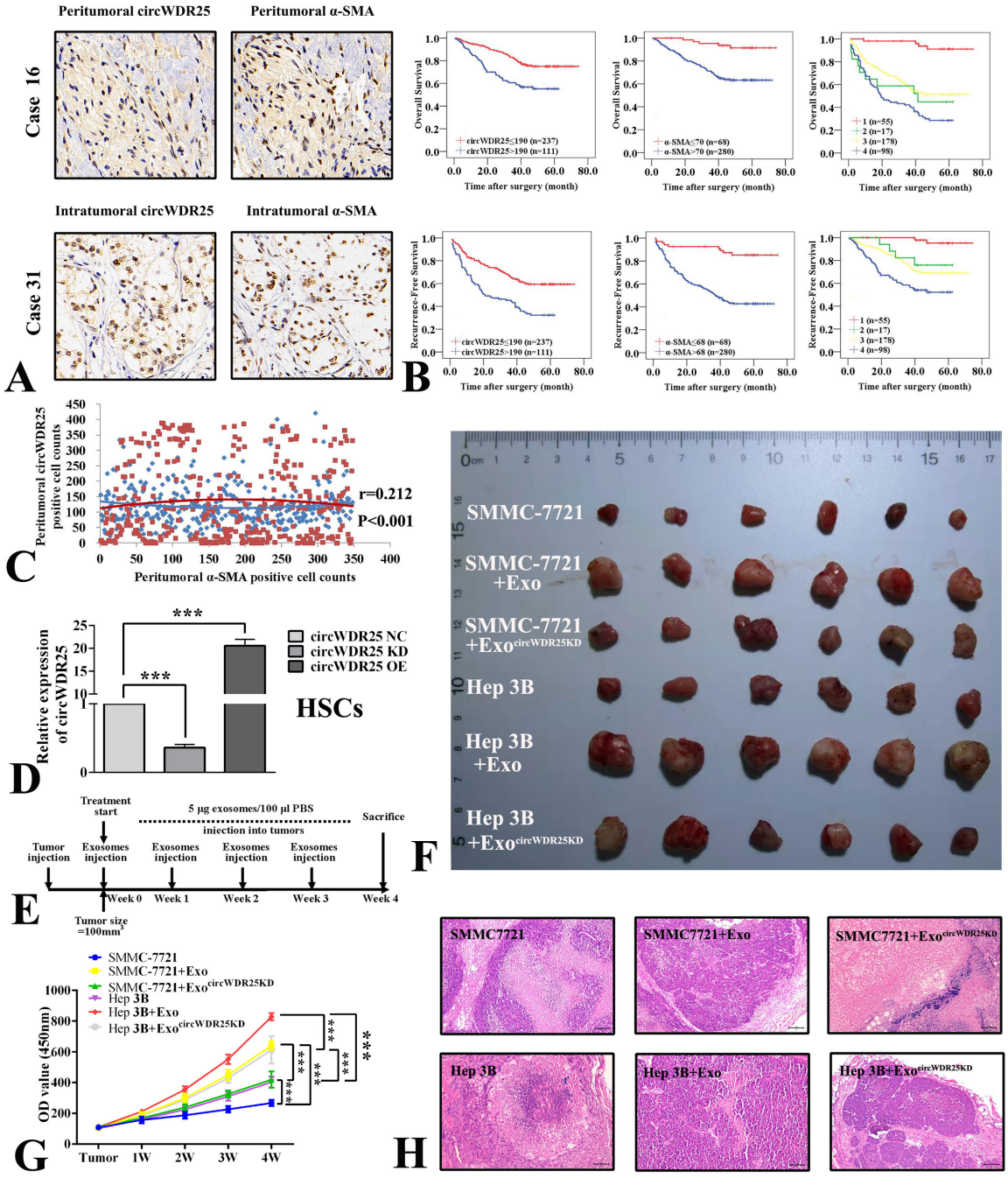

Figure 2. The expression and characterization of circWDR25 in HCC tissues from patients and xenograft mice. A: Consecutive sections were used to detect the expression of circWDR25 and α-SMA via in situ hybridization in 348 pairs of peritumoral and matched intratumoral HCC tissues (400× magnification). **B:** Peritumoral circWDR25, α-SMA, and a combination of the two were related to overall survival (OS) and recurrence-free survival (RFS) of patients with HCC after curative resection. **C:** The scatter diagram indicated that the expression of peritumoral circWDR25 is positively related to that of peritumoral α-SMA. **D:** A lentiviral vector for circWDR25OE or circWDR25KD was successfully constructed to transfect HSCs. **E:** Diagram of the procedure to establish a xenograft mouse model affected by HSC-derived exosomal circWDR25. **F:** Representative images of subcutaneous xenograft tumors treated or not treated with HSC-derived exosomal circWDR25 ($n = 6$ for each group). **G:** Growth curves for tumor volume, which was measured every week after injection of HSC-derived exosomes into the tumors. **H:** Representative H.E staining images of mouse tumors (100× magnification). All data are expressed as the mean ± SD of three independent experiments, $^{***}p < 0.001$.

those injected with circWDR25KD transported by HSC-derived exosomes or a blank vector without exosomes (Figure 2G-H).

In *in vitro* experiments, exosomes were isolated from HSCs with circWDR25OE or circWDR25KD or with a blank lentiviral vector (circWDR25NC). After coculturing with HSC-derived exosomes, the efficiency and specificity of circWDR25 overexpression and knockdown in HCC cells (SMMC-7721 and Hep3B) were verified using qRT–PCR (Figure 3A). Subsequent CCK-8 assays, transwell assays, and wound healing assays were performed to assess proliferation,

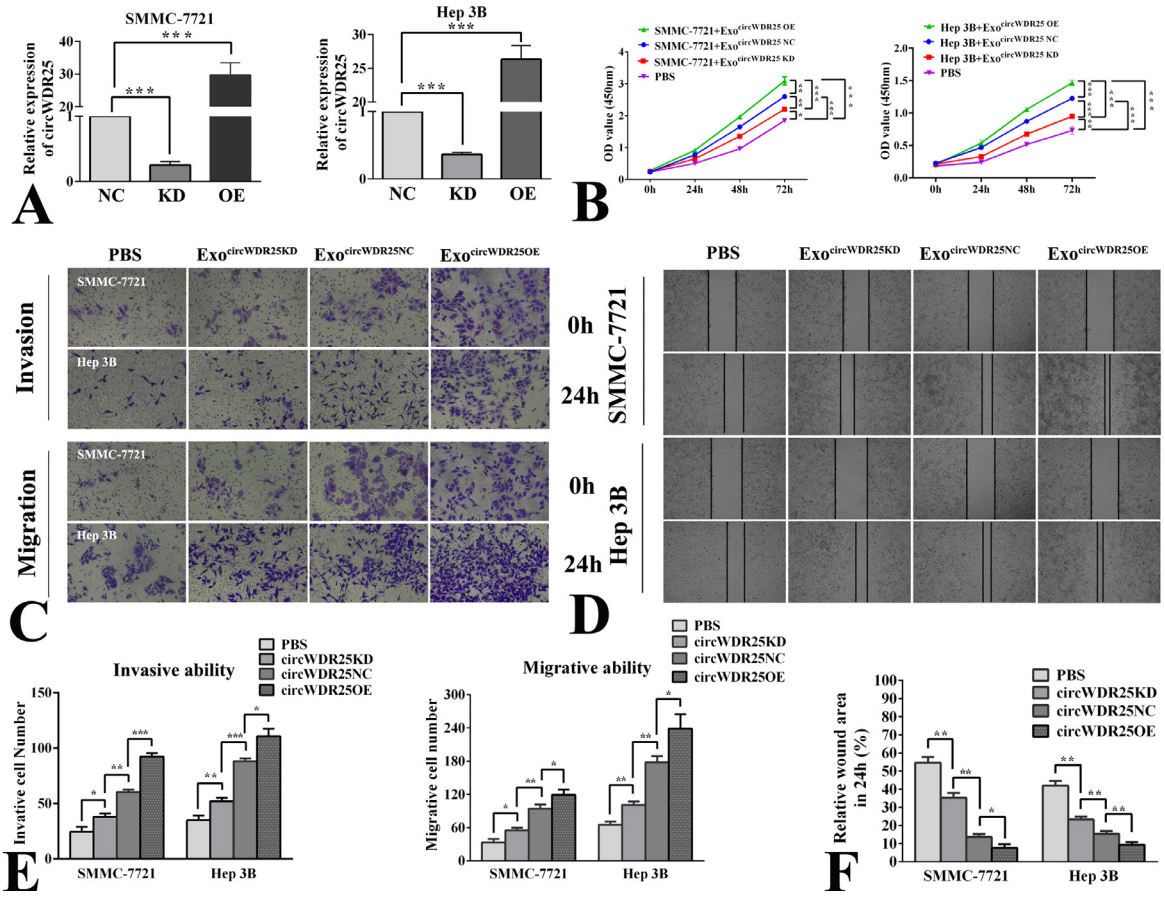

Figure 3. HSC exosome-derived circWDR25 promotes proliferation, migration, and invasion by HCC cells *in vitro*. A: Relative circWDR25 expression in HCC cell lines was determined with qRT-PCR after coculturing with HSC exosome-derived circWDR25KD, circWDR25OE, or circWDR25NC. **B:** The growth curves for HCC cells were assessed using CCK-8 assays after coculturing with HSC exosome-derived circWDR25KD, circWDR25OE, or circWDR25NC. **C:** Transwell assays were performed to evaluate migration and invasion by HCC cells. **D:** A wound healing assay wase performed to assess cell migration. **E:** Numbers of invading and migrating cells according to a transwell assay. **F:** Relative wound area based on the wound healing assay. All data are expressed as the mean ± SD of three independent experiments. $^{*}p < 0.05$, $^{**}p < 0.01$, $^{***}p < 0.001$.

migration, and invasion by HCC cells as were affected by HSC-derived exosomes (Figure 3B-D). The CCK-8 assay indicated that HSC-derived exosomes with circWDR25OE markedly increased the proliferation of HCC cells, while HSC-derived exosomes with circWDR25KD inhibited cell growth compared to the NC and PBS groups (Figure 3B). The results of the transwell and wound healing assays demonstrated that HSC-derived exosomes with high circWDR25 levels dramatically enhanced invasion by HCC cells compared to exosomes with low circWDR25 levels (Figure 3E-F). Collectively, these findings indicate that circWDR25 derived from HSC exosomes plays an oncogenic role in HCC cells.

3.4. CircWDR25 acts as a sponge for miR-4474-3p

Based on a cross-analysis of microRNA target prediction databases (TargetScan and miRanda), 298 miRNAs with potential binding sites for circWDR25 were identified (Table S6, *http://www.biosciencetrends.com/action/getSupplementalData.php?ID=109*). For instance, miR-4474-3p, miR-6856-5p, miR-889-5p, miR-210-5p, and miR-6763-5p were the most likely potential binding sites for circWDR25 (Figure 4A). Of note, circWDR25 had four binding sites with miR4474-3p (Figure 4B), and miR4474-3p was the most highly enriched miRNA in sponge complexes with circWDR25, a finding that was confirmed by pull-down assays with a biotin-labelled circWDR25 probe. In addition, FISH analysis of HEK293T cells indicated that circWDR25 was colocalized with miR-4474-3p in the cytoplasm (Figure 4C). Moreover, after a pull-down assay was performed with a biotinylated miR-4474-3p mimic, qRT-PCR revealed significant enrichment of circWDR25 compared to negative controls. Moreover, miR-4474-3p was the most highly enriched miRNA in the sponge complexes for hepatoma cells (Figure 4D). To further verify the specific binding region between circWDR25 and miR-4474-3p, a dual-luciferase reporter assay was performed in HEK293T cells. After cotransfecting HEK293T cells with miR-4474-3p mimics and a circWDR25-WT reporter gene, a miR-4474-3p mimic significantly reduced the luciferase activity of the circWDR25-WT

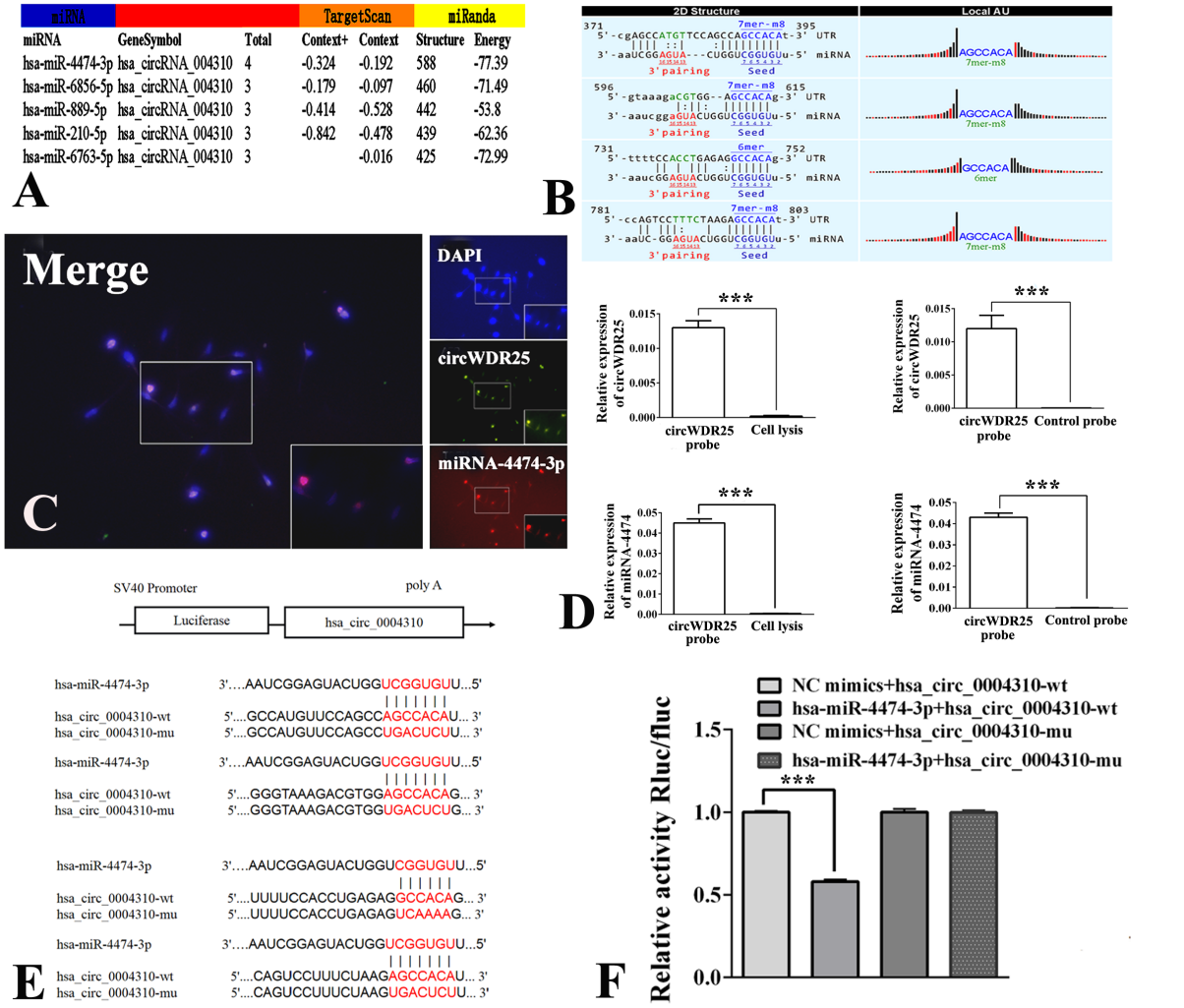

Figure 4. CircWDR25 functions as a sponge for miR-4474-3p. A: The top five target miRNAs with potential binding sites for circWDR25 as predicted by TargetScan and miRanda. **B:** The putative binding sites of miR-4474-3p in circWDR25. **C:** The colocalization of circWDR25 and miR-4474-3p in HEK293T cells was determined using a FISH assay. **D:** After a pull-down assay was performed with a biotinylated miR-4474-3p mimic, qRT–PCR indicated significant enrichment of circWDR25 compared to negative controls. **E-F:** The luciferase activity of the circWDR25 dual-luciferase reporter vector (WT or MUT) in HEK293T cells cotransfected with miR-4474-3p. All data are expressed as the mean ± SD of three independent experiments. $^{***}p < 0.001$.

reporter but not the mutant circWDR25 reporter (Figure 4E-F). Thus, circWDR25 acts as a sponge of miR-4474-3p and suppresses its expression.

3.5. MiR-4474-3p reverses the oncogenic effects of circWDR25 in HCC cells

MiR-4474-3p mimics were successfully transfected into HCC cells (Figure S2A, *http://www.biosciencetrends.com/action/getSupplementalData.php?ID=106*). The levels of miR-4474-3p expression in the two HCC cell lines decreased or increased after transfection with lentivirus carrying circWDR25OE or circWDR25KD, respectively (Figure S2B, *http://www.biosciencetrends.com/action/getSupplementalData.php?ID=106*). After transfecting miR-4474-3p mimics in HCC cells (Figures S2C and S3A, *http://www.biosciencetrends.com/action/getSupplementalData.php?ID=106*), CCK-8 assays, transwell assays, and wound healing assays indicated that cell proliferation, invasion, and migration decreased significantly (Figures 5A-B and S3A-D, *http://www.biosciencetrends.com/action/getSupplementalData.php?ID=106*). To further elucidate the functions of miR-4474-3p in circWDR25-induced signalling, rescue experiments were performed with cotransfection of miR-4474-3p mimics or miR-4474-3pNC with circWDR25OE or circWDR25NC. Promotion of the migration and invasion by HCC cells induced by circWDR25OE was reversed by miR-4474-3p mimics in transwell assays (Figures 5B and S3D, *http://www.biosciencetrends.com/action/getSupplementalData.php?ID=106*). These results suggest that miR-4474-3p has an anti-oncogenic effect on HCC cells and that it has an important function downstream of circWDR25.

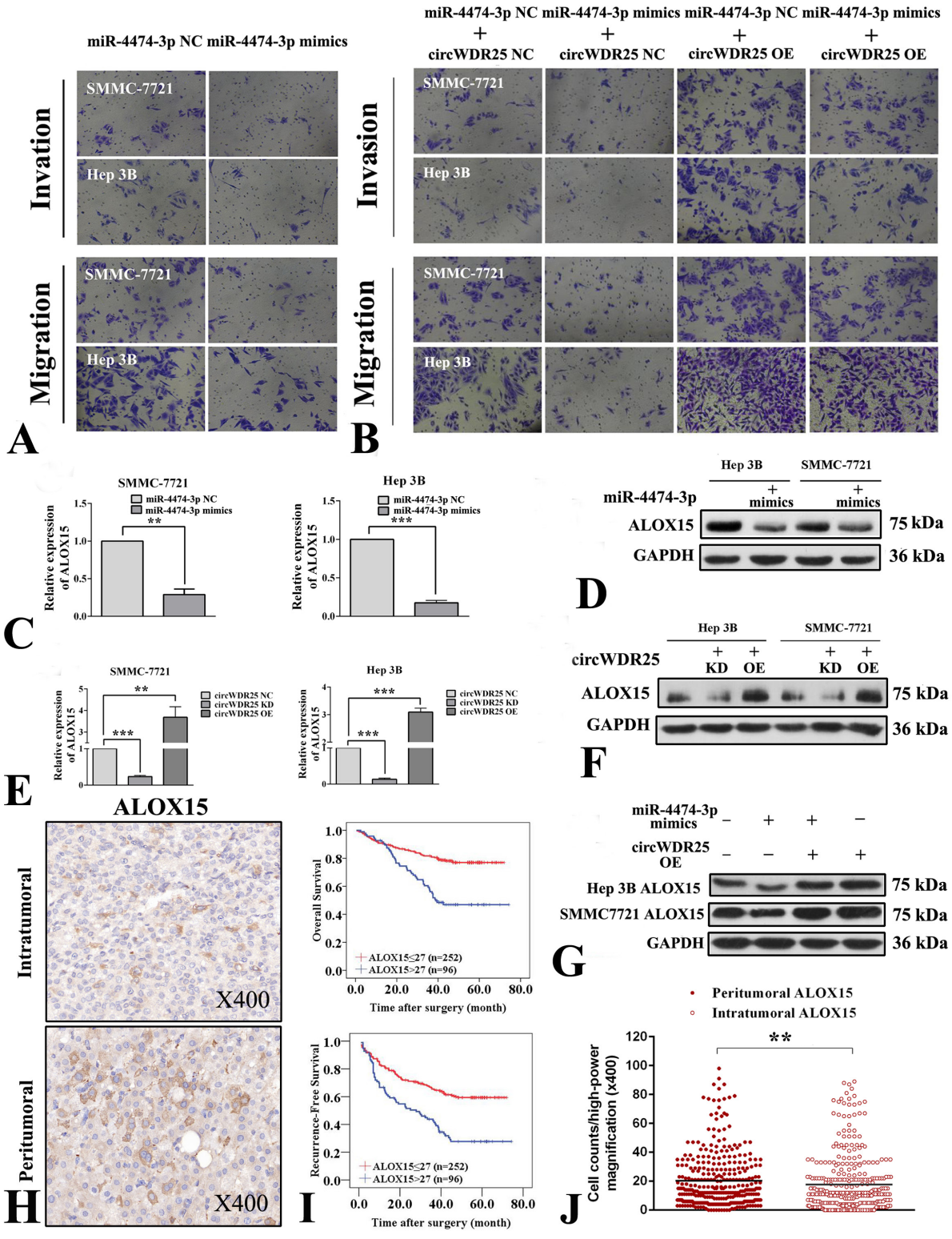

Figure 5. MiR-4474-3p reverses the oncogenic effects of circWDR25, which indirectly regulates ALOX15. A: Invasion and migration by HCC cells as were affected by the miR-4474-3p mimics were analyzed using a transwell assay. **B:** Transwell assays indicated that miR-4474-3p reversed the oncogenic effects of circWDR25 in four groups of HCC cells. **C-D:** qRT-PCR and western blot analyses of the relative levels of ALOX15 expression in HCC cells after transfection with the miR-432-5p mimics. **E-F:** The relative levels of ALOX15 mRNA and protein in HCC cells after transfection with the circWDR25KD or circWDR25OE. **G:** Western blot analyses of the relative levels of ALOX15 expression in HCC cells after transfection with the miR-432-5p mimics or/and circWDR25OE. **H:** IHC staining of intratumoral and peritumoral ALOX15 in patients with HCC (400× magnification). **I:** Kaplan-Meier survival curves showing the OS and RFS for peritumoral ALOX15 expression based on a tissue microarray including 348 patients with HCC. **J:** The scatter diagram showed that there were higher levels of ALOX15 expression in peritumoral liver tissues than in paired intratumoral tissues. All data are expressed as the mean ± SD of three independent experiments. $^{**}p < 0.01$, $^{***}p < 0.001$.

3.6. ALOX-15 is a downstream target of miR-4474-3p and is indirectly regulated by circWDR25

To further investigate the potential gene targets of miR-4474-3p and their underlying mechanism in HCC, the online programs TargetScan and miRDB were used to perform a bioinformatic analysis. According to the two databases, 435 and 3,851 predicted genes were possibly targeted by miR-4474-3p (Tables S7 and S8, *http://www.biosciencetrends.com/action/getSupplementalData.php?ID=107; http://www.biosciencetrends.com/action/getSupplementalData.php?ID=110*). Both of these databases indicated that ALOX15 had the highest prediction score and could be a downstream target of miR-4474-3p. The dual-luciferase reporter assay also demonstrated that a miR-4474-3p mimic significantly reduced the luciferase activity of the ALOX15 3′-UTR WT reporter but not the mutant ALOX15 3′-UTR reporter (Figure S4A-B, *http://www.biosciencetrends.com/action/getSupplementalData.php?ID=106*). Moreover, qRT–PCR and a Western blot analysis suggested that miR-4474-3p mimics negatively regulated the expression of ALOX15 in both cell lines (Figures 5C-D and S4C, *http://www.biosciencetrends.com/action/getSupplementalData.php?ID=106*). In addition, the levels of mRNA and protein expression for ALOX15 were positively regulated by circWDR25 (Figures 5E-F and S4D, *http://www.biosciencetrends.com/action/getSupplementalData.php?ID=106*). The effect of circWDR25OE was fully rescued by miR-4474-5p mimics (Figures 5G and S4E, *http://www.biosciencetrends.com/action/getSupplementalData.php?ID=106*). These results identified ALOX-15 as a downstream target of miR-4474-3p that was potentially indirectly regulated by circWDR25. Elucidation of the regulatory mechanism involved in this signal pathway depends partially on further investigation of the interaction between miR-4474-3p and ALOX15.

3.7. ALOX15 is associated with the prognosis for HCC

Clinically, since the current results indicated that circWDR25 acts as a predictor of the outcomes of HCC and to regulate the levels of ALOX15 expression, whether ALOX15 was associated with HCC progression was also assessed (Figure 5H-I). Inconsistent with the expression of circWDR25, the levels of ALOX15 expression were higher in peritumoral liver tissues than in paired intratumoral tissues (Figure 5H and 5J). However, similar to peritumoral circWDR25, both univariate analysis and multivariate analysis revealed that peritumoral ALOX15 could predict the OS and RFS for patients with HCC (Figure 5I). There was no correlation between ALOX15 and characteristics of patients with HCC (Table S9, *http://www.biosciencetrends.com/action/getSupplementalData.php?ID=107*). Together, the aforementioned results verify that the circWDR25-miR4474-3p-ALOX15 axis may contribute to the tumorigenesis and progression of HCC.

3.8. Exogenous and HSC exosome-derived circWDR25 induces an EMT

A previous study by the current authors found that activated HSC secretions facilitated the aggressiveness of HCC *via* an EMT (*13*). Here, whether the expression of EMT markers was regulated by the circWDR25-miR4474-3p pathway *in vitro* was further investigated. Exogenous circWDR25KD or miR-4474-3p mimics were found to increase the expression of E-cadherin but decrease the expression of vimentin in both HCC cell lines. CircWDR25OE was completely rescued by miR-4474-5p mimics (Figures 6C and S5E-F, *http://www.biosciencetrends.com/action/getSupplementalData.php?ID=106*). In addition, the EMT induced by HSC exosome-derived circWDR25 was examined in HCC cells. Similarly, *in vitro* HSC exosome-derived circWDR25KD or circWDR25OE had the same effects on the EMT pathways in both cell lines and positively regulated the level of expression of the downstream gene ALOX15 (Figures 6D and S5G-J, *http://www.biosciencetrends.com/action/getSupplementalData.php?ID=106*). *in vivo* xenograft mouse experiments indicated that exosomal circWDR25KD from HSCs promoted EMT in tumors induced by the two HCC cell lines, which downregulated the expression of E-cadherin, increased the expression of N-cadherin and vimentin, and upregulated ALOX15 expression (Figures 6E and S5K-N, *http://www.biosciencetrends.com/action/getSupplementalData.php?ID=106*). IHC staining for EMT markers in the subcutaneous tumor yielded the same results as Western blotting *in vivo* (Figures 6F and S5O, *http://www.biosciencetrends.com/action/getSupplementalData.php?ID=106*) and further confirmed the critical effects of exosomal circWDR25KD from HSCs on the EMT pathway.

3.9. CircWDR25 and ALOX15 synergistically regulate the expression of PD-L1 in hepatoma cells and CTLA-4 in HSCs

A previous study indicated that ALOX15 was upregulated in tumor-associated macrophages (TAMs) and that it promoted CTLA-4 expression in T lymphocytes (*34*). Moreover, the PD-L1 pathway that was involved in inducing tolerance was regulated by ALOX15 (*35*). Here, the ALOX-15 inhibitor PD146176 exhibited a dose-independent inhibitory effect on the expression of PD-L1 protein in HCC cells and it extenuated the influence of circWDR25OE transported by HSC exosomes (Figure 7A-C). After stimulation with LPS and coculturing with HSC-derived exosomal circWDR25OE, there was a significant increase in CTLA-4 expression in activated HSCs (Figure 7 D-F).

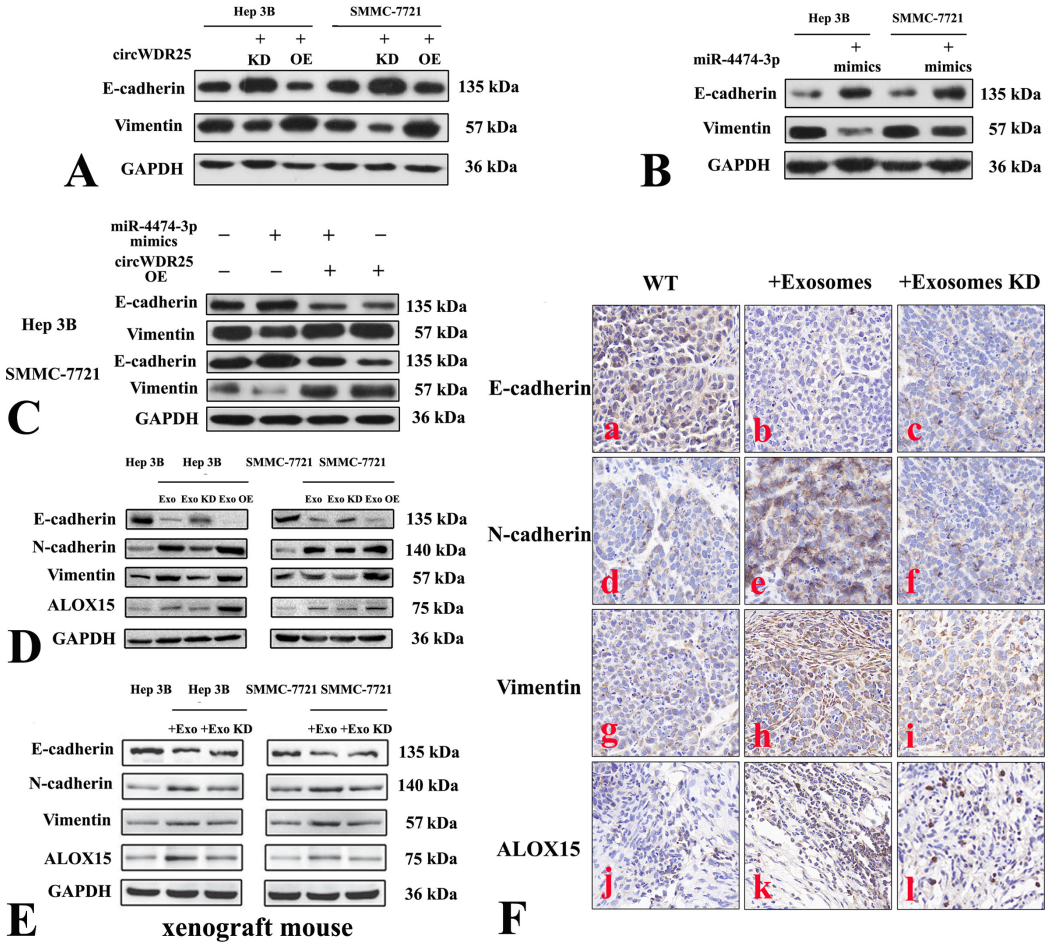

Figure 6. Exogenous and HSC exosome-derived circWDR25 induce epithelial-to-mesenchymal transition (EMT). A-B: The levels of expression of EMT marker proteins in HCC cells as were affected by circWDR25KD, circWDR25OE, or miR-4474-3p mimics were determined using Western blot analysis. **C:** The relative expression of EMT marker proteins in HCC cells as was affected by circWDR25KD, miR-4474-3p mimics, or a combination of the two. **D:** The levels of expression of EMT marker and ALOX15 proteins in HCC cells cultured with HSC-derived exosome circWDR25KD or circWDR25OE. **E:** The levels of expression of EMT marker and ALOX15 proteins in tumors of xenograft mice injected with HSC-derived exosomal circWDR25KD. **F:** Representative images of IHC staining of mouse tumors revealed the effects of exosomal circWDR25KD from HSCs on the EMT markers and ALOX15 (400× magnification).

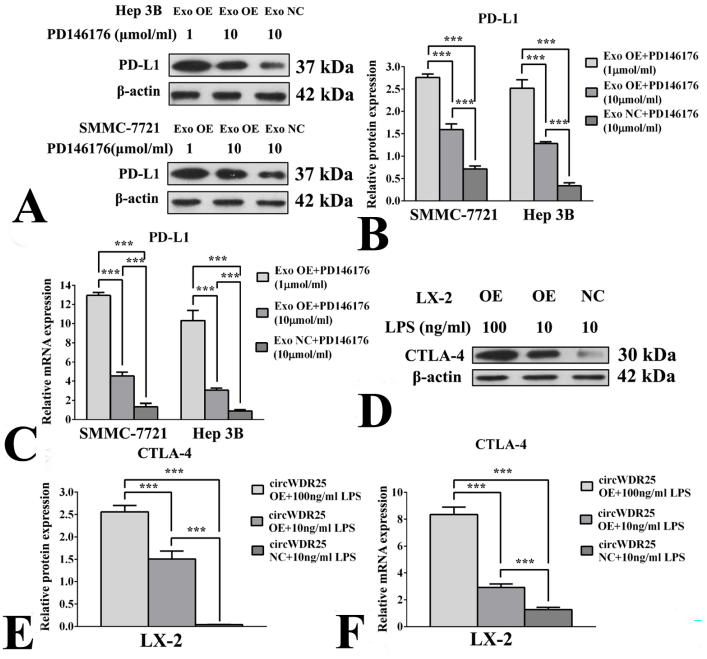

Figure 7. ALOX15 regulates the expression of PD-L1 in HCC cells and CTLA-4 in HSCs. A-B: Western blot analyses of the relative levels of expression of PD-L1 protein in HCC cells after treatment with exosome-derived circWDR25OE or circWDR25NC and different doses of the ALOX-15 inhibitor PD146176. **C:** qRT-PCR analyses of the relative levels of PD-L1 mRNA expression in HCC cells with the same treatments. **D-E:** Western blot analyses of the relative levels of expression of CTLA-4 protein in HSCs after stimulation with circWDR25OE or circWDR25NC and different doses of LPS. **F:** qRT-PCR analyses of the relative levels of CTLA-1 mRNA expression in HSCs with the same treatments. All data are expressed as the mean ± SD of three independent experiments. $^{***}p < 0.001$.

These data indicated that circWDR25 and ALOX-15 played potential synergistic roles in the immune response of the HCC microenvironment and that they might be therapeutic targets. Moreover, a daunting challenge would be to examine the immunotherapy effect of related drugs on HCC *via* this pathway.

4. Discussion

Emerging evidence indicates that in the tumor milieu of HCC, activated HSCs may accelerate the neoplastic transformation of hepatocytes after interactions with hepatocytes. The current study used RNA sequencing to profile circRNA expression in HSCs (LX-2) after stimulation with 3 different HCC cell lines (Hep3B, SMMC-7721, and HCCLM3), resulting in the identification of differentially expressed circRNAs. This study is the first to identify the circRNA hsa_circ_004310, designated circWDR25, as a significantly upregulated circRNA in tumor-activated HSCs and HCC tissues. Moreover, results indicated that HSC-secreted exosomal circWDR25 was delivered to HCC cells, it upregulated ALOX15 expression by sponging miR-4474-3p, and it in turn induced EMT. Moreover, loss- and gain-of-function experiments revealed that HSC-derived exosomal circWDR25 enhanced the proliferation and aggressiveness of HCC cells and facilitated the transmission of tumor information. The oncogenic role of circWDR25 was also corroborated by its potential prognostic value in patients with HCC. More importantly, results indicated that circWDR25-overexpressing HSCs and exosomal circWDR25-stimulating HCC cells were characterized by increased expression of CTLA-4 and PD-L1, respectively. All of the above results suggest that exosomal circWDR25 may provide a potential immunotherapy-related antitumor target for patients with HCC.

The current results indicated that circWDR25 was a critical signal transducer in the cellular network of the tumor microenvironment when preferentially exposed to cancer cells *via* the transport of HSC-derived exosomes. Many studies have confirmed that HCC development and progression are greatly influenced by dozens of circRNAs, which are enriched and stable in exosomes and can act in cellular networks. However, few studies have reported the role of HSC-derived exosomes in HCC. Most recently, Xia *et al*. (*24*) confirmed that HCC cell-derived exosomal smoothing promoted HCC progression after activating HSCs *via* the hedgehog pathway. Another recent study revealed that exosomes derived from HSCs stimulated cytokine synthesis-release and cell migration of macrophages and subsequently modulated the inflammatory response and fibrosis (*36*). The current study indicated that both HSC exosomal circWDR25 and also endogenous circWDR25 enhanced the proliferation of and invasion by HCC cells. Hence, circWDR25 acts as a bridging cytokine between HSC-to-HCC cell communications. In addition, these studies suggested its functional properties and triggering of hepatocarcinogenesis during the development of HCC.

Cytoplasmic exon circRNAs primarily function through miRNA sponging. Multiple-sequence alignment analyses have already revealed that miR-4474-3p is a microRNA target site of some exon and intron enhancers and silencers and transcription factors, some of which are cancer related (*37*). Cross-analysis of miRanda and TargetScan in the current study revealed that 4 miRNAs harbored potential binding sites for circWDR25. Of note, miR4474-3p was the most highly enriched miRNA in the sponge complexes with circWDR25, which was confirmed by pull-down assays with a circWDR25 probe. Dual-luciferase assays also verified the binding between circWDR25 and miR-4474-3p. The above results indicated that circWDR25 could directly bind to the seed region of miR-4474-3p in the cytoplasm of HCC cells. A rescue experiment to elucidate the biological function of this complex indicated that the circWDR25OE-induced enhancement of tumor proliferation and migration was reversed by treatment with miR-4474-3p mimics. Therefore, this study has demonstrated that circWDR25 functions as a miR-4474-3p sponge and that it has an effect on the proliferation of and invasion by HCC, and especially *via* transportation of HSC-derived exosomes.

As a target of miR-4474-3p, ALOX15 is upregulated in HCC cells and peritumoral tissues. Notably, ALOX15, an enzyme for lipid metabolism, has been widely reported to play important roles in a variety of human diseases, and especially oxidative stress, immune/inflammatory responses, and cancer (*38*). In HCC, Ma *et al*. found that ALOX15 prevented cancer cell apoptosis and promoted cancer cell growth and metastasis *via* the interaction of the Akt/heat shock protein (HSP)-90 pathway (*39*). The current study also indicated that circWDR25 promoted HCC progression *via* the circWDR25/miR-4474-3p/ALOX15 axis. Another important finding was that peritumoral ALOX15 serves as an unfavorable prognostic predictor in HCC. Given its involvement in inflammatory responses and the roles of the peritumoral inflammatory environment as the principal target of intrahepatic metastasis (*14,16*), ALOX15 may facilitate intrahepatic metastases, probably through the conversion of the proinflammatory response to tumor development.

Recently, EMT programs, a process involving a loss of epithelial cell polarity, extracellular matrix remodelling, and premetastatic niche formation, have garnered attention again due to emerging concepts and evidence related to cancer heterogeneity and metastasis (*40*). Oncogenic exosomal miRNAs (*e.g.*, miR-23a, miR-193a-3p, miR-210-3p, and miR-5100 (*41*)) and circRNAs (*e.g.*, circ-0004277 (*42*)) are also involved in the regulation of EMT. Similarly, the current findings suggest that HSC exosomal circWDR25 induces EMT in HCC *via* the miR4474-3p-ALOX15 axis. *In*

vitro experiments also verified that HSC exosomal and endogenous circWDR25 promoted migration and invasion by HCC cells. Taken together, these results provide evidence that circWDR25 can indirectly (HSC-derived exosomes) or directly (endogenously) enhance the progression of HCC metastasis *via* the EMT process.

Currently, the combination of immune checkpoint inhibitors (ICIs), such as PD-1 and CTLA-4, has efficacious synergistic antitumor activity and therefore has emerged as an anticancer strategy in HCC associated with high levels of their expression in tumor cells and immune cells, inducing T cell inhibition and tumor immune escape (*43*) . Interestingly, the current findings indicated that circWDR25 and ALOX15 can synergistically regulate the levels of CTLA-4 expression in HSCs or PD-L1 in HCC cells, possibly suggesting that the circWDR25-ALOX-15 signalling pathway is involved in immunomodulatory activity between activated HSCs and HCC cells. To date, tumor mutational burden (TMB) and PD-L1 expression are the most extensively studied predictive biomarkers of immunotherapy efficacy. The results for circWDR25 and ALOX15 in the current study indicated that they synergistically provoked the activation of the PD-L1 and CTLA-4 pathways and may have distinct but complementary effects in negatively regulating immune activity and as predictive biomarkers of the efficacy of immunotherapy. However, further studies need to explore the in-depth mechanisms.

The current study had several limitations. (*i*). Given the role of circWDR25 as an upstream gene in this signalling pathway, its regulatory mechanism involved miR-4474-3p-ALOX15. A regulatory relationship between miR-4474-3p and ALOX15 was identified, but the specific regulatory mechanism of miR-4474-3p on ALOX15 should be explored in the future. (*ii*) Further studies need to validate the immunotherapy efficacy of related drugs *via* this pathway, taking into consideration the complexity of signalling networks, the target drug combined with PD-1 or CTLA-4, medication dosage and duration of administration, and even the possibility of clinical trials. (*iii*) If gene knockout mice were available, more accurate and detailed evidence regarding drug treatment and the malignant capacity for invasion and metastasis induced by these oncogenes could be obtained.

In conclusion, circWDR25 was identified as a novel circRNA that is involved in the progression of HCC. To the extent known, few studies have examined the mechanism of exosomal circRNAs from HSCs in HCC.

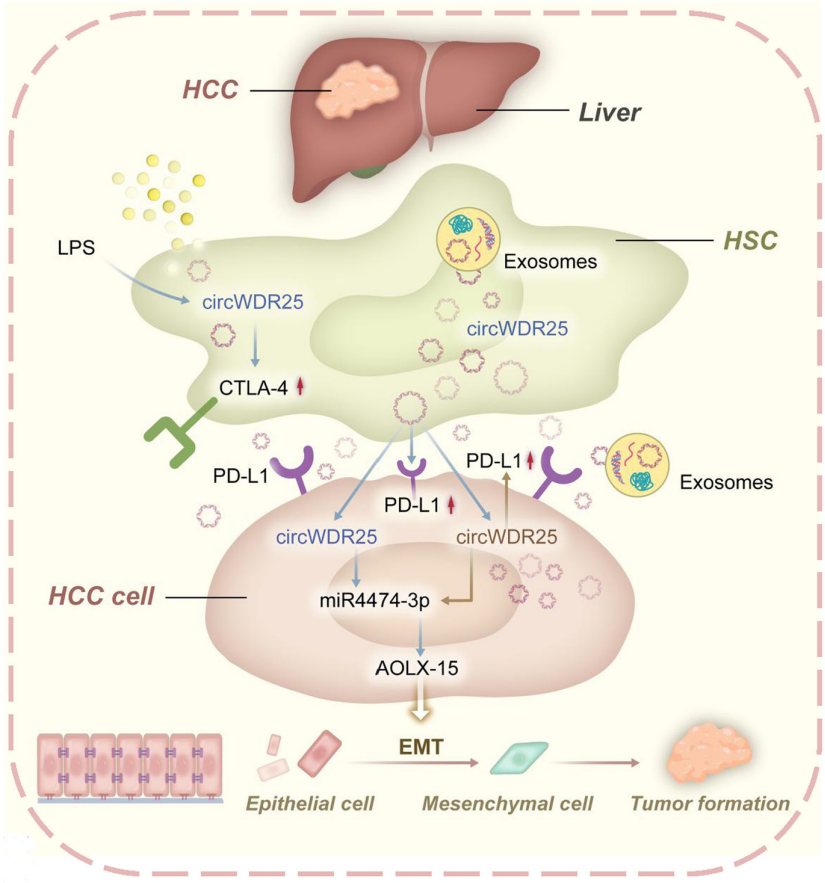

Figure 8. Diagram of the mechanistic findings. Exogenous and HSC exosome-derived circWDR25 promotes HCC cell proliferation, migration, and invasion through the circWDR25/miR-4474-3p/ALOX15 and epithelial-to-mesenchymal transition (EMT) axes. In addition, circWDR25 also increased the expression of PD-L1 in HCC and CTLA-4 in HSCs.

A valuable contribution of this study is the identification of the important role of HSC-derived exosomal circRNA (circWDR25) in cell-to-cell communications, which may be responsible for tumor aggressiveness *via* the downstream miR4474-3p/ALOX15 regulatory loop and EMT pathway in HCC. Importantly, both circWDR25 and ALOX15 were able to predict the outcomes of HCC and stimulate the expression of CTLA-4 and PD-L1 (Figure 8). In this regard, both may be promising predictive biomarkers of the prognosis for HCC and the efficacy of immunotherapy.

Funding: This work was supported by a grant from the National Natural Science Foundation of China (No. 82170666) and a Science and Health Joint Research Project of Chongqing City (2020GDRC013); CQMU Program for Youth Innovation in Future Medicine (W0087).

Conflict of Interest: The authors have no conflicts of interest to disclose.

References

1. Forner A, Reig M, Bruix J. Hepatocellular carcinoma. Lancet. 2018; 391:1301-1314.
2. Wen N, Cai Y, Li F, Ye H, Tang W, Song P, Cheng N. The clinical management of hepatocellular carcinoma worldwide: A concise review and comparison of current guidelines: 2022 update. Biosci Trends. 2022; 16:20-30.
3. Deng ZJ, Li L, Teng YX, Zhang YQ, Zhang YX, Liu HT, Huang JL, Liu ZX, Ma L, Zhong JH. Treatments of hepatocellular carcinoma with portal vein tumor thrombus: Current status and controversy. J Clin Transl Hepatol. 2022; 10:147-158.
4. Villanueva A. Hepatocellular Carcinoma. N Engl J Med. 2019; 380:1450-1462.
5. Yang JD, Hainaut P, Gores GJ, Amadou A, Plymoth A, Roberts LR. A global view of hepatocellular carcinoma: Trends, risk, prevention and management. Nat Rev Gastroenterol Hepatol. 2019; 16:589-604.
6. Qiu G, Xie K, Jin Z, Jiang C, Liu H, Wan H, Huang J. The multidisciplinary management of hepatocellular carcinoma with portal vein tumor thrombus. Biosci Trends. 2021; 15:148-154.
7. Tsuchida T, Friedman SL. Mechanisms of hepatic stellate cell activation. Nat Rev Gastroenterol Hepatol. 2017; 14:397-411.
8. Myojin Y, Hikita H, Sugiyama M, *et al*. Hepatic stellate cells in hepatocellular carcinoma promote tumor growth *via* growth differentiation factor 15 production. Gastroenterology. 2021; 160:1741-1754 e1716.
9. Xiao H, Zhang Y, Li Z, Liu B, Cui D, Liu F, Chen D, Liu Y, Ouyang G. Periostin deficiency reduces diethylnitrosamine-induced liver cancer in mice by decreasing hepatic stellate cell activation and cancer cell proliferation. J Pathol. 2021; 255:212-223.
10. Liu C, Zhou X, Long Q, Zeng H, Sun Q, Chen Y, Wu D, Liu L. Small extracellular vesicles containing miR-30a-3p attenuate the migration and invasion of hepatocellular carcinoma by targeting *SNAP23* gene. Oncogene. 2021; 40:233-245.
11. Kang MJ, Lee S, Jung U, Mandal C, Park H, Stetler-Stevenson WG, Kim YS, Moon JW, Park SH, Oh J. Inhibition of hepatic stellate cell activation suppresses tumorigenicity of hepatocellular carcinoma in mice. Am J Pathol. 2021.
12. Liao R, Sun TW, Yi Y, Wu H, Li YW, Wang JX, Zhou J, Shi YH, Cheng YF, Qiu SJ, Fan J. Expression of TREM-1 in hepatic stellate cells and prognostic value in hepatitis B-related hepatocellular carcinoma. Cancer Sci. 2012; 103:984-992.
13. Xie YX, Liao R, Pan L, Du CY. ERK pathway activation contributes to the tumor-promoting effects of hepatic stellate cells in hepatocellular carcinoma. Immunol Lett. 2017; 188:116-123.
14. Liao R, Wu H, Yi Y, Wang JX, Cai XY, He HW, Cheng YF, Zhou J, Fan J, Sun J, Qiu SJ. Clinical significance and gene expression study of human hepatic stellate cells in HBV related-hepatocellular carcinoma. J Exp Clin Cancer Res. 2013; 32:22.
15. Liao R, Sun J, Wu H, Yi Y, Wang JX, He HW, Cai XY, Zhou J, Cheng YF, Fan J, Qiu SJ. High expression of IL-17 and IL-17RE associate with poor prognosis of hepatocellular carcinoma. J Exp Clin Cancer Res. 2013; 32:3.
16. Zhou BY, Gong JH, Cai XY, Wang JX, Luo F, Jiang N, Gong JP, Du CY, Liao R. An imbalance between stellate cells and gammadeltaT cells contributes to hepatocellular carcinoma aggressiveness and recurrence. Hepatol Int. 2019; 13:631-640.
17. Kalluri R, LeBleu VS. The biology, function, and biomedical applications of exosomes. Science. 2020; 367:eaau6977.
18. Morrissey SM, Zhang F, Ding C, *et al*. Tumor-derived exosomes drive immunosuppressive macrophages in a pre-metastatic niche through glycolytic dominant metabolic reprogramming. Cell Metab. 2021;33:2040-2058.e10.
19. Jiang C, Zhang N, Hu X, Wang H. Tumor-associated exosomes promote lung cancer metastasis through multiple mechanisms. Mol Cancer. 2021; 20:117.
20. Wu J, Gao W, Tang Q, *et al*. M2 macrophage-derived exosomes facilitate HCC metastasis by transferring alphaM beta2 integrin to tumor cells. Hepatology. 2021; 73:1365-1380.
21. Shefler I, Salamon P, Mekori YA. Extracellular vesicles as emerging players in intercellular communication: Relevance in mast cell-mediated pathophysiology. Int J Mol Sci. 2021; 22.
22. Herrera M, Llorens C, Rodriguez M, *et al*. Differential distribution and enrichment of non-coding RNAs in exosomes from normal and cancer-associated fibroblasts in colorectal cancer. Mol Cancer. 2018; 17:114.
23. Muralikumar M, Manoj Jain S, Ganesan H, A KD, Pathak S, Banerjee A. Current understanding of the mesenchymal stem cell-derived exosomes in cancer and aging. Biotechnol Rep (Amst). 2021; 31:e00658.
24. Xia Y, Zhen L, Li H, Wang S, Chen S, Wang C, Yang X. MIRLET7BHG promotes hepatocellular carcinoma progression by activating hepatic stellate cells through exosomal SMO to trigger Hedgehog pathway. Cell Death Dis. 2021; 12:326.
25. Zhou Y, Ren H, Dai B, Li J, Shang L, Huang J, Shi X. Hepatocellular carcinoma-derived exosomal miRNA-21 contributes to tumor progression by converting hepatocyte stellate cells to cancer-associated fibroblasts. J Exp Clin

Cancer Res. 2018; 37:324.
26. Liao R, Liu L, Zhou J, Wei X, Huang P. Current molecular biology and therapeutic strategy status and prospects for circRNAs in HBV-associated hepatocellular carcinoma. Front Oncol. 2021; 11:697747.
27. Shi L, Liu B, Shen DD, *et al*. A tumor-suppressive circular RNA mediates uncanonical integrin degradation by the proteasome in liver cancer. Sci Adv. 2021; 7:eabe5043.
28. Bu FT, Zhu Y, Chen X, Wang A, Zhang YF, You HM, Yang Y, Yang YR, Huang C, Li J. Circular RNA circPSD3 alleviates hepatic fibrogenesis by regulating the miR-92b-3p/Smad7 axis. Mol Ther Nucleic Acids. 2021; 23:847-862.
29. Costa-Silva B, Aiello NM, Ocean AJ, *et al*. Pancreatic cancer exosomes initiate pre-metastatic niche formation in the liver. Nat Cell Biol. 2015; 17:816-826.
30. Hao TT, Liao R, Lei DL, Hu GL, Luo F. Inhibition of B7-H4 promotes hepatocellular carcinoma cell apoptosis and autophagy through the PI3K signaling pathway. Int Immunopharmacol. 2020; 88:106889.
31. Zhang PF, Wei CY, Huang XY, Peng R, Yang X, Lu JC, Zhang C, Gao C, Cai JB, Gao PT, Gao DM, Shi GM, Ke AW, Fan J. Circular RNA circTRIM33-12 acts as the sponge of MicroRNA-191 to suppress hepatocellular carcinoma progression. Mol Cancer. 2019; 18:105.
32. Wang L, Long H, Zheng Q, Bo X, Xiao X, Li B. Circular RNA circRHOT1 promotes hepatocellular carcinoma progression by initiation of NR2F6 expression. Mol Cancer. 2019; 18:119.
33. Galon J, Costes A, Sanchez-Cabo F, *et al*. Type, density, and location of immune cells within human colorectal tumors predict clinical outcome. Science. 2006; 313:1960-1964.
34. Daurkin I, Eruslanov E, Stoffs T, Perrin GQ, Algood C, Gilbert SM, Rosser CJ, Su LM, Vieweg J, Kusmartsev S. Tumor-associated macrophages mediate immunosuppression in the renal cancer microenvironment by activating the 15-lipoxygenase-2 pathway. Cancer Res. 2011; 71:6400-6409.
35. Leconet W, Petit P, Peraldi-Roux S, Bresson D. Nonviral delivery of small interfering RNA into pancreas-associated immune cells prevents autoimmune diabetes. Mol Ther. 2012; 20:2315-2325.
36. Benbow JH, Marrero E, McGee RM, Brandon-Warner E, Attal N, Feilen NA, Culberson CR, McKillop IH, Schrum LW. Hepatic stellate cell-derived exosomes modulate macrophage inflammatory response. Exp Cell Res. 2021; 405:112663.
37. Dvorak P, Leupen S, Soucek P. Functionally significant features in the 5' untranslated region of the ABCA1 gene and their comparison in vertebrates. Cells. 2019; 8:623.
38. Orafaie A, Matin MM, Sadeghian H. The importance of 15-lipoxygenase inhibitors in cancer treatment. Cancer Metastasis Rev. 2018; 37:397-408.
39. Ma J, Zhang L, Zhang J, Liu M, Wei L, Shen T, Ma C, Wang Y, Chen Y, Zhu D. 15-lipoxygenase-1/15-hydroxyeicosatetraenoic acid promotes hepatocellular cancer cells growth through protein kinase B and heat shock protein 90 complex activation. Int J Biochem Cell Biol. 2013; 45:1031-1041.
40. Lambert AW, Weinberg RA. Linking EMT programmes to normal and neoplastic epithelial stem cells. Nat Rev Cancer. 2021; 21:325-338.
41. Liu J, Ren L, Li S, Li W, Zheng X, Yang Y, Fu W, Yi J, Wang J, Du G. The biology, function, and applications of exosomes in cancer. Acta Pharm Sin B. 2021; 11:2783-2797.
42. Zhu C, Su Y, Liu L, Wang S, Liu Y, Wu J. Circular RNA hsa_circ_0004277 stimulates malignant phenotype of hepatocellular carcinoma and epithelial-mesenchymal transition of peripheral cells. Front Cell Dev Biol. 2020; 8:585565.
43. Yau T, Kang YK, Kim TY, *et al*. Efficacy and safety of nivolumab plus ipilimumab in patients with advanced hepatocellular carcinoma previously treated with sorafenib: The CheckMate 040 Randomized Clinical Trial. JAMA Oncol. 2020; 6:e204564.

Received June 25, 2022; Revised July 27, 2022; Accepted August 3, 2022.

[§]These authors contributed equally to this work.
**Address correspondence to:*
Rui Liao, Department of Hepatobiliary Surgery, the First Affiliated Hospital of Chongqing Medical University, Chongqing 400016, China.
E-mail: liaorui99@163.com

Released online in J-STAGE as advance publication August 7, 2022.

Original Article

DOI: 10.5582/bst.2021.01306

Association of MTHFR 677C>T polymorphism with pregnancy outcomes in IVF/ICSI-ET recipients with adequate synthetic folic acid supplementation

Feijun Ye[1,§], Siwei Zhang[2,3,4,§], Qing Qi[2,3,4], Jing Zhou[2,3,4], Yan Du[2,3,4,*], Ling Wang[2,3,4,*]

[1] Reproductive Medicine Center, Zhoushan Maternal and Child Health Care Hospital, Zhoushan, Zhejiang, China;
[2] Laboratory for Reproductive Immunology, Obstetrics and Gynecology Hospital of Fudan University, Shanghai, China;
[3] The Academy of Integrative Medicine, Fudan University, Shanghai, China;
[4] Shanghai Key Laboratory of Female Reproductive Endocrine-related Diseases, Shanghai, China.

SUMMARY Methylenetetrahydrofolate reductase (*MTHFR*) genetic polymorphism rs1801133 (677C>T) will decrease the utilization of folate. Folate deficiency and its resulting homocysteine (HCY) accumulation can impair female fertility. Folic acid (FA) supplementation is necessary in pregnant women who are undergoing in-vitro fertilization (IVF)/intracytoplasmic sperm injection (ICSI) - embryo transfer (ET), and especially in women with *MTHFR* rs1801133 C-to-T mutations. At present, affordable and accessible synthetic FA is mainly used. However, some studies have suggested that 5-methylenetetrahydrofolate (5-MTHF), a type of active FA, may be more suitable for women with the *MTHFR* 677C>T polymorphism, since it is safer and more effective. This retrospective study aimed to evaluate whether the *MTHFR* rs1801133 gene polymorphism is related to the pregnancy outcomes of IVF/ICSI-ET recipients after sufficient supplementation with FA instead of 5-MTHF. Data on 692 women undergoing IVF/ICSI-ET and taking adequate FA were collected. Participant characteristics were compared using the Kruskal-Wallis test and Pearson chi-square test. Logistic regressions were used to calculate the odds ratio (OR) and 95% confidence interval (95% CI), after adjusting for age, BMI, method of fertilization, method of embryo transfer and number of embryos transferred. An additive model (T/T *vs.* C/C), dominant model (C/T + T/T *vs.* C/C), and recessive model (T/T *vs.* C/T + C/C) were evaluated. Analysis revealed that *MTHFR* rs1801133 in IVF/ICSI-ET women with adequate FA supplementation was not associated with the pregnancy rate but with age (OR = 0.91, 95% CI = 0.88, 0.94, $P < 0.001$) and BMI (OR = 0.95, 95% CI = 0.90, 0.997, $P = 0.037$). In 349 clinically pregnant women, no association of the *MTHFR* 677C>T with pregnancy outcomes was found in the additive model, dominant model, or recessive model. Of the 273 women with positive pregnancy outcomes, 34 had a preterm delivery. *MTHFR* 677C>T was not associated with a preterm delivery after adjusting for age and BMI. The current results indicated that *MTHFR* polymorphism rs1801133 was not related to the pregnancy rate or pregnancy outcomes of women undergoing IVF/ICSI-ET with adequate synthetic FA supplementation, suggesting that simple supplementation with less expensive and readily available FA, rather than expensive 5-MTHF, appeared to be appropriate.

Keywords methylenetetrahydrofolate reductase, IVF/ICSI-ET, folic acid supplementation, active folic acid, 5-MTHF, adverse pregnancy, preterm delivery

1. Introduction

Folic acid (FA) is an important type of vitamin B, which is involved in various biological transmethylation reactions that include many physiological and pathological processes. Folate deficiency elevates the frequency of uracil misincorporation into DNA, disrupts nucleic acid integrity, slows DNA replication, and increases the risk of chromosomal breakage, thereby negatively affecting female fertility and fetal viability (*1*). Severe folate deficiency before and during pregnancy can lead to oocyte and follicle development disorder, reduced endometrial receptivity, and impair the implantation process and fetal development (*2*). In addition, folate deficiency can lead to the accumulation of homocysteine (HCY), which may damage the

vascular endothelium and disrupt the coagulation and fibrinolytic system, subsequently causing hypercoagulability and eventually leading to recurrent abortion, fetal growth restriction, and stillbirth (*3-5*).

The methylenetetrahydrofolate reductase (*MTHFR*) gene is located at the end of the short arm of chromosome 1 (chr1:11796321), and is 2.2 kb long. One of the most common single nucleotide polymorphisms (SNPs) in the *MTHFR* gene is rs1801133 (677C>T). A systematic review and meta-analysis indicated that the overall T allele frequency of *MTHFR* rs1801133 was 36.9% in Chinese (*6*), and 78.4% of Chinese people have homozygous or heterozygous mutations (*7*); this figure exceeds that in many other countries. The C-to-T transition results in a missense mutation that changes alanine (Ala) to valine (Val), which reduces the thermal stability and activity of MTHFR (*8*). The enzyme activity of individuals with homozygous TT mutation was about 30% of that in individuals with the wild-type (CC) genotype, whereas individuals with the heterozygous genotype (CT) had about 65% of the wild-type enzyme activity (*9*). Subsequently, the mutated genotype reduced the capacity to convert 5,10-methylenetetrahydrofolate (5,10-MTHF) to 5-methylenetetrahydrofolate (5-MTHF), the predominant circulating form of folate, thus decreasing the utilization of folate (*10*) (Figure 1). Several studies have suggested that the *MTHFR* gene is a major genetic factor for adverse pregnancy outcomes (APOs) (*11-14*). Moreover, intake of FA from supplements has been found to reduce the risk of spontaneous abortion and pregnancy complications (*15-17*).

In-vitro fertilization (IVF), intracytoplasmic sperm injection (ICSI), and embryo transfer (ET) are assisted reproductive techniques (ARTs). Several studies have indicated that women after IVF/ICSI-ET have a higher spontaneous miscarriage rate than those after natural conception (*18,19*). In addition, IVF/ICSI-ET was found to be associated with preterm delivery (*20*). With the implementation of the three-child policy and the increase in women of advanced maternal age in China, the need for and use of ART is also estimated to be increasing.

FA supplementation is necessary in pregnant women who are undergoing ART, and especially in women with *MTHFR* rs1801133 C-to-T mutations. Therefore, the choice of the type of FA supplementation is not only a family-related but also a social issue that needs to be addressed. At present, synthetic FA is mainly used. Synthetic FA is a form of FA extracted and synthesized from the chemical raw material L-N-p-aminophenylmethylcool glutamic acid or 2,4,5- triamino -6- hydroxypyrimidine sulfate, and it has the advantages of good stability and affordability. China has been implementing a folate fortification policy since 2009, providing free supplements of synthetic FA to women of childbearing age.

Nevertheless, studies have pointed out that the conversion of synthetic FA to 5-MTHF is limited in women with the *MTHFR* rs1801133 CT or TT genotype (*21,22*), and FA is inactive until reduced into the bioactive folate derivative, 5-MTHF (*23*). Active FA, 5-MTHF, is the main circulating form of folate in the body, and it can bypass the MTHFR block. However, whether active FA is better than synthetic FA in preventing APOs remains a subject of controversy (*24,25*).

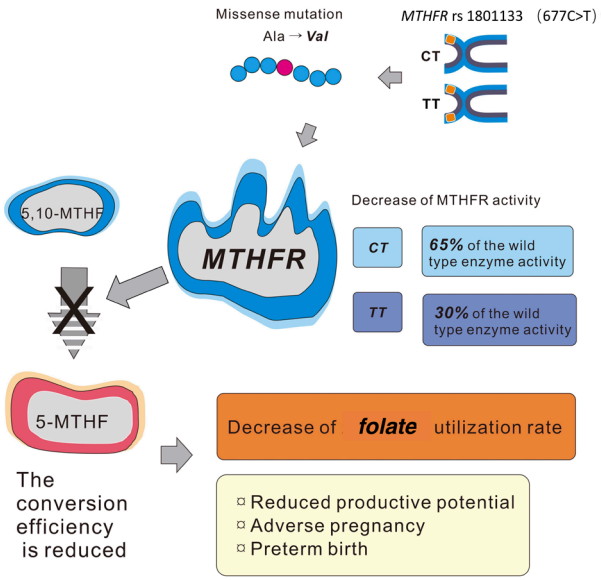

Figure 1. Possible mechanism of *MTHFR* rs1801133 affecting folic acid and pregnancy outcomes. MTHFR rs1801133 will lead to a missense mutation that changes Ala to Val, which can decrease the thermal stability and reduce the activity of MTHFR. The enzyme activity of individuals with homozygous TT mutation is about 30% of that in individuals with the wild-type (CC) genotype, whereas individuals with the heterozygous genotype (CT) have about 65% of the wild-type enzyme activity. Subsequently, the mutated genotype reduces the capacity to convert 5,10-MTHF to 5-MTHF, the predominant circulating form of folic acid, thus decreasing the utilization of folic acid.

Folate levels in women are still low even in countries with mandatory folate fortification (*21*). Since China is a developing country with a large population, affordable and accessible synthetic FA is more readily available than 5-MTHF, which is more expensive. Therefore, the aim of the current study was to evaluate whether *MTHFR* rs1801133 gene polymorphism was related to the pregnancy outcomes of IVF/ICSI-ET subjects after taking sufficient synthetic FA supplements.

2. Materials and Methods

2.1. Study population

The study population was 692 women who underwent IVF/ICSI-ET at Zhoushan Women's and Children's Health Hospital from 2016 to 2020. All of the women had adequate synthetic FA supplementation depending on their genotype, and they sought the treatment due to

fallopian tube or ovulation disorders or rare, weak, or abnormal sperm of their husbands.

2.2. Genotype determination

The extraction of whole-genome DNA from blood samples was performed using QIAquick PCR purification kits (QIAGEN, Germany). The *MTHFR* rs1801133 genotype was determined using a fluorescence PCR detection kit (PCR-fluorescence probe) designed by Osama Medicine (Shenzhen, Guangdong, China). Genotyping was performed under the following conditions: a 25-μL whole blood sample, a 16-μL PCR reaction system, reaction conditions of 45 cycles, 95°C denaturation for 15 s, and 60°C annealing/extension for 1 min, as recommended by the manufacturer. After the reaction was completed, the end point fluorescence in sample wells was read on the ABI 7900 fluorescence quantitative PCR instrument (Applied Biosystems, Foster City, CA), and the genotyping results for each sample were determined using the ABI 3730 Genetic Analyzer (Applied Biosystems, Foster City, CA).

2.3. Ovarian stimulation and oocyte retrieval

A controlled ovarian hyperstimulation protocol was tailored to the individual. According to comprehensive factors such as age of the woman, ovarian preparation, and outcomes of previous ovulation induction protocols, a long luteal phase protocol, a long early follicular phase protocol, an overlength protocol, a short protocol, an antagonist protocol, a natural cycle protocol, or a microstimulation protocol was adopted. When the diameter of two dominant follicles was ≥ 18 mm and that of three follicles ≥ 16mm, human chorionic gonadotropin (HCG) (a recombinant HCG alfa solution for injection, Merck Serono Sweden; chorionic gonadotrophin for injection, Livzon China, 6500/8500 IU) was injected at 9 PM on the same night. If the follicle diameter was ≥ 14 mm and urine luteinizing hormone (LH) was positive or blood LH > 10 mIU/ml, the oocyte was retrieved 24 hours after the immediate injection of HCG. Oocyte retrieval was performed under ultrasound guidance using a K-OPSD oocyte retrieval needle (Cook, Australia).

2.4. IVF/ ICSI-ET

The oocytes and sperm are then fertilized using IVF or ICSI and cultured *in vitro* on cleavage stage/blastocyst culture medium (Vitrolife Sweden). Embryo transfer was performed using a K-JETS catheter (Cook, Australia) 3-5 days after oocyte retrieval. Women younger than 35 years of age or who had received IVF/ ICSI-ET for the first time underwent single embryo transfer, while women older than 35 or who had failed IVF/ ICSI-ET several times received 2-3 embryos.

2.5. Determination of pregnancy

Twelve days after transplantation, a urine pregnancy test or a blood HCG quantitative test was conducted. For HCG-positive patients, the first vaginal ultrasound was performed 21 days after transplantation to exclude ectopic pregnancy. Ultrasound was performed again after 28 days to determine the number of embryos and their development.

2.6. FA supplementation

Patients were encouraged to take FA (Silian, China), instead of 5-MTHF, depending on their genotype. For the CC genotype: 400 μg/day FA was taken three months before pregnancy, 400 μg/day FA was taken in early pregnancy (0-12 weeks), and food supplementation was considered in middle/late pregnancy (13-40 weeks), but no extra supplementation was needed. For the CT genotype: FA was supplemented 400 μg/day three months before pregnancy, 800 μg/day in early pregnancy (0-12 weeks), and 400 μg/day in middle/late pregnancy (13-40 weeks). For the TT genotype: FA was supplemented 800 μg/day three months before pregnancy, 800 μg/day in the early pregnancy (0-12 weeks), and 400 μg/day in middle/late pregnancy (13-40 weeks).

2.7. Statistical analysis

Characteristics of participants with different genotypes were compared using the Kruskal–Wallis test for continuous variables and the chi-square test or Fisher's exact test for discrete variables. Genotype and allele frequencies were calculated. Observed genotype frequencies in different genotypes were separately tested for deviation from the Hardy–Weinberg equilibrium (HWE) using the exact test. Logistic regressions were used to calculate the odds ratio (OR) and 95% confidence interval (95% CI), after adjusting for age, body mass index (BMI), method of fertilization, method of embryo transfer and number of embryos transferred. An additive model (T/T *vs.* C/C), dominant model (C/T + T/T *vs.* C/C), and recessive model (T/T *vs.* C/T + C/C) were evaluated to assess the strength of association between *MTHFR* polymorphism rs1801133 and pregnancy outcomes. All significance tests were two-sided; a P value of < 0.05 was considered to be statistically significant. Data analyses were performed using the software platform SPSS v.26.0 (IBM, Armonk, NY, USA).

3. Results

3.1. Participant characteristics

The age range of the 692 women was between 22 and 49 years of age, and the range of their BMI was

Table 1. Participant characteristics

Characteristics	*MTHFR* rs1801133 genotype			*p*
	CC (*n* = 316)	CT (*n* = 226)	TT (*n* = 150)	
Age, years (mean ± SD)	33.13 ± 4.64	32.51 ± 4.65	32.91 ± 4.33	0.34[a]
BMI, kg/m^2 (mean ± SD)	22.11 ± 2.95	22.32 ± 3.01	22.47 ± 3.17	0.53[a]
Method of fertilization (*n*, %)				
IVF	235 (74.37)	173 (76.55)	114 (76.00)	0.83[b]
ICSI	81 (25.63)	53 (23.45)	36 (24.00)	
Method of embryo transfer (*n*, %)				
FET	251 (79.43)	171 (75.66)	121 (80.67)	0.44[b]
ET	65 (20.57)	55 (24.34)	29 (19.33)	
Number of embryos transferred (*n*, %)				
1	99 (31.33)	71 (31.42)	43 (28.67)	0.82[b]
≥ 2	217 (68.67)	155 (68.58)	107 (71.33)	

BMI: body mass index; ET: fresh embryo transfer; FET: frozen embryo transfer; ICSI: intracytoplasmic sperm injection; IVF: *in-vitro* fertilization; [a]Kruskal-Wallis test. [b]Pearson chi-square test.

Table 2. Pregnancy outcomes

Pregnancy outcome	*MTHFR* rs1801133 genotype			*p*
	CC (*n* = 316)	CT (*n* = 226)	TT (*n* = 150)	
Not pregnant (*n*, %)	149 (47.15)	89 (39.38)	69 (46.00)	0.18[a*]
Pregnancy	167 (52.85)	137 (60.62)	81 (54.00)	
Biochemical pregnancy (*n*, %)	21 (12.57)	12 (8.76)	3 (3.70)	
Positive pregnancy outcome (*n*, %)	114 (68.26)	95 (69.34)	64 (79.01)	
Adverse pregnancy (*n*, %)	32 (19.16)	30 (21.90)	14 (17.28)	
Miscarriage (*n*, %)	22 (68.75)	21 (7.00)	9 (64.29)	
Ectopic pregnancy (*n*, %)	9 (28.13)	6 (2.00)	4 (28.57)	
Preterm delivery (*n*, %)	13 (11.40)	10 (10.53)	11 (17.19)	0.42[a]

[a]Pearson chi-square test. [*]Between pregnant patients and non-pregnant patients.

between 32.66 kg/m^2 and 16.02 kg/m^2. Based on the genotype of *MTHFR* rs1801133, 316 (45.66%) women were classified as wildtype homozygotes (CC), 226 (32.66%) women were classified as heterozygotes (CT), and 150 (21.68%) women were classified as mutated homozygotes (TT). There were no differences found regarding age (P = 0.34), BMI (P = 0.53), method of fertilization (P = 0.83), method of embryo transfer (P = 0.44), or number of embryos transferred (P = 0.82) among the three genotypes (Table 1).

3.2. Pregnancy outcomes

The pregnancy outcomes were compared among the different genotypes. Results revealed no significant differences in pregnancy rates of wildtype homozygotes (CC, 47.15%), heterozygotes (CT, 39.38%), or mutated homozygotes (TT, 46.00%). Among pregnant women, 12.75% of wildtype homozygotes (CC), 8.76% of heterozygotes (CT) and 3.7% of mutated homozygotes (TT) had a biochemical pregnancy. One hundred and fourteen pregnant women with the CC genotype (114/167, 68.26%), 95 with the CT genotype (95/137, 69.34%), and 64 with the TT genotype (64/81, 79.01%) had a positive pregnancy outcome (live birth ≥ 1), while 32 with the CC genotype (32/167, 19.16%), 30 with the CT genotype (30/137, 21.90%), and 14 with the TT genotype (14/81, 17.28%) had adverse pregnancy outcomes including miscarriage, ectopic pregnancy, and other pathological pregnancies (Table 2). The proportion of preterm deliveries by women with a positive pregnancy outcome is also shown in Table 2.

3.3. Association of the *MTHFR* rs1801133 genotype with a successful pregnancy

All DNA samples were successfully genotyped for rs1801133, and this SNP deviated from HWE (P < 0.01) in women receiving IVF/ICSI-ET. The proportions of each genotype among 385 pregnant and 307 non-

Table 3. Association of *MTHFR* rs1801133 with pregnancy or no pregnancy

Variables	*N* (%)		OR (95% CI)	*p*
	Pregnancy (*n* = 385)	No pregnancy (*n* = 307)		
Genotype/Allele				
CC	167 (43.38)	167 (43.38)	reference	
CT	137 (35.58)	137 (35.58)	1.35 (0.94, 1.95)	0.10
TT	81 (21.04)	81 (21.04)	1.03 (0.68, 1.55)	0.89
Age			0.91 (0.88, 0.94)	< 0.001
BMI			0.95 (0.90, 0.997)	0.04
Additive model				
CC	167 (43.38)	167 (43.38)	reference	
TT	81 (21.04)	81 (21.04)	1.02 (0.68, 1.54)	0.92
Dominant model				
CC	167 (43.38)	167 (43.38)	reference	
CT+TT	218 (56.62)	218 (56.62)	1.21 (0.88, 1.66)	0.23
Recessive model				
TT	81 (21.04)	81 (21.04)	reference	
CT+CC	304 (78.96)	304 (78.96)	1.11 (0.76, 1.62)	0.60

pregnant women are shown in Table 3. Logistic regression was used to analyze the association between the*MTHFR* rs1801133 genotype and a successful pregnancy, after adjusting for age, BMI, method of fertilization, method of embryo transfer, and number of embryos transferred. An additive model, dominant model, and recessive model were all assessed (Table 3). Results indicated that *MTHFR* genetic polymorphism rs1801133 was not associated with a successful pregnancy but with age (OR = 0.91, 95% CI = 0.88-0.94, $P < 0.001$) and BMI (OR = 0.95, 95% CI = 0.90, 0.997, $P = 0.04$) (Table 3) (Figure 2).

3.4. Association of the *MTHFR* rs1801133 genotype with pregnancy outcomes

Of 385 pregnant women, 349 were clinically pregnant, and 36 were biochemically pregnant. The proportions of genotypes in positive and adverse pregnancy outcomes are shown in Table 4. Results indicated that after adjusting for covariates, *MTHFR* rs1801133 was not associated with pregnancy outcomes in the additive model, dominant model, or recessive model. However, a younger age (OR = 0.92, 95% CI = 0.86-0.98, $P = 0.01$) was positively associated with pregnancy outcomes (Table 4) (Figure 2).

3.5. Association of the *MTHFR* rs1801133 genotype with preterm delivery

The association of *MTHFR* rs1801133 with a preterm delivery was further analyzed in 273 women with positive pregnancy outcomes. The genotype proportions in preterm deliveries and normal deliveries are shown in Table 5. *MTHFR* rs1801133 was not associated with a preterm delivery after adjusting for age and BMI (Table 5) (Figure 2).

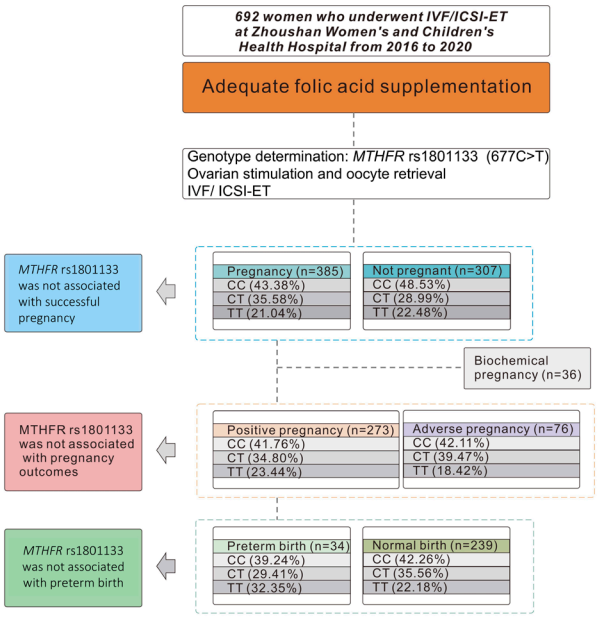

Figure 2. Flow diagram of the study population and results. A total of 692 women were included. They all received sufficient folic acid supplementation, and their genotype of *MTHFR* rs1801133 was determined. These participants were divided into two groups depending on whether they were pregnant or not. Then, the participants who were pregnant were divided into two groups, those with a positive pregnancy and those with an adverse pregnancy. The participants with a positive pregnancy were divided into two groups, those with a preterm delivery and those with a normal delivery.

Table 4. Association of the *MTHFR* rs1801133 genotype with pregnancy outcomes

Variables	*N* (%)		OR (95% CI)	*p*
	Positive pregnancy (*n* = 273)	Adverse pregnancy (*n* = 76)		
Genotype/Allele				
CC	114 (41.76)	32 (42.11)	reference	
CT	95 (34.80)	30 (39.47)	0.85 (0.47, 1.51)	0.57
TT	64 (23.44)	14 (18.42)	1.29 (0.63, 2.61)	0.49
Age			0.92 (0.86, 0.98)	0.01
BMI			0.99 (0.90, 1.07)	0.73
Additive model				
CC	114 (41.76)	32 (42.11)	reference	
TT	64 (23.44)	14 (18.42)	1.28 (0.62, 2.65)	0.50
Dominant model				
CC	114 (41.76)	32 (42.11)	reference	
CT+TT	159 (58.24)	44 (57.89)	0.99 (0.59, 1.67)	0.96
Recessive model				
TT	64 (23.44)	14 (18.42)	reference	
CT+CC	209 (76.56)	62 (81.58)	0.72 (0.37, 1.39)	0.33

Table 5. Association of the *MTHFR* rs1801133 genotype with a preterm delivery

Variables	*N* (%)		OR (95% CI)	*p*
	Preterm delivery (*n* = 34)	Normal delivery (*n* = 239)		
Genotype/Allele				
CC	13 (38.24)	101 (42.26)	reference	
CT	10 (29.41)	85 (35.56)	0.89 (0.37, 2.16)	0.80
TT	11 (32.35)	53 (22.18)	1.63 (0.68, 3.94)	0.28
Age			0.93 (0.84, 1.03)	0.15
BMI			0.97 (0.86, 1.10)	0.66
Additive model				
CC	13 (38.24)	101 (42.26)	reference	
TT	11 (32.35)	53 (22.18)	1.65 (0.68, 3.98)	0.27
Dominant model				
CC	13 (38.24)	101 (42.26)	reference	
CT+TT	21 (61.76)	138 (57.74)	1.16 (0.55, 2.45)	0.70
Recessive model				
TT	11 (32.35)	53 (22.18)	reference	
CT+CC	23 (67.65)	186 (77.82)	0.58 (0.26, 1.29)	0.18

4. Discussion

This study found no association between *MTHFR* polymorphism rs1801133 and pregnancy outcomes of women undergoing IVF/ICSI-ET with adequate synthetic FA supplementation. *MTHFR* rs1801133 fits the additive model, but results were also analyzed in a dominant model and a recessive model. Age was found to be related to the pregnancy rate (OR = 0.91, 95% CI = 0.88-0.94, $P < 0.001$) and pregnancy outcome (OR = 0.92, 95% CI = 0.86-0.98, $P = 0.01$), which was consistent with the results of previous studies (*18,26*). Older women may have an increased risk of impaired oocyte quality and chromosomal abnormalities and decreased endometrial receptivity (*27-29*). In addition, BMI also had an impact on the pregnancy rate (OR = 0.95, 95% CI = 0.90, 0.997, $P = 0.04$). Obese women often have impaired folliculogenesis, ovulation, and conception, resulting in decreased reproductive potential (*30*).

The conversion of 5,10-MTHF to 5-MTHF, a co-substrate for the re-methylation of HCY to methionine, requires the protein encoded by the *MTHFR* gene. The T allele of rs1801133 will lead to decreased activity of MTHFR, thus affecting the conversion of 5,10-MTHFR to 5-MTHF, and reduce the amount of folate circulating in the blood. In addition, the T allele of rs1801133 can also reduce the rate of FA utilization (*8*). Studies have been conducted to evaluate the association between *MTHFR* genetic polymorphism rs1801133 and pregnancy outcomes. Some have found that the mutated T allele of *MTHFR* rs1801133 was associated with a higher risk of adverse outcomes, including spontaneous abortion, premature birth, and stillbirth (*2,11,31-33*).

Folate deficiency and its resulting HCY accumulation can impair female fertility; possible mechanisms for this include reduced cell division, increased apoptosis, overproduction of inflammatory cytokines, impaired nitric oxide (NO) metabolism, oxidative stress, and defective methylation reaction (*34*). Moreover, maternal demand for folate increases during pregnancy, and a maternal folate deficiency often leads to APOs (*35*). Previous *in vivo* experiments have found that in the absence of maternal folate, placental mTOR signaling and amino acid transporter activity are inhibited (*36*) as well as the uterine decidualization (*37*) and decidual angiogenesis in pregnant mice (*38*), subsequently causing placental dysplasia and dysfunction and ultimately resulting in fetal growth restriction. A case-control study in Venezuela confirmed the association between maternal folate deficiency and an increased risk of a preterm delivery at the end of the third trimester and in labor (*39*). Another case-control study in Sweden suggested that the increased risk of early spontaneous abortion was also associated with low plasma folate levels (*40*).

Taking high doses of FA can prevent developmental delay and placental abnormalities (*41*) that may reduce the risk of low birth weight and premature birth (*36*). FA supplementation is especially necessary in patients undergoing IVF/ICSI-ET because of the inherent risk of an adverse pregnancy. Patients taking FA supplements were found to have significantly reduced HCY levels in follicle fluid, indicating that the recovered oocytes would be more mature and of better embryo quality (*42*).

However, studies in recent years have indicated that 5-MTHF is safer than FA. 5-MTHF is comparable to FA in reducing HCY, and it is comparable to or more effective than FA in maintaining serum and plasma folate levels (*43*). Compared to FA, 5-MTHF is less likely to cause unmetabolized folic acid (UMFA) syndrome or mask a B12 deficiency (*43*).

A Chinese study analyzed *MTHFR* polymorphism in normal pregnant patients and found that active FA (5-MTHF) had a significant therapeutic effect for patients with *MTHFR* rs1801133 C-to-T mutations. In patients without such a mutation, the therapeutic effect of 5-MTHF did not differ significantly from that of FA (*25*). A possible explanation for this is that 5-MTHF does not require the already reduced activity of MTHFR in individuals with the *MTHFR* 677C>T polymorphism to convert 5,10-MTHFR to 5-MTHF to become effective, but it can function directly.

5-MTHF appears to be more advantageous in women with the *MTHFR* 677C>T polymorphism than FA. However, a randomized, double-blind, placebo-controlled trial found that there was no difference in the abortion rate between women with *MTHFR* 677C>T polymorphism taking 5-MTHF and those taking FA; that is, there was no beneficial effect of 5-MTHF compared to FA supplementation (*44*). The current study also found that for women undergoing IVF/ICSI-ET, taking a sufficient amount of FA, rather than 5-MTHF, starting 3 months before conception can lead to a result where the *MTHFR* 677C>T genotype is irrelevant to the pregnancy outcome.

Although 5-MTHF has a slight advantage in increasing serum folate levels for the population with the *MTHFR* 677C>T polymorphism, previous studies found no difference in the effect on HCY in groups taking FA or 5-MTHF (*44,45*). Pharmacokinetic studies have also attempted to explain the possible reason why 5-MTHF did not appear superior to FA in improving pregnancy outcomes. On each of the four mornings following the start of dosing (7.5 mg/day), the serum total folate level of 5-MTHF was 23 to 55% higher than that of FA. Interestingly, 12 days later, when both groups continued to take a dose of 0.4 mg/day, serum total folate levels in the 5-MTHF and FA groups were indistinguishable (*21*). One of the advantages of 5-MTHF is that it can replenish the body's reserves more quickly in women with a folate deficiency. However, the quick replenishment for women undergoing IVF/ICSI-ET seems unnecessary since they usually start taking a full, genotypic dose of FA three months before conception.

For developing countries like China, affordable and more accessible synthetic FA seems to be cost-effective for most women than expensive 5-MTHF at the current stage. Because, according to the current results, the use of synthetic FA alone, in a sufficient amount and with enough time, can nullify the association between the *MTHFR* 677C>T genotype and pregnancy outcomes in IVF/ICSI-ET recipients. However, the related mechanism and whether FA alone is enough to eliminate the effects of the *MTHFR* 677C>T polymorphism still needs to be investigated further.

In summary, the current study did not find that *MTHFR* polymorphism rs1801133 was related to the pregnancy rate or pregnancy outcomes of women undergoing IVF/ICSI-ET with adequate synthetic FA supplementation, suggesting that simple supplementation with less expensive and readily available synthetic FA, rather than expensive 5-MTHF, appeared to be appropriate.

Acknowledgements

The authors wish to sincerely thank Peng Li and Suna Tian for their assistance in preparing the figures in this manuscript.

Funding: This work was supported by grants for a project under the Scientific and Technological Innovation Action Plan of the Shanghai Natural Science Fund (grant no. 20ZR1409100 to L Wang), a project of the Chinese Association of Integration of Traditional and Western Medicine special foundation for Obstetrics and Gynecology-PuZheng Pharmaceutical Foundation (grant no. FCK-PZ-08 to L Wang), a project for hospital management of the Shanghai Hospital Association (grant no. X2021046 to L Wang), and a clinical trial project of the Special Foundation for Healthcare Research of the Shanghai Municipal Health Commission (Grant No. 202150042 to L Wang).

Conflict of Interest: The authors have no conflicts of interest to disclose.

References

1. Enciso M, Sarasa J, Xanthopoulou L, Bristow S, Bowles M, Fragouli E, Delhanty J, Wells D. Polymorphisms in the *MTHFR* gene influence embryo viability and the incidence of aneuploidy. Hum Genet. 2016; 135:555-568.
2. Zhang Y, He X, Xiong X, Chuan J, Zhong L, Chen G, Yu D. The association between maternal methylenetetrahydrofolate reductase C677T and A1298C polymorphism and birth defects and adverse pregnancy outcomes. Prenat Diagn. 2019; 39:3-9.
3. Nair RR, Khanna A, Singh R, Singh K. Association of maternal and fetal *MTHFR* A1298C polymorphism with the risk of pregnancy loss: A study of an Indian population and a meta-analysis. Fertil Steril. 2013; 99:1311-1318 e1314.
4. Zhou J, Huang Z, Pan X, Leung WT, Li C, Chen L, Zhang Y, Wang L, Sima Y, Zhang N, Qiu X, Li L, Wang L. New thoughts in exploring the pathogenesis, diagnosis, and treatment of threatened abortion. Biosci Trends. 2019; 13:284-285.
5. Qian J, Zhang N, Lin J, Wang C, Pan X, Chen L, Li D, Wang L. Distinct pattern of Th17/Treg cells in pregnant women with a history of unexplained recurrent spontaneous abortion. Biosci Trends. 2018; 12:157-167.
6. Yang B, Fan S, Zhi X, Xia R, Wang Y, Zheng Q, Sun G. Geographical and ethnic distribution of *MTHFR* gene polymorphisms and their associations with diseases among Chinese population. Clin Genet. 2017; 92:243-258.
7. Yang B, Liu Y, Li Y, Fan S, Zhi X, Lu X, Wang D, Zheng Q, Wang Y, Wang Y, Sun G. Geographical distribution of *MTHFR* C677T, A1298C and *MTRR* A66G gene polymorphisms in China: Findings from 15357 adults of Han nationality. PLoS One. 2013; 8:e57917.
8. Mo H, Rao M, Wang G, Long YX, Wang HW, Tang L. Polymorphism of *MTHFR* 1298A>C in relation to adverse pregnancy outcomes in Chinese populations. Mol Genet Genomic Med. 2019; 7:e642.
9. Ulrich CM, Kampman E, Bigler J, Schwartz SM, Chen C, Bostick R, Fosdick L, Beresford SA, Yasui Y, Potter JD. Lack of association between the C677T *MTHFR* polymorphism and colorectal hyperplastic polyps. Cancer Epidemiol Biomarkers Prev. 2000; 9:427-433.
10. Mazokopakis EE, Papadomanolaki MG. Methylene tetrahydrofolate reductase (*MTHFR*) gene polymorphisms among Greek women with medical history of recurrent pregnancy loss. Arch Gynecol Obstet. 2020; 302:1555-1556.
11. Kos BJP, Leemaqz SY, McCormack CD, Andraweera PH, Furness DL, Roberts CT, Dekker GA. The association of parental methylenetetrahydrofolate reductase polymorphisms (*MTHFR* 677C>T and 1298A>C) and fetal loss: A case-control study in South Australia. J Matern Fetal Neonatal Med. 2020; 33:752-757.
12. Du B, Shi X, Yin C, Feng X. Polymorphisms of methalenetetrahydrofolate reductase in recurrent pregnancy loss: An overview of systematic reviews and meta-analyses. J Assist Reprod Genet. 2019; 36:1315-1328.
13. Al-Achkar W, Wafa A, Ammar S, Moassass F, Jarjour RA. Association of methylenetetrahydrofolate reductase C677T and A1298C gene polymorphisms with recurrent pregnancy loss in Syrian women. Reprod Sci. 2017; 24:1275-1279.
14. Chen L, Li D, Wang L. Research progress on genetics related factors of recurrent spontaneous abortion. J Reprod Med. 2017; 26:1158-1162.
15. Serapinas D, Boreikaite E, Bartkeviciute A, Bandzeviciene R, Silkunas M, Bartkeviciene D. The importance of folate, vitamins B6 and B12 for the lowering of homocysteine concentrations for patients with recurrent pregnancy loss and *MTHFR* mutations. Reprod Toxicol. 2017; 72:159-163.
16. Haider BA, Bhutta ZA. Multiple-micronutrient supplementation for women during pregnancy. Cochrane Database Syst Rev. 2017; 4:CD004905.
17. Mao YY, Yang L, Li M, Liu J, Zhu QX, He Y, Zhou WJ. Periconceptional folic acid supplementation and the risk of spontaneous abortion among women who prepared to conceive: Impact of supplementation initiation timing. Nutrients. 2020; 12:2264.
18. Bu Z, Hu L, Su Y, Guo Y, Zhai J, Sun YP. Factors related to early spontaneous miscarriage during IVF/ICSI treatment: an analysis of 21,485 clinical pregnancies. Reprod Biomed Online. 2020; 40:201-206.
19. Basirat Z, Kashifard M, Golsorkhtabaramiri M, Mirabi P. Factors associated with spontaneous abortion following intracytoplasmic sperm injection (ICSI). JBRA Assist Reprod. 2019; 23:230-234.
20. Jancar N, Mihevc Ponikvar B, Tomsic S, Vrtacnik Bokal E, Korosec S. Is IVF/ICSI an independent risk factor for spontaneous preterm birth in singletons? A population-based cohort study. Biomed Res Int. 2018; 2018:7124362.
21. Bailey SW, Ayling JE. The pharmacokinetic advantage of 5-methyltetrahydrofolate for minimization of the risk for birth defects. Sci Rep. 2018; 8:4096.
22. Servy EJ, Jacquesson-Fournols L, Cohen M, Menezo YJR. MTHFR isoform carriers. 5-MTHF (5-methyl tetrahydrofolate) *vs* folic acid: A key to pregnancy outcome: A case series. J Assist Reprod Genet. 2018; 35:1431-1435.
23. Pannia E, Hammoud R, Kubant R, Sa JY, Simonian R,

Wasek B, Ashcraft P, Bottiglieri T, Pausova Z, Anderson GH. High intakes of [6S]-5-methyltetrahydrofolic acid compared with folic acid during pregnancy programs central and peripheral mechanisms favouring increased food intake and body weight of mature female offspring. Nutrients. 2021; 13.
24. Cirillo M, Fucci R, Rubini S, Coccia ME, Fatini C. 5-methyltetrahydrofolate and vitamin B12 supplementation is associated with clinical pregnancy and live birth in women undergoing assisted reproductive technology. Int J Environ Res Public Health. 2021; 18.
25. Mei J, Wang H, Lu S, Zhang YZ, Chen YM, Zhang W, Yin YX, Mao AF. Treatment effect of active folate on adverse pregnancy. Chin J Woman Child Health Res. 2017; 28.
26. Zhou L, Gao X, Wu Y, Zhang Z. Analysis of pregnancy outcomes for survivors of the vanishing twin syndrome after *in vitro* fertilization and embryo transfer. Eur J Obstet Gynecol Reprod Biol. 2016; 203:35-39.
27. Sacha CR, Basnet K, Lee AM, James K, Roberts DJ. Advanced maternal age may impact placental morphology in IVF pregnancies. Fertil Steril. 2018; 109:E48.
28. Dong Y, Wang L, Lu Y, Fu Z, Du Y, Wang L. Factors affecting mode of delivery in women of advanced maternal age. Biosci Trends. 2021; 15:61-63.
29. Liu N, Hu Q, Liao H, Wang X, Yu H. Vasa previa: Perinatal outcomes in singleton and multiple pregnancies. Biosci Trends. 2021; 15:118-125.
30. Zaadstra BM, Seidell JC, Van Noord PA, te Velde ER, Habbema JD, Vrieswijk B, Karbaat J. Fat and female fecundity: Prospective study of effect of body fat distribution on conception rates. BMJ. 1993; 306:484-487.
31. Zhu L. Polymorphisms in the methylene tetrahydrofolate reductase and methionine synthase reductase genes and their correlation with unexplained recurrent spontaneous abortion susceptibility. Genet Mol Res. 2015; 14:8500-8508.
32. Yang Y, Luo Y, Yuan J, Tang Y, Xiong L, Xu M, Rao X, Liu H. Association between maternal, fetal and paternal *MTHFR* gene C677T and A1298C polymorphisms and risk of recurrent pregnancy loss: A comprehensive evaluation. Arch Gynecol Obstet. 2016; 293:1197-1211.
33. Hwang IW, Kang YD, Kwon BN, Hong JH, Han SH, Kim JS, Park JW, Jin HJ. Genetic variations of *MTHFR* gene and their association with preterm birth in Korean women. Medicina (Kaunas). 2017; 53:380-385.
34. Forges T, Monnier-Barbarino P, Alberto JM, Guéant-Rodriguez RM, Daval JL, Guéant JL. Impact of folate and homocysteine metabolism on human reproductive health. Hum Reprod Update. 2007; 13:225-238.
35. Mishra J, Tomar A, Puri M, Jain A, Saraswathy KN. Trends of folate, vitamin B12, and homocysteine levels in different trimesters of pregnancy and pregnancy outcomes. Am J Hum Biol. 2020; 32:e23388.
36. Rosario FJ, Nathanielsz PW, Powell TL, Jansson T. Maternal folate deficiency causes inhibition of mTOR signaling, down-regulation of placental amino acid transporters and fetal growth restriction in mice. Sci Rep. 2017; 7:3982.
37. Ahmed T, Fellus I, Gaudet J, MacFarlane AJ, Fontaine-Bisson B, Bainbridge SA. Effect of folic acid on human trophoblast health and function *in vitro*. Placenta. 2016; 37:7-15.
38. Li Y, Gao R, Liu X, Chen X, Liao X, Geng Y, Ding Y, Wang Y, He J. Folate deficiency could restrain decidual angiogenesis in pregnant mice. Nutrients. 2015; 7:6425-6445.
39. Martí-Carvajal A, Peña-Martí G, Comunián-Carrasco G, Muñoz-Navarro S, Luco M, Martí-Peña A, Medina-Laurentín C. Prematurity and maternal folate deficiency: Anemia during pregnancy study group results in Valencia, Venezuela. Arch Latinoam Nutr. 2004; 54:45-49.
40. George L, Mills JL, Johansson AL, Nordmark A, Olander B, Granath F, Cnattingius S. Plasma folate levels and risk of spontaneous abortion. Jama. 2002; 288:1867-1873.
41. Ferrazzi E, Tiso G, Di Martino D. Folic acid versus 5-methyl tetrahydrofolate supplementation in pregnancy. Eur J Obstet Gynecol Reprod Biol. 2020; 253:312-319.
42. Kaye AD, Jeha GM, Pham AD, Fuller MC, Lerner ZI, Sibley GT, Cornett EM, Urits I, Viswanath O, Kevil CG. Folic acid supplementation in patients with elevated homocysteine levels. Adv Ther. 2020; 37:4149-4164.
43. Obeid R, Holzgreve W, Pietrzik K. Is 5-methyltetrahydrofolate an alternative to folic acid for the prevention of neural tube defects? J Perinat Med. 2013; 41:469-483.
44. Hekmatdoost A, Vahid F, Yari Z, Sadeghi M, Eini-Zinab H, Lakpour N, Arefi S. Methyltetrahydrofolate *vs* folic acid supplementation in idiopathic recurrent miscarriage with respect to methylenetetrahydrofolate reductase C677T and A1298C polymorphisms: A randomized controlled trial. PLoS One. 2015; 10:e0143569.
45. Lamers Y, Prinz-Langenohl R, Moser R, Pietrzik K. Supplementation with [6S]-5-methyltetrahydrofolate or folic acid equally reduces plasma total homocysteine concentrations in healthy women. Am J Clin Nutr. 2004; 79:473-478.

Received July 25, 2021; Revised April 18, 2022; Accepted May 31, 2022.

[§]These authors contributed equally to this work.
**Address correspondence to:*
Ling Wang, Laboratory for Reproductive Immunology, Obstetrics and Gynecology Hospital of Fudan University, 419 Fangxie Road, Shanghai 200011, China.
E-mail: Dr.wangling@fudan.edu.cn

Yan Du, Laboratory for Reproductive Immunology, Obstetrics and Gynecology Hospital of Fudan University, 419 Fangxie Road, Shanghai 200011, China.
E-mail: sophiedu_61@163.com

Released online in J-STAGE as advance publication June 10, 2022.

Original Article

DOI: 10.5582/bst.2022.01116

The preventive effect of loganin on oxidative stress-induced cellular damage in human keratinocyte HaCaT cells

Cheol Park[1], Hyesook Lee[2], Soojung Jin[3], Jung-Ha Park[3,4], Min Ho Han[5], Jin-Woo Jeong[6], Hyun Ju Kwon[3,4], Byung Woo Kim[3,4], Shin-Hyung Park[7], Su Hyun Hong[8,9], Gi-Young Kim[10], Yung Hyun Choi[3,8,9,*]

[1] Division of Basic Sciences, College of Liberal Studies, Dong-eui University, Busan, Korea;
[2] Department of Convergence Medicine, Pusan National University School of Medicine, Yangsan, Korea;
[3] Core-Facility Center for Tissue Regeneration, Dong-eui University, Busan, Korea;
[4] Biopharmaceutical Engineering Major, Division of Applied Bioengineering, College of Engineering, Dong-eui University, Busan, Korea;
[5] National Marine Biodiversity Institute of Korea, Seocheon, Korea;
[6] Nakdonggang National Institute of Biological Resources, Sangju, Korea;
[7] Department of Pathology, Dong-eui University College of Korean Medicine, Busan, Korea;
[8] Anti-Aging Research Center, Dong-eui University, Busan, Korea;
[9] Department of Biochemistry, Dong-eui University College of Korean Medicine, Busan, Korea;
[10] Department of Marine Life Science, Jeju National University, Jeju, Korea.

SUMMARY Loganin is a type of iridoid glycosides isolated from Corni fructus and is known to have various pharmacological properties, but studies on its antioxidant activity are still lacking. Therefore, in this study, the preventive effect of loganin on oxidative stress-mediated cellular damage in human keratinocyte HaCaT cells was investigated. Our results show that loganin pretreatment in a non-toxic concentration range significantly improved cell survival in hydrogen peroxide (H_2O_2)-treated HaCaT cells, which was associated with inhibition of cell cycle arrest at the G2/M phase and induction of apoptosis. H_2O_2-induced DNA damage and reactive oxygen species (ROS) generation were also greatly reduced in the presence of loganin. Moreover, H_2O_2 treatment enhanced the cytoplasmic release of cytochrome *c*, upregulation of the Bax/Bcl-2 ratio and degradation of cleavage of poly (ADP-ribose) polymerase, whereas loganin remarkably suppressed these changes. In addition, loganin obviously attenuated H_2O_2-induced autophagy while inhibiting the increased accumulation of autophagosome proteins, including as microtubule-associated protein 1 light chain 3-II and Beclin-1, and p62, an autophagy substrate protein, in H_2O_2-treated cells. In conclusion, our current results suggests that loganin could protect HaCaT keratinocytes from H_2O_2-induced cellular injury by inhibiting mitochondrial dysfunction, autophagy and apoptosis. This finding indicates the applicability of loganin in the prevention and treatment of skin diseases caused by oxidative damage.

Keywords Loganin, ROS, DNA damage, apoptosis, autophagy

1. Introduction

Corni fructus, a fruit of *Cornus officinalis* Sieb. et Zucc. belonging to the Cornaceae family, has been widely used in East Asia including Korea for the purpose of tonifying the kidneys and liver (*1-3*). Secondary metabolites, including iridoids, are abundantly present in Corni fructus, and studies on the various pharmacological effects of these substances are increasing (*3-5*). Among them, loganin is an iridoid glycoside compound found and has been reported to have various beneficial effects, including anti-inflammatory, neuroprotective, inhibiting cartilage degeneration and osteoarthritis, renal protection and improving intestinal function (*6-12*). These pharmacological activities of loganin are believed to be at least related to its antioxidant effect. For example, loganin protected against hydrogen peroxide (H_2O_2) and amyloid-β-induced neurotoxicity while inhibiting the production of reactive oxygen species (ROS) (*13,14*), suggesting that its antioxidant effect was closely associated with ROS scavenging activity. In addition, this compound suppressed diabetes mellitus-induced reproductive damage by restoring glutathione level and superoxide dismutase activity, as well as reducing

ROS level (*15*). Recently, Wen *et al*. (*9*) reported that loganin reduced burn-induced intestinal inflammation and oxidative stress, and Cheng *et al*. (*16*) found that inhibition of NLRP3 inflammasome activation by the antioxidant activity of loganin contributed to the blockade of Schwann cell pyroptosis. Moreover, Xu *et al*. (*12*) have been reported that the antioxidant activity of loganin contributes to neuronal survival by inhibiting autophagy and mitochondrial division. Similar to these results, we also demonstrated that loganin may be a substance capable of preventing inflammatory and oxidative damage in lipopolysaccharide-stimulated macrophages (*17*).

Although ROS play an important role as a second messenger during normal cellular metabolism, excessive production of ROS results in progressive oxidative damage to organelles [18, 19]. In particular, ROS act as regulators of body homeostasis, including epidermal keratinocyte proliferation, exacerbating skin aging and has been implicated in various skin diseases (*20,21*). As in other tissues, oxidative stress caused by excessive accumulation of ROS in keratinocytes ultimately induces depolarization of the mitochondrial membrane potential (MMP, *Δψm*), a hallmark of mitochondrial dysfunction. Subsequently, cytochrome *c* is released from the mitochondria into the cytoplasm, which activates the caspase cascade and ultimately induces apoptosis (*22,23*). More recently, Liu *et al*. (*24*) suggested that catalpol, a type of natural iridoid glucoside, may have therapeutic properties for psoriasis by ameliorating oxidative stress in tumor necrosis factor-α-stimulated keratinocytes. In addition, natural iridoid glucoside derivatives such as geniposide and aucubin have been reported to have protective effects on oxidative stress induced by ultraviolet-B irradiation in human skin fibroblasts (*25,26*). However, since the beneficial effect of loganin on epidermal keratinocytes has not been clearly elucidated, in this study, the protective potential of loganin against H_2O_2-induced oxidative stress in human keratinocyte HaCaT cells was investigated.

2. Materials and Methods

2.1. Cell culture and treatment

HaCaT keratinocytes purchased from the American Type Culture Collection (CRL-1458™, Manassas, VA, USA) were cultured in Dulbecco's modified Eagle's medium containing 10% fetal bovine serum and 1% antibiotics at 37°C and 5% CO_2. All materials needed for cell culture were obtained from WelGENE Inc. (Gyungsan, Korea). Loganin and H_2O_2 (Sigma-Aldrich Chemical Co., St. Louis, MO, USA) were dissolved in dimethyl sulfoxide (Thermo Fisher Scientific, Waltham, MA, USA) and distilled water to prepare stock solutions of 100 mM each. The stock solutions were diluted in the medium before utilization.

2.2. Cell viability

A 3-(4,5-dimethylthiazol-2-yl)-2,5-diphenyltetrazolium bromide (MTT) assay is used to measure cell viability, as previously described (*27*). Briefly, HaCaT cells were stimulated with the different concentrations of loganin or H_2O_2 alone for 24 h, or exposed to loganin for 1 h and then treated with H_2O_2 for 24 h. At the end time, the MTT reaction was run and absorbance was measured with a microplate reader (Beckman Coulter Inc., Brea, CA, USA) at the Core Facility Center for Tissue Regeneration (Dong-eui University, Busan, Korea). Images of cell morphological changes were captured using an inverted microscope (Carl Zeiss, Oberkochen, Germany).

2.3. Cell cycle analysis

For cell cycle analysis of H_2O_2-treated or untreated cells with and without loganin for 24 h, both adherent and detached cells were washed with phosphate-buffered saline (PBS) and then fixed by ethanol, as previously described (*28*). After that, cells were exposed with RNAase and propidium iodide (PI) (Thermo Fisher Scientific, Waltham, MA, USA) for 20 min at 4°C. Cell cycle distributions were calculated after appropriate gating of cell populations using flow cytometry (Becton Dickinson, San Jose, CA, USA).

2.4. Apoptosis analysis

To observe whether apoptosis was induced, flow cytometry was performed according to a published method (*29*). Briefly, cells were stimulated with H_2O_2 for 24 h with or without loganin, washed with PBS and then fixed with 4% paraformaldehyde solution for 15 min. Subsequently, cells were stained with annexin V-fluorescein isothiocyanate (FITC)/propidium iodide (PI) (Becton Dickinson), and annexin V-positive cells were quantified as cells induced by apoptosis using a flow cytometer.

2.5. Analysis of intracellular ROS

To measure the levels of ROS, the collected cells were stained with 2',7'-dichlorofluorescein diacetate (DCF-DA) dye (Sigma-Aldrich Chemical Co.). In brief, treated cells were collected and preloaded with 10 μM DCF-DA for 20 min at 37°C in the dark. The fluorescence intensity was observed under a fluorescence microscope as previously described (*30*). In parallel, ROS generation was quantified using flow cytometry (*31*). N-acetyl-L-cysteine (NAC, Sigma-Aldrich Chemical Co.) was used as a positive control as a scavenger of ROS.

2.6. Comet assay

A comet assay® kit obtained from Trevigen, Inc.

(Gaithersburg, MD, USA) was used to evaluate DNA damage according to the manufacturer's kit protocols (*32*). The localized green fluorescence of apoptotic cells was detected using fluorescent microscope (Leica, Wetzlar, Germany). The stained cells were imaged using a fluorescence microscope.

2.7. Immunofluorescence assay for detection of phospho (p)-γH2AX

To observe intracellular expression of p-γH2AX, a marker of DNA strand breakage (*30*), cells grown on 4-well chamber slide were stimulated with or without loganin for 1 h and then treated with H_2O_2 for additional 24 h. After fixing with 4% paraformaldehyde solution at room temperature (RT) for 20 min, cells were incubated with ice-cold PBS containing 1% bovine serum albumin (Sigma-Aldrich Chemical Co.) and 1% Triton X-100 (Sigma-Aldrich Chemical Co.) for 1 h. Subsequently, immunostaining was performed using an antibody against p-γH2AX (Abcam, Inc., Cambridge, UK) at 4°C overnight and then reacted with Alexa Fluor® 647-conjugated secondary antibody (Abcam, Inc.) for 1 h at RT. Additionally, nuclei were also stained with 4′,6′-diamidino-2-phenylindole (DAPI) solution (Thermo Fisher Scientific) for 20 min at RT. The cells were immediately observed under a fluorescence microscope (Carl Zeiss).

2.8. Western blotting for protein expression analysis

Whole cell lysates for immunoblotting were prepared according to a previous method (*33*). To isolate the cytoplasmic and mitochondrial fractions, a mitochondrial/cytoplasmic fractionation kit (Active Motif, Inc., Carlsbad, CA, USA) was used. For Western blot analysis, the same amount of protein for each treatment group was separated by sodium dodecyl sulfate-polyacrylamide gel electrophoresis and transferred to polyvinylidene difluoride membranes, and then the primary antibodies purchased from Santa Cruz Biotechnology, Inc. (Santa Cruz, CA, USA), Abcam, Inc.), Thermo Fisher Scientific and Cell Signaling Technology (Danvers, MA, USA) were probed, as previously described (*34*). Subsequently, the membranes that had finished reacting with the primary antibodies reacted with the correlated secondary antibodies (Santa Cruz Biotechnology, Inc.). The membranes were then exposed enhanced chemiluminescence solution (Thermo Fisher Scientific) and visualized using a Fusion FX Imaging System (Vilber Lourmat, Torcy, France). Band intensities were quantified and normalized to a loading control by densitometry using ImageJ® software (v1.48, National Institutes of Health, Bethesda, MD, USA).

2.9. MMP assay

To measure MMP, the cells were stained with 5,5',6,6'-tetrachloro-1,1',3,3'-tetraethylimidacarbocyanine iodide (JC-1, Thermo Fisher Scientific) reagent according to the previous methods (*35,36*), and quantitative analysis was performed using a flow cytometer, and fluorescence images were taken with a fluorescence microscope.

2.10. Autophagic activity detection

To evaluate the occurrence of autophagy, the Cyto-ID® Autophagy Detection Kit (Enzo Life Sciences Inc, Farmingdale, NY, USA) was employed according to the manufacturer's instructions. In brief, the treated cells were collected, suspended, stained with the Cyto-ID staining solution provided in the kit at RT temperature in the dark, and then autophagy-induced cells were quantitatively analyzed using flow cytometry (*36*). In parallel with this, DAPI staining was used to counterstain the nuclei, and localized green fluorescence of autophagic cells was detected under a fluorescence microscope (*30*).

2.11. Statistical analysis

All experiments were independently repeated at least 3 times to determine significance. Results were presented as mean and standard deviation (SD) using SPSS 25.0 (SPSS Inc., Chicago, IL, USA), and differences ($p < 0.05$) were considered statistically using ANOVA-Tukey's post-hoc test.

3. Results

3.1. Loganin prevented the loss of HaCaT cell viability caused by H_2O_2 treatment

As indicated in Figure 1A, loganin has been no cytotoxicity up to 12.5 μM of concentration in HaCaT cells. However, cells exposed to 15 μM loganin showed a slight inhibition in cell viability. Therefore, 12.5 μM was selected the maximum concentration of loganin to establish its efficacy, we performed further experiments. The cell viability in HaCaT cells treated with 500 μM H_2O_2 was significantly reduced to approximately 60% compared that in the untreated control cells (Figure 1B). However, pretreatment of loganin significantly inhibited H_2O_2-induced reduction of cell viability in a concentration-dependent manner (Figure 1C). Especially, exposure to NAC as a positive control restored cell viability that could control the level of H_2O_2-stimulated cells. In addition, morphological alterations such as cell shrinkage and cytoplasm vacuolization were observed in H_2O_2-treated cells, but not in the presence of loganin (Figure 1D).

3.2. Loganin restored cell cycle arrest and apoptotic cell death in H_2O_2-treated HaCaT cells

As shown in Figure 2A, the population of cells belonging to the G2/M phase in H_2O_2-treated HaCaT cells was significantly increased compared to the untreated control group, which was attenuated by loganin pretreatment. The proportion of cells with sub-G1 DNA content, which indicates the frequency of apoptosis, also greatly increased after H_2O_2 treatment compared with control cells, which significantly diminished by pretreatment of loganin (Figure 2A and 2B). In addition, the population of annexin V-positive cells was also significantly increased in H_2O_2-treated HaCaT cells (Figure 2C and 2D), which was markedly suppressed by loganin pretreatment. The results indicate that, similar to the NAC pretreatment group, loganin substantially attenuated cell cycle arrest and apoptotic cell death following by H_2O_2, thereby restoring cell viability.

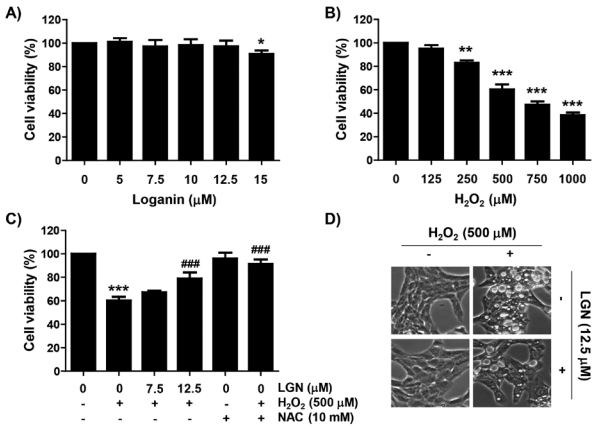

Figure 1. Inhibitory effects of loganin on H_2O_2-mediated cytotoxicity in HaCaT cells. Cells were treated with different concentrations of loganin (LGN) or H_2O_2 for 24 h **(A** and **B)** or treated the indicated concentrations of loganin or NAC (10 mM) for 1 h, and then stimulated with H_2O_2 for 24 h **(C** and **D)**. **(A-C)** The results of quantitative analysis of cell viability according to MTT assay were presented. The data were represented as mean ± SD of three independent experiments. Significant differences compared to the control cells ($^{*}p < 0.05$, $^{**}p < 0.01$ and $^{***}p < 0.001$) or H_2O_2-treated cells ($^{\#\#\#}p < 0.001$) were shown. **(D)** Representative cell morphologies observed under an inverted microscope are presented.

3.3. Loganin inhibited ROS production in H_2O_2-stimulated HaCaT cells

The results of flow cytometry after DCF-DA staining showed that the level of intracellular ROS production was markedly increased in H_2O_2-exposed HaCaT cells (Figure 3A and 3B). Consistent with this result, the DCF-fluorescence image in H_2O_2-treated cells was markedly increased compared to that of control cells (Figure 3C). However, similar to NAC pretreatment, loganin significantly decreased H_2O_2-induced ROS generation, indicating that the inhibitory effect of loganin on the cytotoxicity of H_2O_2 in HaCaT cells was related to its antioxidant activity.

3.4. Loganin suppressed DNA damage in H_2O_2-treated HaCaT cells

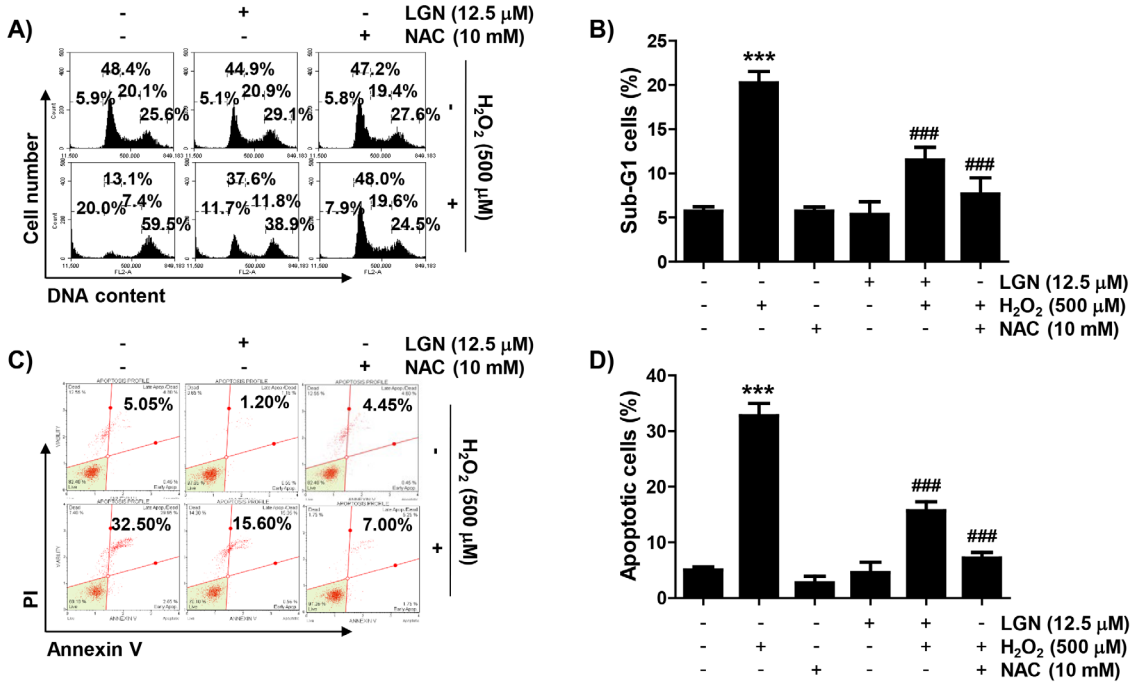

Figure 2. Attenuation of cell cycle arrest and apoptosis by loganin in H_2O_2-treated HaCaT cells. Cells were incubated in medium containing loganin (12.5 μM) or NAC (10 mM) for 1 h, and then exposed to H_2O_2 (500 μM) for 24 h. **(A** and **B)** Cells were collected and analysis of cell cycle distribution was performed. **(A)** Representative flow histograms were presented. **(B)** The frequency of sub-G1 cells were presented. **(C** and **D)** Cells were stained with annexin V-FITC/PI, and analyzed by flow cytometry. **(C)** The population of apoptotic cells were shown in the upper right panel of representative histograms. **(D)** The averages of the frequencies of apoptotic cells were presented. **(B** and **D)** The data were represented as mean ± SD of three independent experiments. Significant differences compared to the control cells ($^{***}p < 0.001$) or H_2O_2-treated cells ($^{\#\#\#}p < 0.001$) were shown.

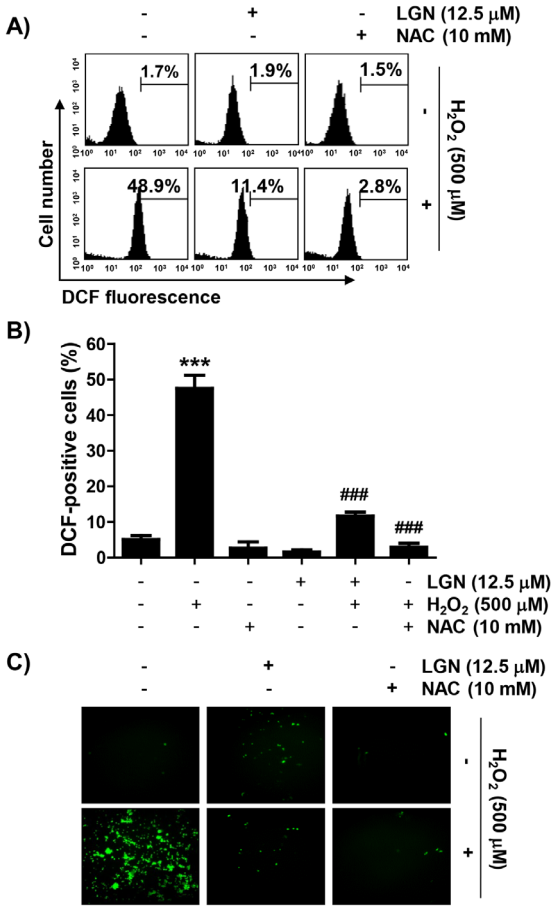

Figure 3. Inhibitory effects of loganin on ROS generated by H_2O_2 in HaCaT cells. Cells were cultured in medium containing loganin (12.5 μM) or NAC (10 mM) for 1 h, treated with H_2O_2 (500 μM) for 1 h and stained with DCF-DA. **(A** and **B)** Intracellular ROS levels were calculated using a flow cytometer **(A** and **B)** or observed under a fluorescence microscope **(C)**. **(B)** Significant differences compared to the control cells ($^{***}p < 0.001$) or H_2O_2-treated cells ($^{###}p < 0.001$) were shown.

Next, we investigated the inhibitory effect of loganin on DNA damage induced by H_2O_2-treatment. According to the comet assay results, DNA tails caused by damaged DNA fragments were markedly enhanced in H_2O_2-treated HaCaT cells (Figure 4A). However, these tails were markedly reduced in cells pretreated with loganin and NAC. Immunofluorescence indicated that H_2O_2 significantly increased the number of p-γH2AX positive-stained nuclei compared to control cells (Figure 4B). In addition, the expression of p-γH2A.X protein was strongly enhanced in H_2O_2-treated cells (Figure 4C and 4D). However, its expression was attenuated by loganin pretreatment, indicating that the inhibitory effect of loganin against H_2O_2-induced DNA damage was related to inhibition of ROS generation.

3.5. Loganin alleviated the change of apoptosis regulators expression in H_2O_2-treated HaCaT cells

As indicated in Figure 5A and 5B, the protein level of Bax was up-regulated in H_2O_2-treated HaCaT cells, while that of Bcl-2 was down-regulated. In addition, H_2O_2 enhanced the degradation of poly (ADP-ribose) polymerase (PARP). Furthermore, the level of cytochrome *c* expression in the mitochondria of cells treated with H_2O_2 was decreased, but its expression in the cytoplasm was increased (Figure 5C and 5D), which was associated with loss of MMP (Figure 5E and 5F). However, H_2O_2-induced these alterations were remarkably suppressed with loganin pretreatment, indicating that loganin protected HaCaT cells from apoptosis by blocking mitochondrial damage caused by H_2O_2.

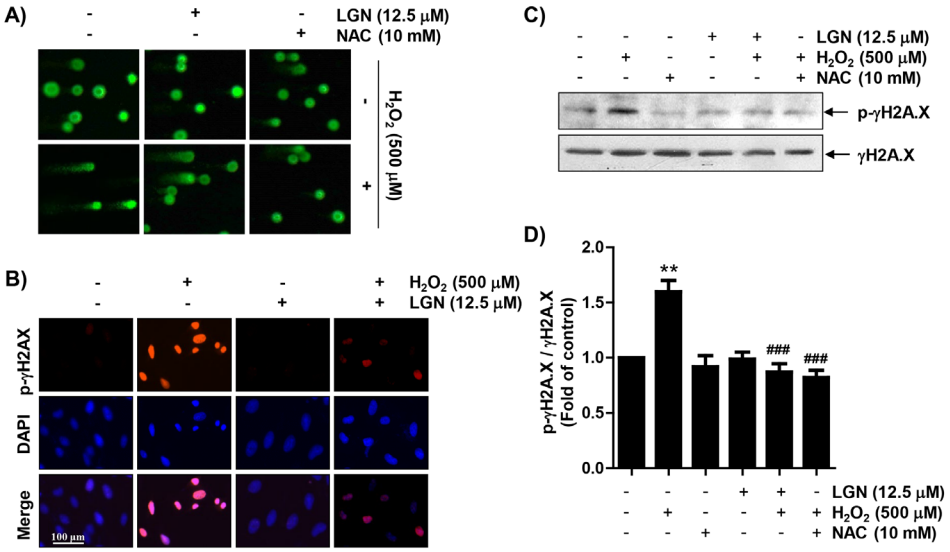

Figure 4. Inhibition of DNA damage by loganin in H_2O_2-treated HaCaT cells. Cells were stimulated with loganin (12.5 μM) or NAC (10 mM) for 1 h, and then exposed to H_2O_2 (500 μM) for 24 h. **(A)** Representative images of comet assay were shown. **(B)** Cells exposed to the indicated treatments were labeled for p-γH2AX (red) and DAPI (blue), and representative immunofluorescence images are presented. **(C)** The protein expression of p-γH2AX was investigated using Western blotting. Actin was used as the reference. **(D)** The relative expression levels of p-γH2AX protein were quantified by densitometry. Significant differences compared to the control cells ($^{**}p < 0.01$) or H_2O_2-treated cells ($^{###}p < 0.001$) were shown.

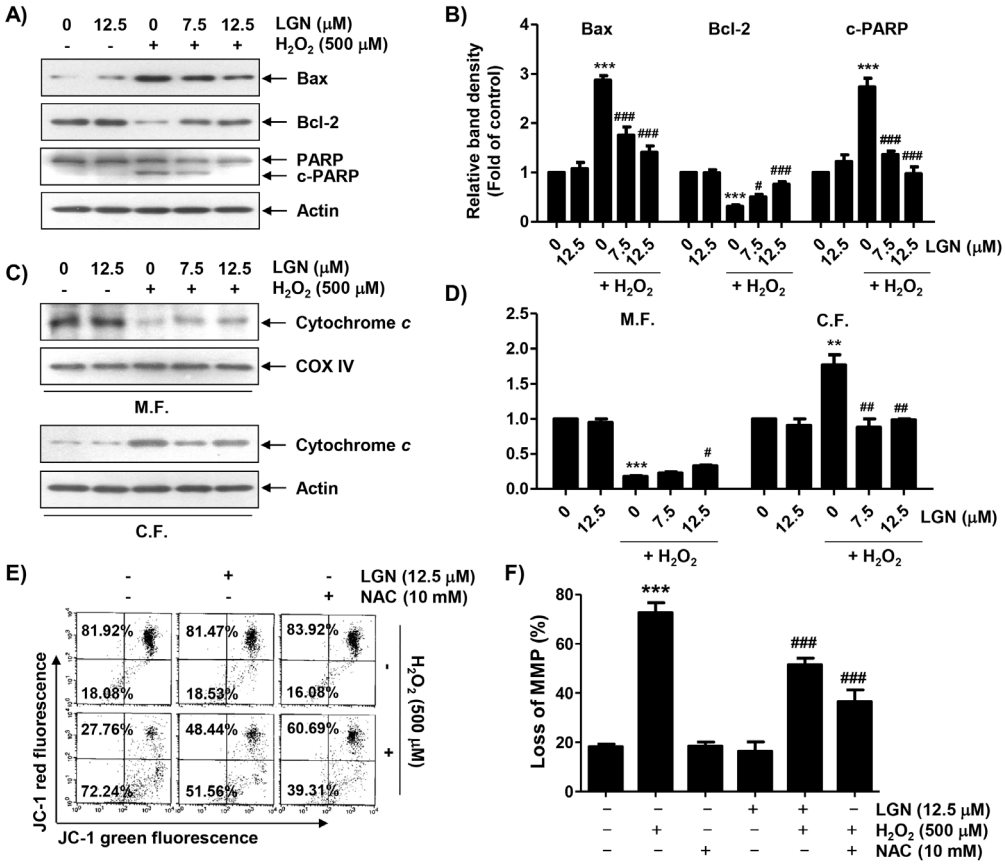

Figure 5. Inhibitory effect of loganin on changes of mitochondria-mediated apoptosis regulatory factors in H_2O_2-treated HaCaT cells. Cells were pretreated with loganin (12.5 μM) for 1 h, and then incubated with H_2O_2 (500 μM) for additional 24 h. **(A)** Protein expression of apoptosis-related mediators was investigated using total proteins. Actin was used as an internal standard. **(C)** Expression of cytochrome *c* in mitochondrial and cytoplasmic fractions was investigated. Actin and cytochrome *c* oxidase subunit IV (COX IV) were used as the reference genes for cytosolic and mitochondrial fractions (M.F., mitochondrial fraction; C.F., cytoplasmic fraction). **(B** and **D)** The relative expression levels of Bax, Bcl-2, c-PARP and cytochrome *c* protein were quantified by densitometry. **(E** and **F)** MMPs were examined by flow cytometry after JC-1 staining. **(E)** Representative profiles of flow cytometry analysis were presented. **(F)** Ratios of JC-1 aggregates to monomers were presented as mean ± SD of triplicate independent experiments. Significant differences compared to the control cells ($^{**}p < 0.01$ and $^{***}p < 0.001$) or H_2O_2-treated cells ($^{\#}p < 0.05$, $^{\#\#}p < 0.01$ and $^{\#\#\#}p < 0.001$) were shown.

3.6. Loganin attenuates H_2O_2-induced autophagy in HaCaT cells

Since the formation of autophagic vacuoles, which is typical of autophagy induction, was increased in H_2O_2-treated HaCaT cells (Figure 1D), we investigated whether autophagy was induced by H_2O_2 and whether loganin could inhibit it. The results of flow cytometry using Cyto-ID staining showed that autophagy was definitely induced in the cells treated with H_2O_2, as shown in Figure 6A and 6B, which was greatly reduced in the presence of loganin, and the same results were observed in the results of fluorescence microscopy (Figure 6C). Subsequently we detected autophagy biomarkers using Western blot analysis to confirm H_2O_2-induced autophagy, and found that H_2O_2 increased the accumulation of proteins such as microtubule-associated protein 1 light chain 3 (LC3)-II, beclin-1 and p62 (Figure 6D and 6E). However, their expression was obviously attenuated when loganin and H_2O_2 were treated together, suggesting that autophagy inhibition was implicated in the protection of HaCaT cells by loganin from oxidative damage caused by H_2O_2.

4. Discussion

In this study, we examined the efficacy of loganin on oxidative damage in H_2O_2-stimulated HaCaT keratinocytes. Our finding indicated that loganin significantly inhibited H_2O_2-induced cellular dysfunctions, including cell cycle arrest at the G2/M phase, DNA damage and apoptotic cell death, which was caused by blocking of ROS accumulation. Furthermore, we showed that the antioxidant potential of loganin was accompanied by inhibition of autophagy H_2O_2-treated HaCaT cells.

As is well known, H_2O_2, as oxidative stressor, induce cell cycle arrest at the G2/M phase in most cells, including keratinocytes, causing to DNA damage as well as cell death (*37-39*). In this study, reduction of cell survival in H_2O_2-treated HaCaT cells was accompanied by inhibition of cell cycle progression at the G2/M phase, which was in good agreement with the previous findings (*38,40*). However, these effects were significantly inhibited by loganin pretreatment. We also demonstrated that, in good agreement with previous studies (*9,13-17*),

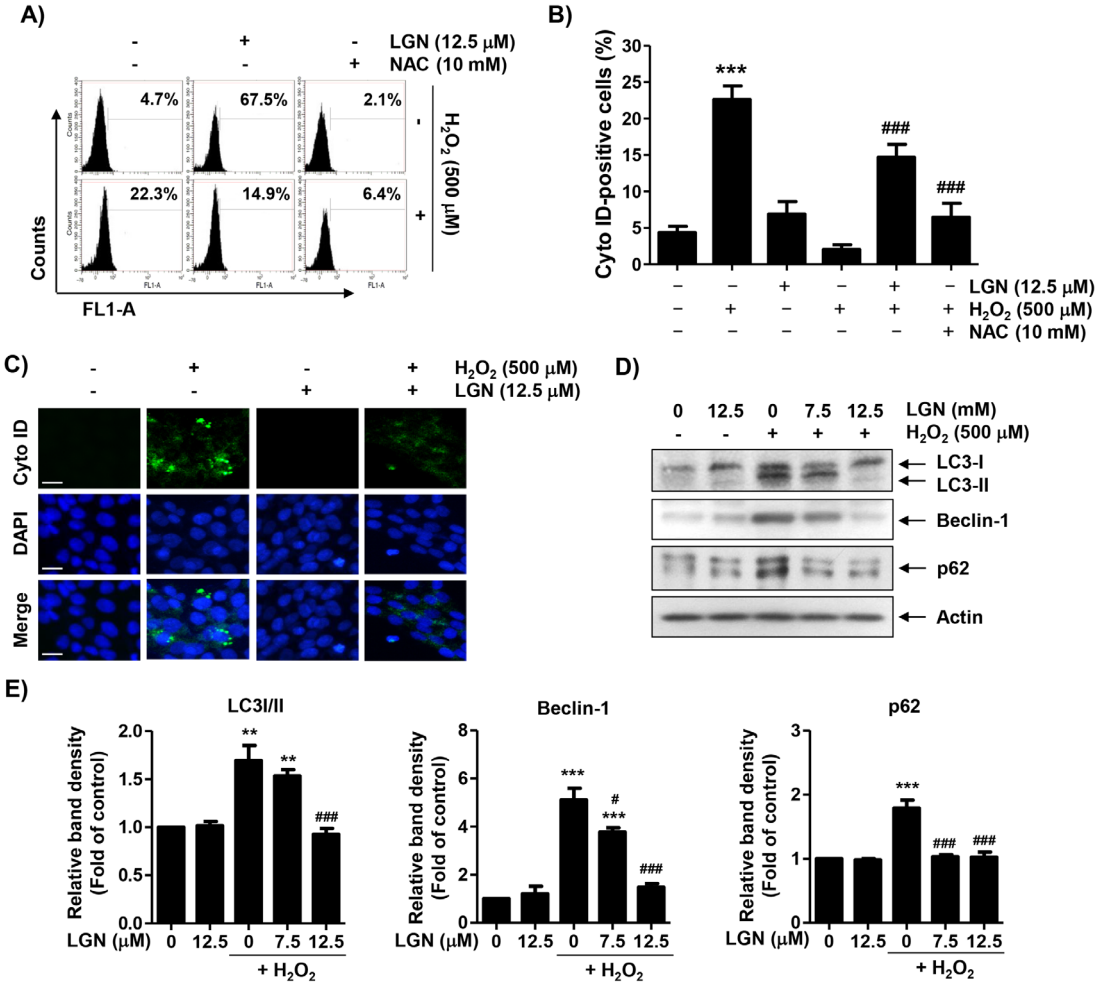

Figure 6. Protection of H_2O_2-induced autophagy by loganin in HaCaT cells. Cells were incubated with loganin (12.5 μM) or NAC (10 mM) for 1 h, and then incubated with H_2O_2 (500 μM) for additional 24 h. **(A** and **B)** Cells were stained with Cyto-ID, and analyzed by flow cytometry. **(A)** The frequency of autophagic cells were shown in the upper right panel of representative histograms. **(B)** The averages of the frequencies of autophagic cells were presented. **(C)** Cells were labeled for Cyto-ID (green) and DAPI (blue), and representative immunofluorescence images are presented. **(D)** Protein expression of autophagy-regulatory proteins was determined using total proteins. Actin was used as an internal standard. **(E)** The relative expression levels of LC3, Beclin-1 and p62 protein were quantified by densitometry. Significant differences compared to the control cells ($^{**}p < 0.01$ and $^{***}p < 0.001$) or H_2O_2-treated cells ($^{\#}p < 0.05$, $^{\#\#}p < 0.01$ and $^{\#\#\#}p < 0.001$) were shown.

loganin had potent antioxidant activity by significantly inhibiting H_2O_2-induced ROS generation. Oxidative stress induces damage to intracellular macromolecules such as nucleic acids, contributing to DNA damage and apoptosis (*41,42*). The results of the comet assay, a commonly used method to measure DNA strand breaks (*43*), showed that loganin largely blocked H_2O_2-induced comet tail formation. Additionally, in the immunoblotting results for analyzing the phosphorylation level of γH2AX (p-γH2AX), which indicates that the DNA double-strand is broken by oxidative stress (*33*), enhanced expression of p-γH2AX by H_2O_2 was effectively suppressed in the presence of loganin. These findings demonstrated that loganin has a remarkable ameliorating effect for H_2O_2-triggered DNA damage in HaCaT keratinocytes.

According to the results of previous studies, H_2O_2-induced apoptosis in HaCaT cells was strongly correlated with the cytosolic release of apoptogenic factors, including cytochrome *c*, which is initiates the mitochondria-mediated intrinsic apoptosis pathway (*40,44,45*). Cytochrome *c* released into the cytoplasm following the loss of MMP activates effector caspases such as caspase-3 and -7 through the activation of caspase-9, which induce degradation of matrix proteins including PARP to terminate apoptosis (*46,47*). In this study, the expression of cytochrome *c* was up-regulated in the cytoplasm and the loss of MMP was increased in H_2O_2-treated cells, consistent with previous studies (*40,44*). However, the expression of cytochrome *c* in the cytoplasm and mitochondria and the level of MMP were maintained at control levels in loganin-pretreated cells, suggesting that mitochondrial integrity in H_2O_2-treated HaCaT cells was maintained in the presence of loganin. Subsequently, the increase of Bax/Bcl-2 ratio by H_2O_2 was also counteracted by loganin pretreatment, which was correlated with to suppressing the cleavage of PARP. Bcl-2 family members control the release of apoptogenic factors through regulation of mitochondrial membrane permeability (*46,47*). Therefore, it is presumed that the reduction of the Bax/Bcl-2 expression ratio by loganin

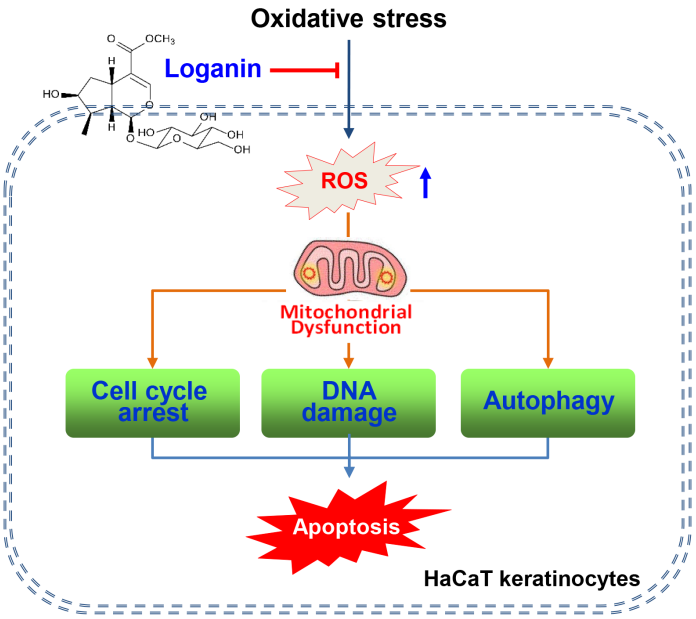

Figure 7. Schematic diagram representing the protective mechanism of loganin against oxidative damage in HaCaT cells.

plays a critical role in attenuating H_2O_2-induced HaCaT cell apoptosis. Based on this finding, we considered that loganin might be a potential antioxidant that prevents mitochondrial-dependent apoptosis as a scavenger of ROS. Our results agree very well with the results of Kwon *et al.* (*14*) on the blocking effect of loganin on the induction of apoptosis by H_2O_2 in SH-SY5Y neuronal cells.

Cellular damage, including DNA damage and apoptosis due to oxidative stress, is often accompanied by autophagy (*48,49*). In keratinocytes, it has also been reported that autophagy is involved in DNA damage and apoptosis caused by oxidative stress inducers (*50,51*), suggesting that ROS are potent and effective triggers of autophagy. Autophagy is a highly conserved self-digestion process for recycling cytoplasmic components such as unwanted protein aggregates and damaged organelles, which are sequestered into newly generated double-membraned structures called autophagosomes (*52,53*). Autophagosomes fuse sequentially with lysosomes and are eliminated through lysosomal degradation (*54,55*). Several important proteins are involved in this process, including LC3-II, Beclin-1 and p62. LC-3, an autophagosome membrane protein, controls key steps in the autophagic pathway, such as autophagic membrane growth and lysosome fusing, and the ratio LC3-II/LC3-I is commonly used to reflect autophagosome formation (*52,56*). Beclin-1 is involved in the initiation of autophagy by mediating the localization of autophagy proteins into the pre-autophagosomal membrane. In addition, Beclin-1 may be importantly involved in the regulation of apoptosis as well as autophagy because pro-autophagy properties may be reduced by Bcl-2 (*57,58*). p62 is another autophagosome-lysosomal membrane-associated protein that serves as an autophagic substrate (*59,60*). Therefore, these proteins are important markers of autophagy flux and critical regulators of autophagy regulation. The flow cytometry results of this study showed that the frequency of autophagosomes increased in H_2O_2-treated HaCaT cells, and the accumulation of LC-3, Beclin-1 and p62 was enhanced after H_2O_2 treatment, as determined by Western blotting. These observations support that autophagy as well as apoptosis are important mechanisms of H_2O_2-mediated cytotoxicity in HaCaT cells. And, in the presence of loganin, these autophagy markers were remarkably reversed compared to cells treated with H_2O_2 alone, showing that H_2O_2-induced HaCaT cell autophagy was clearly reduced by loganin supplementation. However, since autophagy has dual roles of pro-survival and pro-death depending on e circumstances, additional mechanistic studies are required on how the alleviated effect of loganin on H_2O_2-induced autophagy affects the survival of HaCaT cells.

In the current study, we evaluated the efficacy of loganin on H_2O_2-mediated oxidative damage in HaCaT keratinocytes. Our results revealed that loganin visibly diminished cell cycle arrest at the G2/M phase, DNA damage, autophagy and apoptosis in H_2O_2-stimulated HaCaT cells, which was linked to its ability to suppress ROS accumulation. Additionally, the anti-apoptotic effect by loganin was a result of blockade of mitochondrial dysfunction, which correlated with inhibition of cytoplasmic release of cytochrome *c* due to inhibition of increased Bax/Bcl-2 ratio (Figure 7). This study provides a theoretical basis for the inhibitory mechanism of oxidative stress-mediated cellular damage of loganin and its application as a novel therapeutic agent to counteract oxidative stress-mediated skin diseases.

Funding: This research was supported by the National Research Foundation of Korea grant (2021R1A2C200954911) and Korea Basic Science Institute grant (2020R1A6C101A201) funded by the Korea government (MSIT).

Conflict of Interest: The authors have no conflicts of interest to disclose.

References

1. Gao X, Liu Y, An Z, Ni J. Active components and pharmacological effects of *Cornus officinalis*: Literature review. Front Pharmacol. 2021; 12:633447.
2. Czerwińska ME, Melzig MF. *Cornus mas* and *Cornus officinalis* - Analogies and differences of two medicinal plants traditionally used. Front Pharmacol. 2018; 9:894.
3. Huang J, Zhang Y, Dong L, Gao Q, Yin L, Quan H, Chen R, Fu X, Lin D. Ethnopharmacology, phytochemistry, and pharmacology of *Cornus officinalis* Sieb. et Zucc. J Ethnopharmacol. 2018; 213:280-301.
4. Dinda B, Kyriakopoulos AM, Dinda S, Zoumpourlis V, Thomaidis NS, Velegraki A, Markopoulos C, Dinda M. *Cornus mas* L. (cornelian cherry), an important European and Asian traditional food and medicine: Ethnomedicine, phytochemistry and pharmacology for its commercial utilization in drug industry. J Ethnopharmacol. 2016; 193:670-690.
5. Dong Y, Feng ZL, Chen HB, Wang FS, Lu JH. Corni Fructus: A review of chemical constituents and pharmacological activities. Chin Med, 2018; 13:34.
6. Park E, Lee CG, Yun SH, Hwang S, Jeon H, Kim J, Yeo S, Jeong H, Yun SH, Jeong SY. Ameliorative effects of loganin on arthritis in chondrocytes and destabilization of the medial meniscus-induced animal model. Pharmaceuticals (Basel). 2021; 14:135.
7. Zhang J, Wang C, Kang K, Liu H, Liu X, Jia X, Yu K. Loganin attenuates septic acute renal injury with the participation of AKT and Nrf2/HO-1 signaling pathways. Drug Des Devel Ther. 2021; 15:501-513.
8. Choi N, Yang G, Jang JH, Kang HC, Cho YY, Lee HS, Lee JY. Loganin alleviates gout inflammation by suppressing NLRP3 inflammasome activation and mitochondrial damage. Molecules. 2021; 26:1071.
9. Wen H, Xing L, Sun K, Xiao C, Meng X, Yang J. Loganin attenuates intestinal injury in severely burned rats by regulating the toll-like receptor 4/NF-κB signaling pathway. Exp Ther Med. 2020; 20:591-598.
10. Hu J, Zhou J, Wu J, Chen Q, Du W, Fu F, Yu H, Yao S, Jin H, Tong P, Chen D, Wu C, Ruan H. Loganin ameliorates cartilage degeneration and osteoarthritis development in an osteoarthritis mouse model through inhibition of NF-κB activity and pyroptosis in chondrocytes. J Ethnopharmacol. 2020; 247:112261.
11. Yang Y, Gu Y, Zhao H, Zhang S. Loganin attenuates osteoarthritis in rats by inhibiting IL-1β-induced catabolism and apoptosis in chondrocytes *via* regulation of phosphatidylinositol 3-kinases (PI3K)/Akt. Med Sci Monit. 2019; 25:4159-4168.
12. Xu YD, Cui C, Sun MF, Zhu YL, Chu M, Shi YW, Lin SL, Yang XS, Shen YQ. Neuroprotective effects of loganin on MPTP-induced Parkinson's disease mice: Neurochemistry, glial reaction and autophagy studies. J Cell Biochem. 2017; 118:3495-3510.
13. Kim H, Youn K, Ahn MR, Kim OY, Jeong WS, Ho CT, Jun M. Neuroprotective effect of loganin against $A\beta_{25-35}$-induced injury *via* the NF-κB-dependent signaling pathway in PC12 cells. Food Funct. 2015; 6:1108-1116.
14. Kwon SH, Kim JA, Hong SI, Jung YH, Kim HC, Lee SY, Jang CG. Loganin protects against hydrogen peroxide-induced apoptosis by inhibiting phosphorylation of JNK, p38, and ERK 1/2 MAPKs in SH-SY5Y cells. Neurochem Int. 2011; 58:533-541.
15. Chen Y, Jiao N, Jiang M, Liu L, Zhu Y, Wu H, Chen J, Fu Y, Du Q, Xu H, Sun J. Loganin alleviates testicular damage and germ cell apoptosis induced by AGEs upon diabetes mellitus by suppressing the RAGE/p38MAPK/NF-κB pathway. J Cell Mol Med. 2020; 24:6083-6095.
16. Cheng YC, Chu LW, Chen JY, Hsieh SL, Chang YC, Dai ZK, Wu BN. Loganin attenuates high glucose-induced Schwann cells pyroptosis by inhibiting ROS generation and NLRP3 inflammasome activation. Cells. 2020; 23:1948.
17. Park C, Lee H, Kwon CY, Kim GY, Jeong JW, Kim SO, Choi SH, Jeong SJ, Noh JS, Choi YH. Loganin inhibits lipopolysaccharide-induced inflammation and oxidative response through the activation of the Nrf2/HO-1 signaling pathway in RAW264.7 macrophages. Biol Pharm Bull. 2021; 44:875-883.
18. Benhar M. Oxidants, antioxidants and thiol redox switches in the control of regulated cell death pathways. Antioxidants (Basel). 2020; 9:309.
19. He L, He T, Farrar S, Ji L, Liu T, Ma X. Antioxidants maintain cellular redox homeostasis by elimination of reactive oxygen species. Cell Physiol Biochem. 2017; 44:532-553.
20. Nakai K, Tsuruta D. What are reactive oxygen species, free radicals, and oxidative stress in skin diseases? Int J Mol Sci. 2021; 22:10799.
21. Birch-Machin MA, Bowman A. Oxidative stress and ageing. Br J Dermatol. 2016; 175:S26-29.
22. Paz ML, González Maglio DH, Weill FS, Bustamante J, Leoni J. Mitochondrial dysfunction and cellular stress progression after ultraviolet B irradiation in human keratinocytes. Photodermatol Photoimmunol Photomed. 2008; 24:115-122.
23. Rizwan H, Pal S, Sabnam S, Pal A. High glucose augments ROS generation regulates mitochondrial dysfunction and apoptosis *via* stress signalling cascades in keratinocytes. Life Sci. 2020; 241:117148.
24. Liu A, Zhang B, Zhao W, Tu Y, Wang Q, Li J. Catalpol ameliorates psoriasis-like phenotypes *via* SIRT1 mediated suppression of NF-κB and MAPKs signaling pathways. Bioengineered. 2021; 12:183-195.
25. Shin D, Lee S, Huang YH, Lim HW, Lee Y, Jang K, Cho Y, Park SJ, Kim DD, Lim CJ. Protective properties of geniposide against UV-B-induced photooxidative stress in human dermal fibroblasts. Pharm Biol. 2018; 56:176-182.
26. Ho JN, Lee YH, Park JS, Jun WJ, Kim HK, Hong BS, Shin DH, Cho HY. Protective effects of aucubin isolated from *Eucommia ulmoides* against UVB-induced oxidative stress in human skin fibroblasts. Biol Pharm Bull. 2005; 28:1244-1248.
27. Kim MY, Choi YW, Hwang HS. Regulatory effect on skin differentiation by mevastatin in psoriasis model using TNF-α and IL-17 induced HaCaT cells. Biotechnol Bioprocess Eng. 2021; 26:348-358.
28. Sim KH, Shu MS, Kim S, Kim JY, Choi BY, Lee YJ. Cilostazol induces apoptosis and inhibits proliferation of hepatocellular carcinoma cells by activating AMPK. Biotechnol Bioprocess Eng. 2021; 26:776-785.
29. Liu Z, Ouyang G, Lu W, Zhang H. Long non-coding RNA HOTAIR promotes hepatocellular carcinoma progression by regulating miR-526b-3p/DHX33 axis. Genes Genomics. 2021; 43:857-868.

30. Lee H, Kim DH, Kim JH, Park SK, Jeong JW, Kim MY, Hong SH, Song KS, Kim GY, Hyun JW, Choi YH. Urban aerosol particulate matter promotes necrosis and autophagy *via* reactive oxygen species-mediated cellular disorders that are accompanied by cell cycle arrest in retinal pigment epithelial cells. Antioxidants (Basel). 2021; 10:149.
31. Noh Y, Ahn JH, Lee JW, Hong J, Lee TK, Kim B, Kim SS, Won MH. Brain Factor-7® improves learning and memory deficits and attenuates ischemic brain damage by reduction of ROS generation in stroke *in vivo* and *in vitro*. Lab Anim Res. 2020; 36:24.
32. Volobaev VP, Serdyukova ES, Kalyuzhnaya EE, Schetnikova EA, Korotkova AD, Naik AA, Bach SN, Prosekov AY, Larionov AV. Investigation of the genotoxic effects of fluoride on a bone tissue model. Toxicol Res. 2020; 36:337-342.
33. Raavi V, Perumal V, Paul SFD. Potential application of γ-H2AX as a biodosimetry tool for radiation triage. Mutat Res Rev Mutat Res. 2021; 787:108350.
34. Choi MJ, Mukherjee S, Yun JW. Loss of ADAMTS15 promotes browning in 3T3-L1 white adipocytes *via* activation of β3-adrenergic receptor. Biotechnol Bioprocess Eng. 2021; 26:188-200.
35. Kim JH, Baek JI, Lee IK, Kim UK, Kim YR, Lee KY. Protective effect of berberine chloride against cisplatin-induced ototoxicity. Genes Genomics. 2022; 44:1-7.
36. Kim SY, Park C, Kim MY, Ji SY, Hwangbo H, Lee H, Hong SH, Han MH, Jeong JW, Kim GY, Son CG, Cheong J, Choi YH. ROS-mediated anti-tumor effect of Coptidis Rhizoma against human hepatocellular carcinoma Hep3B cells and xenografts. Int J Mol Sci. 2021; 22:4797.
37. Emmert H, Culley J, Brunton VG. Inhibition of cyclin-dependent kinase activity exacerbates H_2O_2-induced DNA damage in Kindler syndrome keratinocytes. Exp Dermatol. 2019; 28:1074-1078.
38. Thorn T, Gniadecki R, Petersen AB, Vicanova J, Wulf HC. Differences in activation of G2/M checkpoint in keratinocytes after genotoxic stress induced by hydrogen peroxide and ultraviolet A radiation. Free Radic Res. 2001; 35:405-416.
39. Panieri E, Gogvadze V, Norberg E, Venkatesh R, Orrenius S, Zhivotovsky B. Reactive oxygen species generated in different compartments induce cell death, survival, or senescence. Free Radic Biol Med. 2013; 57:176-187.
40. Park C, Lee H, Noh JS, Jin CY, Kim GY, Hyun JW, Leem SH, Choi YH. Hemistepsin A protects human keratinocytes against hydrogen peroxide-induced oxidative stress through activation of the Nrf2/HO-1 signaling pathway. Arch Biochem Biophys. 2020; 691:108512.
41. Brillo V, Chieregato L, Leanza L, Muccioli S, Costa R. Mitochondrial dynamics, ROS, and cell signaling: A blended overview. Life (Basel). 2021; 11:332.
42. Jiang Q, Yin J, Chen J, Ma X, Wu M, Liu G, Yao K, Tan B, Yin Y. Mitochondria-targeted antioxidants: A step towards disease treatment. Oxid Med Cell Longev. 2020; 2020:8837893.
43. Cordelli E, Bignami M, Pacchierotti F. Comet assay: A versatile but complex tool in genotoxicity testing. Toxicol Res (Camb). 2021; 10:68-78.
44. Park C, Cha HJ, Hong SH, Kim GY, Kim S, Kim HS, Kim BW, Jeon YJ, Choi YH. Protective effect of phloroglucinol on oxidative stress-induced DNA damage and apoptosis through activation of the Nrf2/HO-1 signaling pathway in HaCaT human keratinocytes. Mar Drugs. 2019; 17:225.
45. Shim JH, Kim KH, Cho YS, Choi HS, Song EY, Myung PK, Kang JS, Suh SK, Park SN, Yoon DY. Protective effect of oxidative stress in HaCaT keratinocytes expressing E7 oncogene. Amino Acids. 2008; 34:135-141.
46. Dadsena S, King LE, García-Sáez AJ. Apoptosis regulation at the mitochondria membrane level. Biochim Biophys Acta Biomembr. 2021; 1863:183716.
47. Xiong S, Mu T, Wang G, Jiang X. Mitochondria-mediated apoptosis in mammals. Protein Cell. 2014; 5:737-749.
48. Lyamzaev KG, Knorre DA, Chernyak BV. Mitoptosis, twenty years after. Biochemistry (Mosc). 2020; 85:1484-1498.
49. Kaminskyy VO, Zhivotovsky B. Free radicals in cross talk between autophagy and apoptosis. Antioxid Redox Signal. 2014; 21:86-102.
50. Fidrus E, Hegedűs C, Janka EA, Paragh G, Emri G, Remenyik É. Inhibitors of nucleotide excision repair decrease UVB-induced mutagenesis - An *in vitro* study. Int J Mol Sci. 2021; 22:1638.
51. Piao MJ, Ahn MJ, Kang KA, Ryu YS, Hyun YJ, Shilnikova K, Zhen AX, Jeong JW, Choi YH, Kang HK, Koh YS, Hyun JW. Particulate matter 2.5 damages skin cells by inducing oxidative stress, subcellular organelle dysfunction, and apoptosis. Arch Toxicol. 2018; 92:2077-2091.
52. Trelford CB, Di Guglielmo GM. Molecular mechanisms of mammalian autophagy. Biochem J. 2021; 478:3395-3421.
53. Condello M, Pellegrini E, Caraglia M, Meschini S. Targeting autophagy to overcome human diseases. Int J Mol Sci. 2019; 20:725.
54. Sánchez-Martín P, Komatsu M. Physiological stress response by selective autophagy. J Mol Biol. 2020; 432:53-62.
55. Zhao YG, Zhang H. Core autophagy genes and human diseases. Curr Opin Cell Biol. 2019; 61:117-125.
56. Xiang H, Zhang J, Lin C, Zhang L, Liu B, Ouyang L. Targeting autophagy-related protein kinases for potential therapeutic purpose. Acta Pharm Sin B. 2020; 10:569-581.
57. Tran S, Fairlie WD, Lee EF. BECLIN1: Protein structure, function and regulation. Cells. 2021; 10:1522.
58. Xu HD, Qin ZH. Beclin 1, Bcl-2 and autophagy. Adv Exp Med Biol. 2019; 1206:109-126.
59. Takahashi D, Arimoto H. Selective autophagy as the basis of autophagy-based degraders. Cell Chem Biol. 2021; 28:1061-1071.
60. Liu WJ, Ye L, Huang WF, Guo LJ, Xu ZG, Wu HL, Yang C, Liu HF. p62 links the autophagy pathway and the ubiqutin-proteasome system upon ubiquitinated protein degradation. Cell Mol Biol Lett. 2016; 21:29.

Received March 14, 2022; Revised March 29, 2022; Accepted May 31, 2022.

**Address correspondence to:*
Yung Hyun Choi, Department of Biochemistry, College of Korean Medicine, Dong-eui University, Busan 47227, Republic of Korea.
E-mail: choiyh@deu.ac.kr

Released online in J-STAGE as advance publication June 10, 2022.

Brief Report

DOI: 10.5582/bst.2022.01256

Real-time intraoperative near-infrared autofluorescence imaging to locate the parathyroid glands: A preliminary report

Bei Qian[§], Ximeng Zhang[§], Kaijian Bing, Longqing Hu, Xincai Qu, Tao Huang, Wei Shi[*], Shoupeng Zhang[*]

Department of Thyroid and Breast Surgery, Union Hospital, Tongji Medical College, Huazhong University of Science and Technology, Wuhan, Hubei, China.

SUMMARY Identification and localization of parathyroid glands (PGs) remains a challenge for surgeons. The aim of this study was to evaluate the efficiency of intraoperative near-infrared autofluorescence (NIRAF) imaging to detect PGs in thyroid and parathyroid diseases. Seventy-six patients undergoing surgery for thyroid or parathyroid diseases between July 9, 2020 and August 20, 2021 were retrospectively analyzed. Intraoperative carbon nanoparticle (CN) negative imaging and handheld NIRAF imaging were successively performed for each patient. Of 206 PGs that needed to be identified for surgery, 162 were identified by NIRAF imaging, with a theoretical rate of identification of 78.64%. This was higher than the rate of identification with CN negative imaging, which was 75.73%. The number of PGs identified by NIRAF imaging and CN negative imaging did not differ significantly in either total thyroidectomy or thyroid lobectomy. In addition, the autofluorescence (AF) intensity of secondary parathyroid adenoma was weaker than that of normal PGs. NIRAF imaging is potentially a more efficient tool for identification of PGs than CN negative imaging, with a shorter learning curve and lower risk. It may not be well-suited to secondary hyperthyroidism or adenoma, but it was more efficient at identifying excised specimens than visual identification by a surgeon.

Keywords parathyroid glands (PGs), near-infrared autofluorescence (NIRAF) imaging, carbon nanoparticles (CNs), identification, localization.

1. Introduction

With the increasing incidence of thyroid cancer (THCA) worldwide, thyroidectomy has become one of the most common endocrine surgeries (*1*). However, hypoparathyroidism caused by surgical injury remains a challenge for surgeons. The reported incidence of permanent hypoparathyroidism after total thyroidectomy is 0.5-6.6% and that of temporary hypoparathyroidism after thyroid surgery is 6.9-46% (*2,3*). Moreover, the risk of iatrogenic injury and inadvertent removal of parathyroid glands (PGs) increases with the extent of dissection or the complexity of the surgery (*4*). Tufano *et al*. reported that the incidence of permanent hypoparathyroidism following reoperative central compartment neck dissection can reach 9.5% (*5*).

Currently, conventional measures to reduce the risk of postoperative hypoparathyroidism mainly rely on visual recognition by a surgeon and preservation of PGs and their vascular pedicles, which are highly dependent on the surgeon's experience (*6*). However, PGs are very small and similar in color to adipose or connective tissue and even lymph nodes (LNs), and they are usually embedded within the surrounding tissue or behind the thyroid gland, so even experienced surgeons can unintentionally remove them at a rate as high as 9.1-15% (*1,7*). For surgeons with less experience or beginners in thyroid surgery, the incidence will be higher. Intraoperative frozen biopsy is the "gold standard" to confirm that the specimen removed is indeed a PG, but it involves considerable time and cost and may cause damage to the blood supply of PGs (*8*). Early studies suggested that injections of fluorescent agents such as methylene blue or indocyanine green (ICG) could aid in the intraoperative detection of PGs, but they have not been widely adopted (*9*). Moreover, these exogenous fluorophores were considered likely to lead to adverse reactions to the dye or injection (*10*).

In 2011, Paras *et al*. first reported that PGs emit autofluorescence (AF) when stimulated with a 785-nm wavelength laser (*11*). The fluorescence intensity of PGs is reported to be much greater than that of the

thyroid and all other surrounding tissue, with peak fluorescence occurring at 820 to 830 nm (*11*). Moreover, this technique does not rely on any exogenous drugs and dyes, thus avoiding possible adverse reactions. Since then, intraoperative near-infrared autofluorescence (NIRAF) imaging has been increasingly used to detect PGs. In addition, carbon nanoparticles (CNs) with an average diameter of 150 nm have also been found to be useful in identifying PGs, thanks to their high degree of lymphatic system tropism, tracing speed, rate of dyeing black, and a high color contrast with the surrounding tissue (*12*). However, the available data to evaluate and compare the effectiveness of the two methods in identifying PGs are still insufficient. The aim of the present study was to compare NIRAF imaging and CN negative imaging to evaluate the efficiency of NIRAF imaging in detecting PGs in thyroid and parathyroid diseases.

2. Patients and Methods

2.1. Study design

Subjects were 76 patients seen at the Thyroid and Breast Disease Center at Wuhan Union Hospital between July 9, 2020 and August 20, 2021. The inclusion criteria were: (1) age > 18 years; (2) no serious systemic disease; (3) patients underwent surgery; and (4) informed consent was provided. Patients who met any of the following criteria were excluded: (1) missing baseline information; (2) age ≤ 18 years; (3) having a severe systemic disease; or (4) lateral cervical LN metastasis. The data collected in this study included: patient ID, gender, age, the number of PGs that were detected by the two methods, the procedure undergone, and the postoperative histopathological diagnosis. Surgical procedures included total thyroidectomy with bilateral central lymph node dissection (CLND) and unilateral thyroid lobectomy with CLND or parathyroidectomy. Intraoperative CN negative imaging and handheld NIRAF imaging was successively performed for each patient.

2.2. Operative and imaging procedures

All of the surgeries were performed independently by two experienced thyroid surgeons. For the thyroid surgery, an incision parallel to a horizontal skin crease was made. The skin, subcutaneous tissue, adipose tissue, and platysma muscle were successively incised. A skin flap down to the superficial surface of the sternohyoid muscle was dissected upward to the thyroid cartilage and downward to the sternal notches, with the anterior jugular veins left in place (*13*). The midline raphe was identified and incised, and the sternohyoid and sternothyroid muscles were pulled laterally until the thyroid capsule was clearly identified. Care should be taken to keep the fibrous capsule of the thyroid gland intact, otherwise the injected CNs may leak out, contaminate the surgical field, and even cause infection. The lower third of the thyroid gland was exposed and 0.1 mL of CNs (in the form of an injected suspension at a concentration of about 50 mg per ml) were injected into the gland with a fine needle to a depth of about one third of the gland. Excessively dissected glands may cause damage to the surrounding lymphatic network, affecting the action of CNs after injection (*12*). The injected gland was gently massaged with gauze for about 1 minute and the surgeon waited for the gland to completely blacken. The thyroid gland was then mobilized to expose the central neck area. PGs were carefully identified by negative visualization while the LNs and thyroid gland were stained black, indicating positive visualization, and photographed intraoperatively. The operating room lights were subsequently turned off, and an infrared camera probe (Micro-intelligence Technology, Hunan, China) encapsulated in a sterile envelope was placed 20 cm away from the surgical field for near-infrared fluorescence imaging (NIFI) to detect the possible location of PGs (Figure 1). The numbers of PGs detected by the two approaches were recorded separately. The thyroid gland was subsequently removed and a rapid intraoperative pathological examination was performed. Based on the pathology results, the decision was made whether to perform a preventive CLND. For parathyroid surgery, thyroid exposure was achieved as described above. PGs were successively imaged with CN negative imaging and NIRAF imaging as described above. The diseased PGs were then removed and sent for a rapid intraoperative pathological examination.

2.3. Statistical analysis

Continuous variables with a normal distribution were expressed as the mean ± standard deviation (SD) or as the median and interquartile range (IQR). Categorical variables were expressed in terms of frequency and

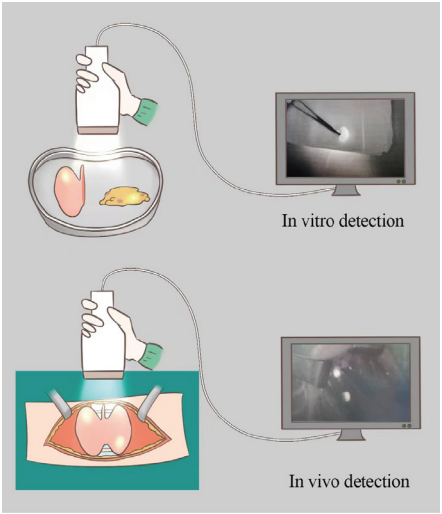

Figure 1. Diagram of NIRAF detection of parathyroid glands *in vivo* and *in vitro*.

percentages. A chi-square test was used to analyze categorical variables, while a *t*-test was used to compare continuous variables. Statistical significance was a two-sided $P < 0.05$. All statistical analyses were performed using R Studio version 4.0.3 (*http://www.r-project.org*).

2.4. Ethical approval and informed consent

The study was conducted in accordance with the ethical standards of the Declaration of Helsinki as well as national and international guidelines and approved by the Ethical Committee of the Union Hospital, Tongji Medical College of Huazhong University of Science and Technology (0304-01). Written consent for publication of patient data was obtained from the patients themselves.

3. Results and Discussion

3.1. Demographic characteristics and clinical features

During the period between July 9, 2020 and August 20, 2021, a total of 76 patients were identified and included in the present study. Table 1 summarizes the clinicopathological characteristics and treatment information of the patients. The mean age of all patients was 41.5 years (IQR: 32.8-50.5, range: 22-63). Twenty-seven patients (35.5%) were male and 49 (64.5%) were female. The final histopathological diagnosis for patients was THCA in 66 (86.8%), benign nodular goiter in 9 (11.8%) and parathyroid adenoma in 1 (1.3%). Of all patients, 25 (32.9%) underwent a total thyroidectomy plus CLND, 3 (3.9%) underwent a total thyroidectomy, 41 (53.9%) underwent a thyroid lobectomy plus CLND, 6 (7.9%) underwent a thyroid lobectomy, and 1 (1.3%) underwent a parathyroidectomy.

3.2. Rate of identification of PGs by the two approaches

According to the theoretical calculation of four PGs per patient, a total of 206 PGs (this number was calculated by procedure) were potentially identifiable in this study. However, 162 PGs were identified by NIRAF imaging, with a theoretical rate of identification of 78.64%. CN negative imaging identified 156 PGs, with a rate of 75.73%. Intraoperative images are shown in Figure 2. NIRAF imaging had a higher rate of identification than CN negative imaging, although the difference was not significant ($P = 0.481$). For total thyroidectomy, NIRAF imaging identified 3.2 PGs on average, while CN negative imaging identified 3.0 PGs. There were no significant differences in the number of PGs identified ($P = 0.457$). For thyroid lobectomy, an average of 1.6 PGs were identified by NIRAF imaging and 1.5 PGs were identified by CN negative imaging. There were no significant differences in the number of PGs identified (P=0.843). Table 2 shows the results of a statistical analysis. Interestingly, the AF intensity of a secondary parathyroid adenoma was weaker than that of a normal PG (Figure 3).

3.3. Discussion

To the extent known, this is the first study to provide data on evaluating the feasibility and efficiency of NIRAF imaging to detect PGs in real time during thyroid and parathyroid surgeries by comparing that modality to CN negative imaging. Results indicated that both NIRAF imaging and CN negative imaging identified PGs at an acceptable rate. The rate of PG identification did not differ significantly between NIRAF imaging and CN negative imaging in either total thyroidectomy or thyroid lobectomy, but NIRAF imaging was considered to have greater clinical value and potential for widespread use because of its convenience, safety, and reproducibility. Because of its simplicity and speed, NIRAF imaging had a shorter learning curve for beginners and less

Table 1. Demographics and clinicopathological characteristics of all patients

Parameters	All patients ($n = 76$)
Age, years (median [IQR])	41.5 (IQR: 32.8-50.5)
Gender, *n* (%)	
Male	27 (35.5%)
Female	49 (64.5%)
Histopathological diagnosis	
Thyroid cancer	66 (86.8%)
Benign nodular goiter	9 (11.8%)
Parathyroid adenoma	1 (1.3%)
Procedure, *n* (%)	
Total thyroidectomy plus CLND	25 (32.9%)
Total thyroidectomy	3 (3.9%)
Thyroid lobectomy plus CLND	41 (53.9%)
Thyroid lobectomy	6 (7.9%)
Parathyroidectomy	1 (1.3%)

IQR: interquartile range; CLND: central lymph node dissection.

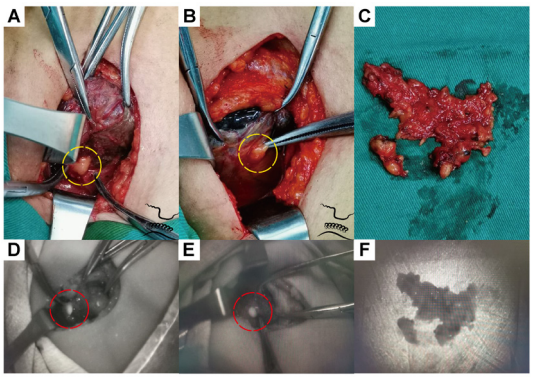

Figure 2. NIRAF imaging and CN negative imaging of the parathyroid glands during a thyroidectomy; the parathyroid glands are circled in red or yellow. (A) CN negative imaging of the upper right parathyroid gland; **(B)** CN negative imaging of the lower right parathyroid gland; **(C)** Visible light images of the isolated right central lymph node specimen; **(D)** NIRAF imaging of the upper right parathyroid gland; **(E)** NIRAF imaging of the lower right parathyroid gland; **(F)** NIRAF imaging of the isolated right central lymph node specimen.

Table 2. Accuracy of identification of 206 parathyroid glands by NIRAF imaging and CN negative imaging

Parameters	NIRAF	CN negative imaging	*P* value
Number identified/total	162/206	156/206	-
Rate of identification	78.64%	75.73%	0.481
Mean number identified for total thyroidectomy	3.19	3.00	0.457
Mean number identified for thyroid lobectomy	1.55	1.53	0.843

NIRAF: near-infrared autofluorescence imaging; CNs: carbon nanoparticles.

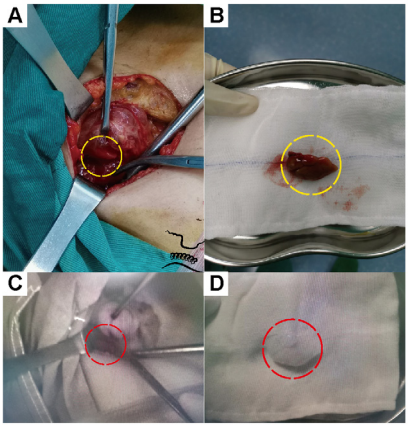

Figure 3. NIRAF imaging and CN negative imaging of a parathyroid adenoma during a parathyroidectomy; the parathyroid glands are circled in red or yellow. (A) CN negative imaging of an upper right parathyroid adenoma; **(B)** Visible light images of the isolated upper right parathyroid adenoma; **(C)** NIRAF imaging of the upper right parathyroid adenoma; **(D)** NIRAF imaging of the isolated upper right parathyroid adenoma.

experienced thyroid surgeons. Moreover, there was no need to use any exogenous dyes or colorant, so NIRAF imaging posed a lower risk during surgery. In addition, the AF intensity of a secondary parathyroid adenoma was weaker than that of a normal PG. The AF intensity did not differ significantly compared to that of the surrounding tissue in the central neck.

The identification and location of PGs is a well-known challenge of thyroid or parathyroid surgery (*14*). Accidental injury or resection may lead to hypoparathyroidism, which means temporary or permanent hypocalcemia and other accompanying symptoms (*15*). Many early intraoperative methods of identifying PGs have been reported, such as intravenous injection of methylene blue(*10*) or ICG (*16*) or 99m-Technetium sestamibi (MIBI) (*17*), CN negative imaging (*18*), measurement of parathyroid hormone levels from needle aspirates of tissue specimens (*19*) and aspartate aminotransferase to lactate dehydrogenase ratios from suspended tissue specimens (*20*). However, few of these methods have been widely adopted and promoted in clinical practice (*21*). Although a frozen section was the gold standard to confirm that a specimen was a PG, obtaining it could damage the integrity of PGs and involve considerable time and cost (*8*). However, the discovery of the intrinsic fluorescence of PGs at NIR wavelengths has allowed the identification of PGs in real time during surgery. Although the detailed mechanism of AF is not yet clear, the mainstream view is that AF was derived from the calcium-sensing receptor protein, which was most concentrated in the chief cells of PGs, less concentrated in the thyroid, and not present in other tissues of the neck (*22*). In patients with secondary hyperparathyroidism, the down-regulation of calcium-sensing receptors leads to a decrease in fluorescence intensity compared to that of normal PGs (*23*). In addition, Squires *et al*. noted significantly lower quantified absolute values of parathyroid AF in situ and ex vivo and significantly lower parathyroid-to-background AF ratios for patients with *vs*. without multiple endocrine neoplasia type 1 (MEN1) (*24*).

In the present study, 78.64% of PGs were detected with NIRAF imaging prior to the dissection, which was consistent with previous reports (*25*). This is because AF was difficult to detect when PGs were buried in surrounding tissue of a certain thickness. Early studies confirmed that about 77-100% of PGs were detectable by NIRAF imaging (*6*). Moreover, Benmiloud *et al*. studied parathyroid AF in 93 patients and found that 68% PGs were identified via NIRAF imaging before they were visualized by the surgeon (*26*). A definite advantage of NIRAF imaging is that it can detect PGs in excised specimens more quickly and efficiently than visual identification by a surgeon (Figure 1). This contention was corroborated by Takahashi *et al*., who emphasized that the sensitivity of NIRAF imaging (82.9%) at detecting PGs from thyroidectomy specimens was significantly higher than that of visual inspection by a surgeon (61.0%) (*27*). NIRAF imaging did not significantly improve the rate of parathyroid identification compared to CN negative imaging (78.64% *vs*. 75.73%), but the former is preferred by surgeons because it has a shorter learning curve and involves lower risk. Different studies have reached conflicting conclusions regarding postoperative hypoparathyroidism or hypocalcemia. A multicenter randomized clinical trial involving 241 patients found that NIRAF-assisted thyroidectomy significantly decreased the rate of early postoperative hypocalcemia compared to a conventional thyroidectomy (9.1% *vs*. 21.7%) with no significant differences in the rate of permanent hypocalcemia (0% *vs*. 1.6%) (*28*). However, Papavramidis *et al*. concluded that the use or lack of NIRAF imaging had no effect on temporary postoperative hypoparathyroidism or hypocalcemia, while NIRAF could drastically

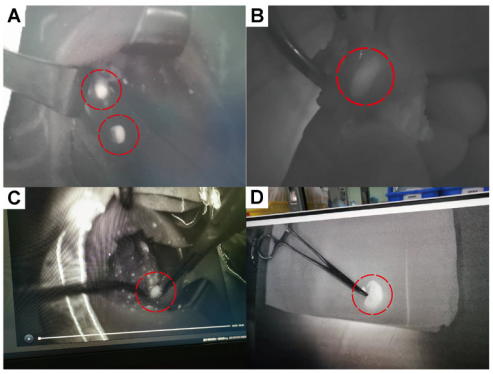

Figure 4. NIRAF imaging of the parathyroid glands under different conditions; the parathyroid glands are circled in red. (A) Ipsilateral upper and lower parathyroid glands in the surgical field; **(B)** A parathyroid gland embedded in an isolated lymph node specimen; **(C)** A parathyroid gland embedded in the thymus; **(D)** A single normal parathyroid gland placed on gauze.

decrease the incidence of permanent postoperative hypoparathyroidism or hypocalcemia (*6*).

Although the fluorescence intensity in this study was not quantified to distinguish PGs from surrounding tissues as in previous studies, PGs emitted significantly stronger fluorescence than surrounding tissues (Figures 2 and 4). Kin *et al*. found that the average fluorescence intensity of PGs calculated by the software Image J was 1.95-5.2 times that of surrounding tissues (*1*). However, McWade *et al*. reported emission intensity from PGs 2.4-8.5 times higher than that from surrounding tissue (*29*). Berber *et al*. found that the optimal tissue/background AF intensity thresholds to predict PGs ranged between 1.46 and 1.72 for different backgrounds (*8*). Moreover, the fluorescence ratio of PGs to surrounding tissues increased with an increase in PG volume and weight (*30*). Even an hour after excision or formalin fixation, the AF of PGs remained stable (*22*). The equipment was set up before surgery and intraoperative imaging took only 2-3 minutes, so the total operating time was not delayed.

However, as a tool for intraoperative real-time identification and localization of PGs, NIRAF imaging still has the following deficiencies: (1) when NIRAF imaging detection equipment was in operation, the ambient light in the operating room had to be completely turned off to eliminate the interference of white light as much as possible; (2) Due to the weak penetration of near-infrared rays, AF may be difficult to detect when the surface tissue of the PG covers more than several millimeters; (3) NIRAF imaging could not evaluate the activity and blood perfusion status of PGs and thus failed to provide guidance for timely intraoperative autologous transplantation or in-situ preservation; (4) Patients with secondary hyperparathyroidism or parathyroid adenoma may exhibit lower intrinsic AF than those with primary hyperparathyroidism or normal PGs; and (5) The equipment needs to be more compact and easier to operate to facilitate real-time intraoperative use. In summary, NIRAF imaging cannot completely replace frozen sections in the short term, but the former could be used as a complement to visual recognition by a surgeon and to minimize unnecessary frozen biopsies in some cases. The above limitations would also provide a direction for the future development and improvement of this technology.

There were certain limitations that should be acknowledged. Firstly, the findings were limited by the insufficient sample size and single-institution nature of this study. Prospective multicenter randomized controlled studies with large sample sizes need to be conducted to further confirm the current results. Secondly, more postoperative indicators such as short- and long-term parathyroidism and serum calcium levels need to be included to better evaluate the effectiveness of NIRAF imaging in preventing hypoparathyroidism. Thirdly, although AF could distinguish PGs from non-PG tissue, histopathological verification may be necessary to confirm that certain samples were indeed PGs.

In conclusion, NIRAF imaging is a potentially more efficient tool for identification of PGs than CN negative imaging, with a shorter learning curve and lower risk. It may not be well-suited to secondary hyperthyroidism or adenoma, but it is more efficient at identifying excised specimens than visual identification by a surgeon.

Acknowledgements

The authors would like to thank all of the clinicians and researchers who contributed to patient care and who helped to collect data at the Union Hospital, Tongji Medical College, Huazhong University of Science and Technology. And data are available upon reasonable request.

Funding: None.

Conflict of Interest: The authors have no conflicts of interest to disclose.

References

1. Kim SW, Song SH, Lee HS, Noh WJ, Oak C, Ahn YC, Lee KD. Intraoperative Real-Time Localization of Normal Parathyroid Glands With Autofluorescence Imaging. J Clin Endocrinol Metab. 2016; 101:4646-4652.
2. Bilezikian JP, Khan A, Potts JT Jr, *et al*. Hypoparathyroidism in the adult: Epidemiology, diagnosis, pathophysiology, target-organ involvement, treatment, and challenges for future research. J Bone Miner Res. 2011; 26:2317-2337.
3. Shoback D. Clinical practice. Hypoparathyroidism. N Engl J Med. 2008; 359:391-403.
4. Kose E, Rudin AV, Kahramangil B, Moore E, Aydin H, Donmez M, Krishnamurthy V, Siperstein A, Berber E. Autofluorescence imaging of parathyroid glands: An assessment of potential indications. Surgery. 2020; 167:173-179.
5. Tufano RP, Clayman G, Heller KS, Inabnet WB, Kebebew

E, Shaha A, Steward DL, Tuttle RM; American Thyroid Association Surgical Affairs Committee Writing Task Force. Management of recurrent/persistent nodal disease in patients with differentiated thyroid cancer: a critical review of the risks and benefits of surgical intervention versus active surveillance. Thyroid. 2015; 25:15-27.
6. Papavramidis TS, Chorti A, Tzikos G, Anagnostis P, Pantelidis P, Pliakos I, Panidis S, Papaioannou M, Bakkar S, Unal E, Michalopoulos A. The effect of intraoperative autofluorescence monitoring on unintentional parathyroid gland excision rates and postoperative PTH concentrations-a single-blind randomized-controlled trial. Endocrine. 2021; 72:546-552.
7. Kim Y, Kim SW, Lee KD, Ahn YC. Real-time localization of the parathyroid gland in surgical field using Raspberry Pi during thyroidectomy: a preliminary report. Biomed Opt Express. 2018; 9:3391-3398.
8. Berber E, Akbulut S. Can near-infrared autofluorescence imaging be used for intraoperative confirmation of parathyroid tissue? J Surg Oncol. 2021; 124:1008-1013.
9. van den Bos J, van Kooten L, Engelen SME, Lubbers T, Stassen LPS, Bouvy ND. Feasibility of indocyanine green fluorescence imaging for intraoperative identification of parathyroid glands during thyroid surgery. Head Neck. 2019; 41:340-348.
10. Patel HP, Chadwick DR, Harrison BJ, Balasubramanian SP. Systematic review of intravenous methylene blue in parathyroid surgery. Br J Surg. 2012; 99:1345-1351.
11. Paras C, Keller M, White L, Phay J, Mahadevan-Jansen A. Near-infrared autofluorescence for the detection of parathyroid glands. J Biomed Opt. 2011; 16:067012.
12. Shi C, Tian B, Li S, Shi T, Qin H, Liu S. Enhanced identification and functional protective role of carbon nanoparticles on parathyroid in thyroid cancer surgery: A retrospective Chinese population study. Medicine (Baltimore). 2016; 95:e5148.
13. Biello A, Kinberg EC, Wirtz ED. Thyroidectomy. StatPearls. Treasure Island (FL): StatPearls Publishing Copyright© 2021, StatPearls Publishing LLC.; 2021.
14. Papavramidis TS, Pliakos I, Chorti A, Panidis S, Kotsovolis G, Stelmach V, Koutsoumparis D, Bakkar S, Michalopoulos A. Comparing Ligasure™ Exact dissector with other energy devices in total thyroidectomy: a pilot study. Gland Surg. 2020; 9:271-277.
15. Kazaure HS, Zambeli-Ljepovic A, Oyekunle T, Roman SA, Sosa JA, Stang MT, Scheri RP. Severe Hypocalcemia After Thyroidectomy: An Analysis of 7366 Patients. Ann Surg. 2021; 274:e1014-e1021.
16. Rudin AV, McKenzie TJ, Thompson GB, Farley DR, Lyden ML. Evaluation of Parathyroid Glands with Indocyanine Green Fluorescence Angiography After Thyroidectomy. World J Surg. 2019; 43:1538-1543.
17. Hall NC, Plews RL, Agrawal A, Povoski SP, Wright CL, Zhang J, Martin EW Jr, Phay J. Intraoperative scintigraphy using a large field-of-view portable gamma camera for primary hyperparathyroidism: initial experience. Biomed Res Int. 2015; 2015:930575.
18. Wang B, Du ZP, Qiu NC, Liu ME, Liu S, Jiang DZ, Zhang W, Qiu M. Application of carbon nanoparticles accelerates the rapid recovery of parathyroid function during thyroid carcinoma surgery with central lymph node dissection: A retrospective cohort study. Int J Surg. 2016; 36:164-169.
19. Farrag T, Weinberger P, Seybt M, Terris DJ. Point-of-care rapid intraoperative parathyroid hormone assay of needle aspirates from parathyroid tissue: A substitute for frozen sections. Am J Otolaryngol. 2011; 32:574-577.
20. Kikumori T, Inaishi T, Miyajima N, Shibata M, Takeuchi D. Robust, quick, and convenient intraoperative method to differentiate parathyroid tissue. Surgery. 2020; 167:385-389.
21. Abbaci M, De Leeuw F, Breuskin I, Casiraghi O, Lakhdar AB, Ghanem W, Laplace-Builhé C, Hartl D. Parathyroid gland management using optical technologies during thyroidectomy or parathyroidectomy: A systematic review. Oral Oncol. 2018; 87:186-196.
22. Kim SW, Lee HS, Lee KD. Intraoperative real-time localization of parathyroid gland with near infrared fluorescence imaging. Gland Surg. 2017; 6:516-524.
23. McWade MA, Sanders ME, Broome JT, Solórzano CC, Mahadevan-Jansen A. Establishing the clinical utility of autofluorescence spectroscopy for parathyroid detection. Surgery. 2016; 159:193-202.
24. Squires MH, Shirley LA, Shen C, Jarvis R, Phay JE. Intraoperative Autofluorescence Parathyroid Identification in Patients With Multiple Endocrine Neoplasia Type 1. JAMA Otolaryngol Head Neck Surg. 2019; 145:897-902.
25. Ladurner R, Sommerey S, Arabi NA, Hallfeldt KKJ, Stepp H, Gallwas JKS. Intraoperative near-infrared autofluorescence imaging of parathyroid glands. Surg Endosc. 2017; 31:3140-3145.
26. Benmiloud F, Rebaudet S, Varoquaux A, Penaranda G, Bannier M, Denizot A. Impact of autofluorescence-based identification of parathyroids during total thyroidectomy on postoperative hypocalcemia: a before and after controlled study. Surgery. 2018; 163:23-30.
27. Takahashi T, Yamazaki K, Ota H, Shodo R, Ueki Y, Horii A. Near-Infrared Fluorescence Imaging in the Identification of Parathyroid Glands in Thyroidectomy. Laryngoscope. 2021; 131:1188-1193.
28. Benmiloud F, Godiris-Petit G, Gras R, Gillot JC, Turrin N, Penaranda G, Noullet S, Chéreau N, Gaudart J, Chiche L, Rebaudet S. Association of Autofluorescence-Based Detection of the Parathyroid Glands During Total Thyroidectomy With Postoperative Hypocalcemia Risk: Results of the PARAFLUO Multicenter Randomized Clinical Trial. JAMA Surg. 2020; 155:106-112.
29. McWade MA, Paras C, White LM, Phay JE, Solórzano CC, Broome JT, Mahadevan-Jansen A. Label-free intraoperative parathyroid localization with near-infrared autofluorescence imaging. J Clin Endocrinol Metab. 2014; 99:4574-4580.
30. Squires MH, Jarvis R, Shirley LA, Phay JE. Intraoperative Parathyroid Autofluorescence Detection in Patients with Primary Hyperparathyroidism. Ann Surg Oncol. 2019; 26:1142-1148.

Received June 9, 2022; Revised June 25, 2022; Accepted June 27, 2022.

§These authors contributed equally to this work.
*Address correspondence to:
Wei Shi and Shoupeng Zhang, Department of Thyroid and Breast Surgery, Union Hospital, Tongji Medical College, Huazhong University of Science and Technology, 1277 Jiefang Avenue, Wuhan 430022, Hubei, China.
E-mail: shiweihust@163.com, 2013xh0903@hust.edu.cn

Released online in J-STAGE as advance publication June 29, 2022.

Correspondence

DOI: 10.5582/bst.2022.01225

Heparin therapy in COVID-19: Call for randomized controlled trials (RCTs)

Tingting Fang[1,§], Xianyang Pan[1,§], Ju Huang[1], Jun Chen[2], Shuli Song[3], Qilin Zhan[1,*]

[1] Department of Hematology, Shanghai Public Health Clinical Center, Fudan University, Shanghai, China;
[2] Department of Infectious Diseases and Immunology, Shanghai Public Health Clinical Center, Fudan University, Shanghai, China;
[3] Department of Nephrology, Shanghai Public Health Clinical Center, Fudan University, Shanghai, China.

SUMMARY Coronavirus disease 2019 (COVID-19) is associated with increases in abnormal coagulation, and particularly D-dimer (D-D) levels. Heparin therapy has been recommended as pharmacologic thromboprophylaxis in patients hospitalized with COVID-19; however, data on its efficacy are lacking. The current study retrospectively analyzed changes in blood coagulation and the impact of heparin therapy. Medical records of 593 patients with confirmed COVID-19 were collected. On admission, elevated fibrinogen (Fg) levels were noted in with 42.2% (250/593) of patients, followed by increases in D-D (28.5%) and a prolonged prothrombin time (PT) (23.9%). Patients with severe/critical COVID-19 had a higher proportion of abnormal coagulation parameters than patients with mild/ordinary COVID-19. Dynamic changes in coagulation parameters were plotted on timeline charts for 97 patients with COVID-19 after heparin treatment. These changes, when combined with Fg, PT, D-D, and other indicators, may provide a relatively comprehensive description of coagulation abnormalities. Heparin seems to be important in the treatment of patients with COVID-19 based on the current findings. The efficacy of heparin in the treatment of COVID-19 should be confirmed by randomized controlled trials (RCTs) as soon as possible.

Keywords coronavirus infection, COVID-19, blood coagulation, heparin, fibrin degradation products

Coronavirus disease 2019 (COVID-19) has been reported in Wuhan since December 2019 and has since spread throughout China and around the world (*1,2*). Despite this immense global burden, no pharmacologic therapies have definitively proven beneficial. Around the world, researchers have been trying to understand the disease manifestations in order to develop both prognostic and therapeutic tools.

Abnormal coagulation has been noted clinically in patients with COVID-19. A severe acute respiratory syndrome coronavirus 2 (SARS-CoV-2) infection might lead to an increased risk of both arterial and venous thrombosis, which may be attributed to the widespread endothelial cell damage caused either directly by the virus itself or indirectly by the burst of proinflammatory cytokines (*3-7*). Monitoring coagulation parameters in patients with COVID-19 is crucial to analyzing the overall severity of the disease. D-dimer (D-D) levels in particular are prognostically significant for mortality in COVID-19 (*6,7*). The degree of increased fibrin degradation products (FDP) and D-D in severe/critical ill patients is significantly higher than in patients with milder disease and who did not die (*8,9*). However, there is no consensus on the difference in coagulation in patients with COVID-19 of varying degrees of severity. Increased attention is being paid to the impact of heparin treatment on patients with COVID-19. Several studies have reported the use of higher doses of heparin to decrease mortality in patients with COVID-19 and additional risk factors. However, anticoagulant therapy mainly with low molecular weight heparin did not appear to improve clinical outcomes in several patients with severe COVID-19 (*10-14*) (Supplemental Table S1, *http://www.biosciencetrends.com/action/getSupplementalData.php?ID=105*). The American Society of Hematology recommended pharmacologic thromboprophylaxis in patients hospitalized with COVID-19 (unless contraindicated) and suggested the administration of therapeutic doses when thrombosis is proven or highly suspected based on clinical findings (*13*). Nonetheless, the optimal preventive strategy in terms of the intensity of anticoagulation for patients with COVID-19 remains to be determined.

In order to answer these questions, the current authors conducted a retrospective study to analyze the relationship between coagulation parameters in 593

patients with COVID-19 of varying severity. Moreover, the dynamic profile of coagulation parameters was determined in patients with COVID-19 receiving heparin therapy. Those parameters may have prognostic value and may indicate important therapeutic targets.

This study collected the medical records of patients (non-pregnant women, over the age of 18) with COVID-19 confirmed by RT-PCR seen at the Shanghai Public Health Clinical Center in Shanghai from January 20, 2020 to May 20, 2020. Patients were categorized into two groups according to disease severity: a group with mild/ordinary COVID-19 and a group with severe/critical COVID-19. The categorization of COVID-19 was according to the World Health Organization's interim guidance (*15*). This study was approved by the Ethics Committee of the Shanghai Public Health Clinical Center (approval no. YJ-2020-S131-01). Informed consent was obtained from all participants.

Patients with COVID-19 were treated with prophylactic doses of heparin depending on their D-D or FDP levels. Patients with D-D > 0.5 mg/L and FDP > 5 mg/L were given 3,000 – 5,000 U of low-molecular weight heparin by subcutaneous injections to prevent thrombosis. Patients with D-D > 5 mg/L were given 6,000 – 8,000 U of low-molecular weight heparin. Patients with D-D > 5 mg/L and FDP > 10 mg/L were given 12,500 – 20,000 U of unfractionated heparin daily by syringe pumps to alleviate abnormal coagulation. The heparin was administered daily for three to five days.

Demographic data, the medical history, clinical characteristics, and laboratory coagulation parameters of the patients on admission were obtained. The coagulation profile was assessed using the following parameters: fibrinogen (Fg), activated partial thromboplastin time (APTT), prothrombin time (PT), thrombin time (TT), D-D, and FDP. For patients who received heparin after admission, data on coagulation parameters (PT, APTT, FDP, D-D) were collected on the day that heparin treatment started to provide a baseline for comparison, and that point was designated Measuring Point 0 (MP 0). In addition, the endpoints at MP 3 were the measurements following heparin treatment. The two measuring points (MP 1 and MP2) were chosen in accordance with time and were evenly distributed between the two points above when blood was collected.

The study included 593 patients with confirmed COVID-19. Demographic characteristics of and coagulation parameters in the sample population are shown in Table 1. More than half of the patients were male (55,5%), and 103 (17.4%) received heparin. Mean age was 42.6-years old (± 16.9). In the 593 patients, increased Fg levels were noted in 42.2% (250/593), increased D-D levels were noted in 28.5%, and prolongation of PT was noted in 23.9%. A decreased platelet count was noted in only 3.2% (19/593) of patients. The APTT was prolonged in 108 patients (18.2%), and it was longer than 10 seconds in 10 of those patients.

Also shown in Table 1 are the differences in parameters between patients with severe/critical COVID-19 and those with mild/ordinary COVID-19. All of the median values for PLT, PT, APTT, FDP, D-D, and TT in the two groups were within the normal range. Coagulation parameters (APTT, Fg, FDP, D-D) except for TT differed significantly in the group with severe/critical COVID-19 and the group with mild/ordinary COVID-19 ($P < 0.05$). Patients with severe/critical COVID-19 had more abnormal coagulation parameters than patients with mild/ordinary COVID-19, including prolonged PT, prolonged APTT, Fg > 4g/L, FDP > 5 mg/

Table 1. Demographic characteristics of and coagulation parameters in patients with COVID-19 on admission

Parameters	Normal range	Total (n = 593)	Severe/Critical (n = 32)	Mild/Ordinary (n = 561)	P
Age (years)		42.6 ± 16.9	62.3 ± 15.7	41.4 ± 16.3	< 0.001
Sex (male/female)		329/264	25/7	304/257	0.008
Heparin treatment		103	29	68	< 0.001
On admission	125-350				
PLT	11-13.7	202 (157-251)	167.5 (130.5-203.3)	206 (160.5-253.0)	0.002
PT	31.5-42.5	13.3 (12.9-13.7)	13.7 (12.9-14.4)	13.3 (12.9-13.7)	0.036
APTT	2.0-4	38.2 (35.4-41.3)	42.1 (36.8-48.7)	38.1 (35.4-40.9)	< 0.001
Fg	0-5	3.7 (3.0-4.6)	4.62 (4.03-5.27)	3.68 (3.00-4.57)	< 0.001
FDP	0-0.5	0.65 (0.22-1.36)	1.96 (1.02-4.04)	0.62 (0.22-1.33)	< 0.001
D-D	14-21	0.35 (0.23-0.55)	0.87 (0.45-1.50)	0.33 (0.23-0.53)	< 0.001
TT		16.4 (15.7-17.1)	16.5 (15.9-18.1)	16.4 (15.7-17.1)	0.089
Coagulation					
PLT < 100×10^9/L		19 (3.2)	2 (6.2)	17 (3.0)	0.270
PT Increased		142 (23.9)	15 (46.9)	127 (22.6)	0.002
APTT Increased		110 (18.5)	15 (46.9)	95 (16.9)	< 0.001
Fg > 4 g/L		250 (42.2)	25 (78.1)	225 (40.1)	< 0.001
FDP > 5 mg/L		18 (3.0)	5 (15.6)	13 (2.3)	0.002
DD > 0.5 mg/L		169 (28.5)	22 (68.8)	147 (26.2)	< 0.001

PLT, platelet count; PT, prothrombin time; APTT, activated partial thromboplastin time; Fg, fibrinogen; FDP, fibrin degradation products; D-D, D-dimer; TT, thrombin time;

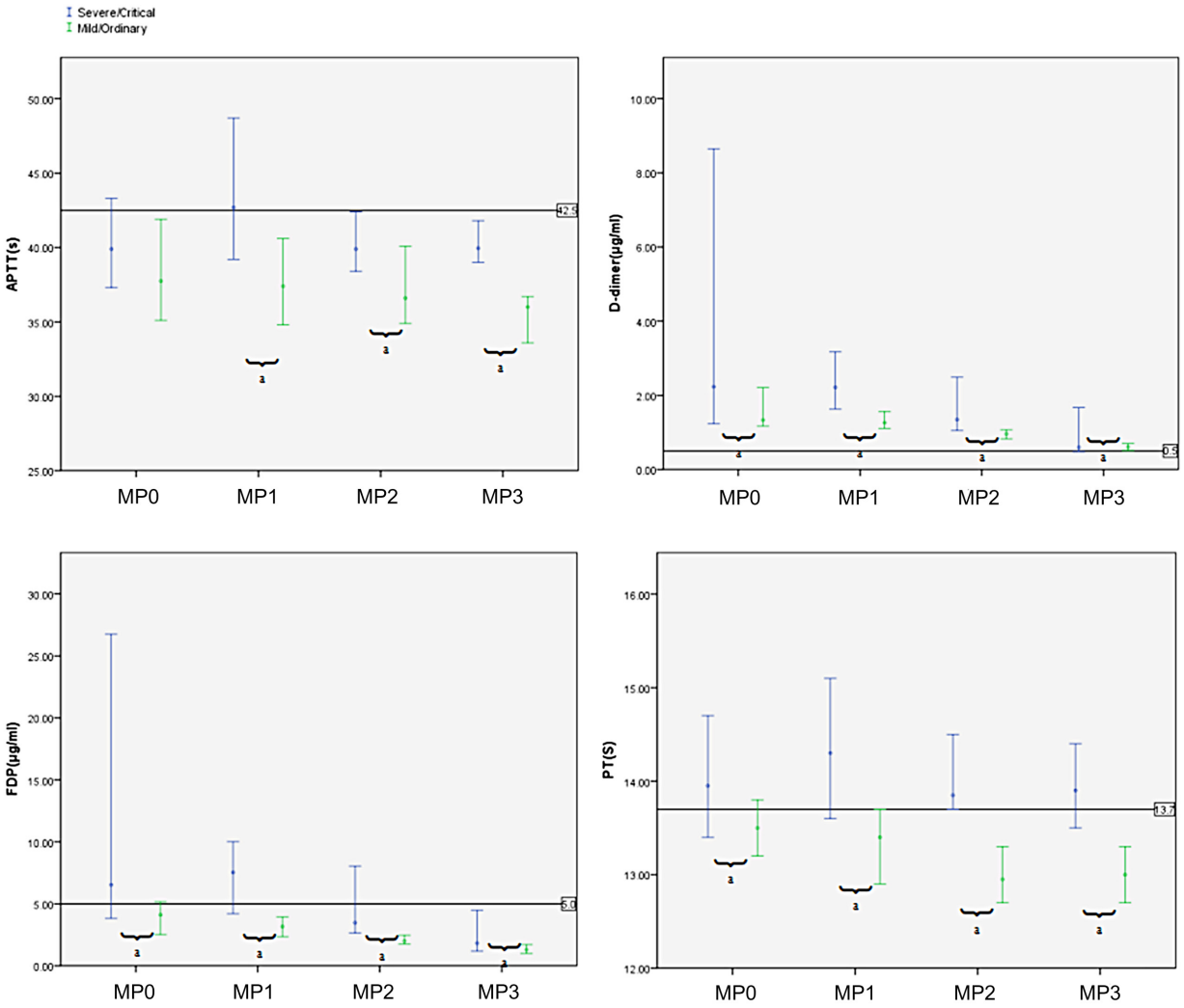

Figure 1. Dynamic profile of coagulation parameters in patients with COVID-19. Timeline charts illustrate changes in coagulation parameters in 97 patients with COVID-19 (29 patients with severe/critical COVID-19 and 68 patients with mild/ordinary COVID-19) after heparin treatment. The error bars indicate medians and 25% and 75% percentiles. The horizontal lines indicate the upper normal limits of PT, APTT, D-D, and FDP. [a]$P < 0.05$ for severe/critical versus mild/ordinary COVID-19.

L, and D-D > 0.5 mg/L.

A total of 103 patients (17.3%) received heparin therapy; 29 had severe/critical COVID-19 and 68 had mild/ordinary COVID-19. Timeline charts illustrate the dynamic changes in coagulation parameters in the 97 patients with COVID-19 after heparin treatment, as determined at 4 measuring points (MP 0, MP 1, MP 2, and MP 3) (Figure 1). As a result of heparin therapy, the coagulation parameters (D-D, FDP, PT, and APTT) decreased rapidly in both groups, including patients with severe/critical and those with mild/ordinary COVID-19, which indicated the effect of heparin therapy, despite increased coagulation parameters in patients with severe/critical COVID-19.

Patients with COVID-19 are prone to venous, cerebrovascular, and coronary thrombi, and this is particularly true in those with severe disease (*3,16*). Abnormalities in a given coagulation parameter might have limited ability to predict venous thrombosis in people infected with SARS-CoV-2. The complete coagulation parameters in patients with COVID-19 cases might have prognostic value and indicate important therapeutic targets.

An acute phase reactant protein, Fg is an important component of the coagulation cascade that can lead to hypercoagulability and thrombosis if increased. Moreover, it can significantly increase in patients with early-stage mild or critical COVID-19 and significantly decrease in patients with late-stage critical COVID-19 (*17*). In the patients in the current study, 42.2% had increased Fg levels upon admission. This was the most common abnormality. In line with previous studies, abnormal Fg levels were significantly higher in patients with severe/critical COVID-19 than in those with mild/ordinary COVID-19 (*4,17*).

In 28.5% of patients, levels of D-D were elevated on admission, suggesting that the fibrinolytic system and thrombogenesis were active. D-D levels are elevated in patients who are likely to have COVID-19, so clinicians need to be aware of the potential for thrombosis in these

patients. In addition, D-D levels were slightly elevated in most patients, and that level was over 5 mg/L in just 1.85%, suggesting that the likelihood of thrombosis formation is limited and that disseminated intravascular coagulation (DIC) did not develop. Alternatively, this complication might be self-limited by a timely diagnosis and treatment or by the body's own resistance. D-D levels differed significantly in patients with critical COVID-19 and patients with mild COVID-19; this indicated that conventional coagulation parameters during the course of COVID-19 were significantly associated with disease prognosis. Some patients with critical COVID-19 deteriorated suddenly during treatment, suggesting they may be at greater risk of thrombosis (*3,4*).Combining PT, APTT, and other indicators can provide a comprehensive description of coagulation abnormalities. Therefore, these factors closely need to be monitored closely. If a serious situation arises, medical personnel can immediately take appropriate measures.

Several studies have indicated that a therapeutic dose of heparin improves clinical outcomes in patients with mild or ordinary COVID-19 on hospital admission (*10,11,17*). However, use of anti-thrombotics to improve outcomes in patients with severe COVID-19 is controversial (*10,11,16*). In the current study, the four coagulation indicators (D-D, FDP, PT, and APTT) were significantly higher in patients with severe/critical COVID-19 than in patients with mild/ordinary COVID-19 at the same measuring point, possibly because tissue damage has already occurred. Patients with severe/critical COVID-19 were not able to recover to the same degree as those with mild/ordinary COVID-19 by the end of heparin treatment. To some extent, this finding reflects the importance of heparin in the early treatment of patients with COVID-19. Notably, the coagulation parameters in most patients returned to normal - D-D, FDP, PT, and APTT in particular - after the intervention with heparin. These parameters might have the potential to guide treatment and evaluate prognosis. Heparin treatment should be initiated as soon as possible in patients with COVID-19 who meet the corresponding criteria for receiving heparin. A limitation of the current retrospective study is that it was unable to establish a direct causal connection. Randomized controlled trials (RCTs) should be conducted as soon as possible to confirm the efficacy of heparin in treating COVID-19 and to explore its appropriate timing and dose.

Acknowledgements

The authors wish to thank all of the participants who participated in this study.

Funding: This study was supported by grants from the Shenzhen Project to Fund Medical and Health Care by Noted Physicians, Hospitals, and Clinics (grant number: SZSM201512029); the National Science Foundation of China (grant number: 92169119), the Program to Produce Academic Personnel of the Shanghai 3-year Action Plan to Create a Public Health System (2020-2022)-Health Education and Health Communication (grant number: GWV-10.1-XK02), the Wuxi Health Committee's Program to Fund Talented Young and Middle-aged Researchers (BJ2020091), and a Project funded by the Shenzhen Third People's Hospital (grant numbers: G2021027 and G2022062).

Conflict of Interest: The authors have no conflicts of interest to disclose.

References

1. Lu H, Stratton CM, Tang YW. Outbreak of pneumonia of unknown etiology in Wuhan China: The mystery and the miracle. J Med Virol. 2020; 92:401-402.
2. Hui DS, I Azhar E, Madani TA, Ntoumi F, Kock R, Dar O, Ippolito G, Mchugh TD, Memish ZA, Drosten C, Zumla A, Petersen E. The continuing 2019-nCoV epidemic threat of novel coronavirus outbreak to global health-The latest 2019 novel coronavirus in Wuhan, China. Int J Infect Dis. 2020; 91:264-266.
3. Guan WJ, Ni ZY, Hu Y, *et al*. Clinical characteristics of 2019 novel coronavirus infection in China. N Engl J Med, 2020; 382:1708-1720.
4. Tang N, Li D, Wang X, Sun Z. Abnormal Coagulation parameters are associated with poor prognosis in patients with novel coronavirus pneumonia. J Thromb Haemost, 2020; 18:844-847.
5. Middeldorp S, Coppens M, van Haaps TF, Foppen M, Vlaar AP, Müller MCA, Bouman CCS, Beenen LFM, Kootte RS, Heijmans J, Smits LP, Bonta PI, van Es N. Incidence of venous thromboembolism in hospitalized patients with COVID-19. J Thromb Haemost. 2020; 18:1995-2002.
6. Lodigiani C, Iapichino G, Carenzo L, Cecconi M, Ferrazzi P, Sebastian T, Kucher N, Studt JD, Sacco C, Bertuzzi A, Sandri MT, Barco S; Humanitas COVID-19 Task Force. Venous and arterial thromboembolic complications in COVID-19 patients admitted to an academic hospital in Milan, Italy. Thromb Res. 2020; 191:9-14.
7. Helms J, Tacquard C, Severac F, *et al*. High risk of thrombosis in patients with severe SARS-CoV-2 infection: A multicenter prospective cohort study. Intensive Care Med. 2020; 46:1089-1098.
8. Mao L, Jin H, Wang M, Hu Y, Chen S, He Q, Chang J, Hong C, Zhou Y, Wang D, Miao X, Li Y, Hu B. Neurological manifestations of hospitalized patients with COVID-19 in Wuhan, China: A retrospective case series study. JAMA Neurol. 2020; 77:1-9.
9. Wang D, Hu B, Hu C, Zhu F, Liu X, Zhang J, Wang B, Xiang H, Cheng Z, Xiong Y, Zhao Y, Li Y, Wang X, Peng Z. Clinical characteristics of 138 hospitalized patients with 2019 novel coronavirus-infected pneumonia in Wuhan, China. JAMA. 2020; 323:1061-1069.
10. Di Micco P, Tufano A, Cardillo G, Imbalzano E, Amitrano M, Lodigiani C, Bellizzi A, Camporese G, Cavalli A, De Stefano C, Russo V, Voza A, Perrella A, Prandoni P. The impact of risk-adjusted heparin regimens on the outcome of patients with COVID-19 infection. A prospective cohort study. Viruses. 2021; 13:1720.

11. Tang N, Bai H, Chen X, Gong J, Li D, Sun Z. Anticoagulant treatment is associated with decreased mortality in severe coronavirus disease 2019 patients with coagulopathy. J Thromb Haemost. 2020; 18:1094-1099.
12. Shi C, Wang C, Wang H, Yang C, Cai F, Zeng F, Cheng F, Liu Y, Zhou T, Deng B, Vlodavsky I, Li JP, Zhang Y. The potential of low molecular weight heparin to mitigate cytokine storm in severe COVID-19 patients: A retrospective cohort study. Clin Transl Sci. 2020; 13:1087-1095.
13. Canoglu K, Saylan B. Therapeutic dosing of low-molecular-weight heparin may decrease mortality in patients with severe COVID-19 infection. Ann Saudi Med. 2020; 40:462-468.
14. Marcos-Jubilar M, Carmona-Torre F, Vidal R, Ruiz-Artacho P, *et al*. Therapeutic versus prophylactic bemiparin in hospitalized patients with nonsevere COVID-19 pneumonia (BEMICOP Study): An open-label, multicenter, randomized, controlled trial. Thromb Haemost. 2022; 122:295-299.
15. World Health Organization. Clinical management of severe acute respiratory infection when novel coronavirus (nCoV) infection is suspected: Interim guidance. *https://www.who.int/publications-detail/clinical-management-of-severe-acute-respiratory-infection-when-novel-coronavirus-(ncov)-infection-is-suspected* (accessed April 30, 2022).
16. Gibbs DV, Shreenivas SS, Hudock KM. Role of acute thrombosis in coronavirus disease 2019. Crit Care Clin. 2022; 38:491-504.
17. Fragkou PC, Palaiodimou L, Stefanou MI, Katsanos AH, Lambadiari V, Paraskevis D, Andreadou E, Dimopoulou D, Zompola C, Ferentinos P, Vassilakopoulos TI, Kotanidou A, Sfikakis PP, Tsiodras S, Tsivgoulis G. Effects of low molecular weight heparin and fondaparinux on mortality, hemorrhagic and thrombotic complications in COVID-19 patients. Ther Adv Neurol Disord. 2022; 15:17562864221099472.

Received May 23, 2022; Revised July 13, 2022; Accepted July 27, 2022.

[§]These authors contributed equally to this work.
**Address correspondence to:*
Qilin Zhan, Shanghai Public Health Clinical Center, Fudan University, 2901 Caolang Road, Jinshan, Shanghai, China.
E-mail:qlzhan3@163.com

Released online in J-STAGE as advance publication July 30, 2022.

Correspondence

DOI: 10.5582/bst.2022.01333

Marburg virus disease: A deadly rare virus is coming

Fang Zhao[§], Yun He[§], Hongzhou Lu[*]

National Clinical Research Centre for Infectious Diseases, The Third People's Hospital of Shenzhen and the Second Hospital Affiliated to Southern University of Science and Technology, Shenzhen, Guangdong, China.

SUMMARY Two cases of the deadly Marburgvirus were reported in Ghana, which might be a new global virus alert following COVID-19 and novel monkeypox. Thus far, there is no vaccine or treatment for Marburg virus disease, which is a disease with a mortality rate as high as that of Ebola. Although now human infections with Marburgvirus occurred mainly in Africa, outbreaks were twice reported in Europe over the past 55 years. A concern is that globalization might promote its global viral transmission, just like what happened with COVID-19. The current study has briefly summarized the etiology, epidemiology, and clinical symptoms of the Marburgvirus as well as vaccine development and experimental treatments in order to prevent and control this virus.

Keywords Marburgvirus (MARV), Marburg virus disease (MVD), emerging infectious disease, public health

On July 17, 2022, the World Health Organization (WHO) declared outbreaks of Marburg virus disease (MVD) in Ghana. The world must be on alert regarding deadly MVD following COVID-19 and the novel monkeypox. The Marburg virus (MARV), a deadly cousin of the Ebola virus, is a member of the Filoviridae family (filovirus), which causes severe viral hemorrhagic fever (VHF) in humans. MARV is one of the most fatal viruses ever known, with a morbidity rate of approximately 50%. During the largest reported MARV outbreak in Angola in 2005, more than 250 people were infected and 90% died (*1*). Facing such a fatal virus, many scientists and clinicians have expressed their concerns about its potential threat to public health. Here, the key characteristics of MVD are highlighted to help prevent and control MVD before it spreads globally.

Pathogenetic characteristics: MARV is an enveloped, single-stranded, negative-sense RNA virus. Morphologically, it resembles silk, with a length ranging from 800 to 14,000 nm. It is most infectious when its length is about 790 nm. MARV consists of seven structural proteins. Although the MARV is almost identical to the Ebola virus in structure, it may induce different antibodies in infectious individuals (*2*). MARV is believed to be the first filovirus discovered by humans (*3*).

Epidemiological characteristics: MVD was first reported in 1967 after outbreaks occurred simultaneously in three cities: Marburg, Frankfurt, and Belgrade (*4*). The source of the outbreak was ultimately traced to a laboratory using African green monkeys imported from Uganda. Henceforward, most human infections were reported in Angola, the Congo, Kenya, South Africa, Uganda and Zimbabwe, along with a laboratory accident in Russia (*5*).

In 2009, scientists successfully isolated MARV from healthy Egyptian fruit bats caught in a Uganda mine, which strongly suggested that the fruit bat is the viral reservoir and natural host of MARV (*6*). MVD outbreaks occurred widely across central Africa, suggesting that MVD is present in chronically infected bats (*7*). In addition, African green monkeys and pigs are susceptible to filoviruses, so they play a role as potential amplifier hosts.

MARV can be transmitted animal-to-human or human-to-human via direct contact with blood, secretions, organs, or bodily fluids of infected people or via surfaces contaminated with these fluids through broken skin or mucous membranes. MARV can persist in the eyes and testes of convalescent patients. It is also found in the placenta, amniotic fluid, and breast milk of pregnant women. Put simply, once the virus is found in the blood, the individual remains infectious. However, there is no evidence that MARV can be transmitted among humans by mosquitoes or other biting arthropods.

Clinical manifestations: The incubation period for MVD commonly ranges from 2 to 21 days (average: 5-6 days), though some studies have extended the maximum period to 26 days (*8*). Three stages of the clinical course can be distinguished. Symptoms of illness start abruptly

Table 1. Progress of vaccine development and experimental treatments for Marburg virus disease

Therapy	Description	Animal studies	Clinical trials	*Ref.*
Vaccine				
MVA-BN-Filo	Modified vaccinia Ankara vector encoding GPs from Ebola virus, Sudan virus, Marburg virus, and Tai Forest virus nucleoproteins.	No data.	Phase 1 indicated sustained Ebola GP immunity 8 months post-vaccination. No results related to MARV were published.	(*10*)
rVSV-MARV-GP	Recombinant vesicular stomatitis virus vector expressing the MARV glycoprotein (GP).	100% survivability in study animals (macaques) 14 months post-vaccination.		(*9*)
cAd3-MARV	Chimpanzee adenovirus type-3 vector encoding the GP from MARV.	No data for cAd3-MARV.	Phase 1 trial: 80-90% produced a Marburg-specific antibody response.	*NCT03475056*
CAdVax-panFilo	The complex adenovirus (CAdVax) encoding GPs from EBOV, SUDV and MARV, and EBOV and MARV-Musoke nucleoproteins.	Antibodies were produced against all five filoviruses and no macaques developed clinical illness.		(*14*)
DNA plasmid vaccine	A Marburg DNA plasmid expressing MARV Angola DNA.	A DNA prime/boost vaccine in macaques provided protection, but all animals developed clinical illness.	Phase 1 trial: 90% had antibody responses in 10 people.	(*15,16*) *NCT00605514*
Antivirals				
Galidesivir (BCX4430)	Synthetic nucleoside analogue that inhibits viral RNA polymerase.	17/18 macaques survived with treatment 1, 24, and 48 h post-infection.	Phase 1 trial: results not published.	(*17*)
Remdesivir (GS-5734)	Mono-phosphoramidate prodrug of an adenosine analog with broad antiviral activity. Inhibits MARV *in vitro*.	Protected 50% and 83% of MARV-infected macaques from lethal disease when initiated up to 4-5 days post-infection with MVD.		(*18*)
Favipiravir (T-705)	Synthetic guanidine nucleoside analogue with broad-spectrum antiviral activity against multiple RNA viruses.	5/6 macaques survived when administered IV on the day of the challenge, but not with oral doses.		(*19,20*)
AVI-7288/7287 or AVI-6003	Positively charged antisense phosphorodiamidate morpholino oligomers AVI-7287 and AVI-7288 target the VP24 and NP genes, respectively.	AVI-7288:83-100% of infected monkeys survived when treatment was initiated 1, 24, 48, or 96 h post-infection.	AVI-6003: no significant safety signals in two RCTs with 70 subjects.	(*21-23*)
NP-718m-LNP	Lipid nanoparticle small-interfering RNA targets MARV nucleoprotein.	All 16 macaques survived with treatment 30 to 45 min, 24, 48, or 72-h post infection.		(*24*)
Antibody				
Polyclonal IgG	Concentrated IgG derived from previously vaccinated NHP survivors from Marburg challenge.	3/3 macaques survived with treatment at D2/D2/D8 post infection.		(*17*)
MR 191N (mAb)	Made in Nicotiana tobacco plants binds the receptor of MARV GP.	9/10 macaques survived with treatment at D5/D8 post infection.	Used following a U.S. lab exposure, but details have not been published.	(*25-27*)
MR186-YTE (mAb)	Made in CHOK1-AF cells binds the receptor of MARV GP.	4/4 and 0/5 macaques survived with treatment at D5 or D6 post infection.		(*11*)

Table 2. Chronology of major Marburg virus disease outbreaks

Year	Country	Suspected origin	Cases	Deaths (mortality rate)	Notes
2022	Ghana	Under investigation	2	2 (100%)	
2021	Guinea	Guinea	1	1 (100%)	
2017	Uganda	Uganda	4	3 (75%)	
2014	Uganda	Uganda	1	1 (100%)	
2012	Uganda	Uganda	15	4 (27%)	
2008	Netherlands	Uganda	1	1 (100%)	Imported
2008	USA	Uganda	1	0 (0)	Imported
2007	Uganda	Uganda	4	1 (25%)	
2004-2005	Angola	Angola	252	227 (90%)	
1998-2000	Democratic Republic of the Congo (DRC)	DRC	154	128 (83%)	
1990	Russia	Russia	1	1 (100%)	Laboratory accident
1987	Kenya	Kenya	1	1 (100%)	
1980	Kenya	Kenya	2	1 (50%)	
1975	South Africa	Zimbabwe	3	1 (33%)	Imported
1967	Germany and Yugoslavia	Uganda	31	7 (23%)	Imported & lab leak

Table adapted from the WHO Marburg Virus Disease Factsheet (August 7, 2021).

with a high fever, and severe myalgia and headaches are also reported in the early stage, often followed by vomiting, diarrhea, and abdominal pain on the third day. Watery diarrhea may last for a week, along with severe exhaustion and lethargy. A severe hemorrhagic rash may develop between 5 and 7 days. Patients who die commonly have fresh blood in their vomit and feces and they may also have bleeding from the nose, gums, or vagina. Patients who die commonly do so from shock and multi-organ failure 8-9 days after infection.

Considerations regarding diagnosis: An appropriate clinical diagnosis of MVD may be difficult because its signs and symptoms are quite analogous to those of other infectious diseases, such as malaria, typhoid fever, meningitis, and the other viral hemorrhagic fevers. Diagnosis can be confirmed using the following diagnostic approaches: *i)* an antibody-capture enzyme-linked immunosorbent assay (ELISA); *ii)* an antigen-capture ELISA test; *iii)* a serum neutralization test; *iv)* a reverse transcription-polymerase chain reaction (RT-PCR) assay; *v)* electron microscopy; or *vi)* virus isolation by cell culture. Laboratory staff must implement stringent protective measures because MARV is classified as a Risk Group 4 pathogen (RG-4).

Treatment and prevention: Thus far, there is no approved vaccine or antiviral treatment for MVD. However, supportive care including balancing fluid and electrolyte levels, maintaining oxygen levels and blood pressure, and replacing lost blood and clotting factors might be helpful.

Several potential MARV vaccines are under investigation. For example, a recombinant vesicular stomatitis virus (VSV)-based vaccine expressing the MARV glycoprotein (VSV-MARV) rapidly protected hosts from MVD in animal models (*9*). Another vaccine candidate, MVA-BN-Filo, containing both Marburg and Ebola virus antigens was also reported to potentially protect against both hemorrhagic viruses (*10*). A phase 3 trial is currently underway, and it seems to trigger good immunity against the Ebola virus, but it has not yet been tested against MARV.

Besides prophylactic vaccines, researchers are now attempting to develop effective postexposure therapies for MVD, including MARV-specific monoclonal antibodies (mAbs) and small-molecule antivirals. Researchers combined a monoclonal antibody (MR186-YTE) and an antiviral (remdesivir) against MVD in a non-human primate model (*11*). Data indicated that this particular combination was highly effective in eliminating the virus. The progress of vaccine development and experimental treatments for MVD are summarized in Table 1.

Public health measures: Emerging infectious diseases, and particularly those caused by bat-borne viruses (*e.g.*, Coronaviruses and the Ebola virus), markedly affect public health and the global economy. Like the Ebola virus, MARV is a highly contagious and deadly virus. Once an MVD outbreak is out of hand, it will expand rapidly and cause severe social and health problems. Key protective measures should be immediately taken to prevent this situation.

The main goal of controlling an MVD outbreak is to interrupt direct human-to-human transmission. The control strategy is analogous to that for other infectious disorders, including early identification and rapid isolation of cases, timely tracing, close monitoring of people at risk, proper personal protection, and safe burial. In addition, avoiding the handling and eating of bush meat is also critical to avoiding any potential infection from animals. The spread of MARV outside Africa is primarily due to international travel (*12,13*). Rapid diagnostics are therefore indispensable to identify the infected before they can carry the virus to other countries.

In conclusion, there have been 15 MARV outbreaks reported around the world thus far (Table 2). Because of its potent infectivity and high fatality rate, MARV is a major public health concern in Africa. Nowadays, however, its impact might be global because of frequent migration and travel. Due to the rapid growth of trade

with African countries, Guangzhou, the biggest city in South China, has become the largest African settlement in Asia. Thousands of people from Africa enter this city every day, and the same thing happens in many parts of the world as well. There is a risk of imported MARV in every country. Hence, international cooperation seems to be crucial to preventing and controlling MARV. Scientists should continue study MARV in the field of vaccine and antiviral medicine to stop this deadly illness as quickly as possible.

Acknowledgements

We are grateful to Prof. Asakawa Tetsuya for his editing.

Funding: This work was supported by the National Natural Science Foundation of China (no. 92169119)

Conflict of Interest: The authors have no conflicts of interest to disclose.

References

1. Amman BR, Bird BH, Bakarr IA, *et al*. Isolation of Angola-like Marburg virus from Egyptian rousette bats from West Africa. Nat Commun. 2020; 11:510.
2. King LB, West BR, Schendel SL, Saphire EO. The structural basis for filovirus neutralization by monoclonal antibodies. Curr Opin Immunol. 2018; 53:196-202.
3. Siegert R, Shu HL, Slenczka W. Isolation and identification of the "Marburg virus". Dtsch Med Wochenschr. 1968; 93:604-612. (in German)
4. Slenczka W, Klenk HD. Forty years of marburg virus. J Infect Dis. 2007; 196 Suppl 2:S131-135.
5. Nikiforov VV, Turovskii Iu I, Kalinin PP, *et al*. A case of a laboratory infection with Marburg fever. Zh Mikrobiol Epidemiol Immunobiol. 1994;104-106. (in Russian)
6. Towner JS, Amman BR, Sealy TK, *et al*. Isolation of genetically diverse Marburg viruses from Egyptian fruit bats. PLoS Pathog. 2009; 5:e1000536.
7. Pigott DM, Golding N, Mylne A, Huang Z, Weiss DJ, Brady OJ, Kraemer MU, Hay SI. Mapping the zoonotic niche of Marburg virus disease in Africa. Trans R Soc Trop Med Hyg. 2015; 109:366-378.
8. Pavlin BI. Calculation of incubation period and serial interval from multiple outbreaks of Marburg virus disease. BMC Res Notes. 2014; 7:906.
9. Marzi A, Jankeel A, Menicucci AR, Callison J, O'Donnell KL, Feldmann F, Pinski AN, Hanley PW, Messaoudi I. Single Dose of a VSV-Based Vaccine Rapidly Protects Macaques From Marburg Virus Disease. Front Immunol. 2021; 12:774026.
10. Anywaine Z, Barry H, Anzala O, *et al*. Safety and immunogenicity of 2-dose heterologous Ad26.ZEBOV, MVA-BN-Filo Ebola vaccination in children and adolescents in Africa: A randomised, placebo-controlled, multicentre Phase II clinical trial. PLoS Med. 2022; 19:e1003865.
11. Cross RW, Bornholdt ZA, Prasad AN, *et al*. Combination therapy protects macaques against advanced Marburg virus disease. Nat Commun. 2021; 12:1891.
12. Centers for Disease C, Prevention. Imported case of Marburg hemorrhagic fever – Colorado, 2008. MMWR Morb Mortal Wkly Rep. 2009; 58:1377-1381.
13. Timen A, Koopmans MP, Vossen AC, van Doornum GJ, Gunther S, van den Berkmortel F, Verduin KM, Dittrich S, Emmerich P, Osterhaus AD, van Dissel JT, Coutinho RA. Response to imported case of Marburg hemorrhagic fever, the Netherland. Emerg Infect Dis. 2009; 15:1171-1175.
14. Swenson DL, Warfield KL, Larsen T, Alves DA, Coberley SS, Bavari S. Monovalent virus-like particle vaccine protects guinea pigs and nonhuman primates against infection with multiple Marburg viruses. Expert Rev Vaccines. 2008; 7:417-429.
15. Geisbert TW, Bailey M, Geisbert JB, Asiedu C, Roederer M, Grazia-Pau M, Custers J, Jahrling P, Goudsmit J, Koup R, Sullivan NJ. Vector choice determines immunogenicity and potency of genetic vaccines against Angola Marburg virus in nonhuman primates. J Virol. 2010; 84:10386-10394.
16. Riemenschneider J, Garrison A, Geisbert J, *et al*. Comparison of individual and combination DNA vaccines for B. anthracis, Ebola virus, Marburg virus and Venezuelan equine encephalitis virus. Vaccine. 2003; 21:4071-4080.
17. Dye JM, Herbert AS, Kuehne AI, Barth JF, Muhammad MA, Zak SE, Ortiz RA, Prugar LI, Pratt WD. Postexposure antibody prophylaxis protects nonhuman primates from filovirus disease. Proc Natl Acad Sci U S A. 2012; 109:5034-5039.
18. Porter DP, Weidner JM, Gomba L, *et al*. Remdesivir (GS-5734) Is Efficacious in Cynomolgus Macaques Infected With Marburg Virus. J Infect Dis. 2020; 222:1894-1901.
19. Bixler SL, Bocan TM, Wells J, *et al*. Efficacy of favipiravir (T-705) in nonhuman primates infected with Ebola virus or Marburg virus. Antiviral Res. 2018; 151:97-104.
20. Zhu W, Zhang Z, He S, Wong G, Banadyga L, Qiu X. Successful treatment of Marburg virus with orally administrated T-705 (Favipiravir) in a mouse model. Antiviral Res. 2018; 151:39-49.
21. Warren TK, Whitehouse CA, Wells J, Welch L, Charleston JS, Heald A, Nichols DK, Mattix ME, Palacios G, Kugleman JR, Iversen PL, Bavari S. Delayed Time-to-Treatment of an Antisense Morpholino Oligomer Is Effective against Lethal Marburg Virus Infection in Cynomolgus Macaques. PLoS Negl Trop Dis. 2016; 10:e0004456.
22. Heald AE, Iversen PL, Saoud JB, Sazani P, Charleston JS, Axtelle T, Wong M, Smith WB, Vutikullird A, Kaye E. Safety and pharmacokinetic profiles of phosphorodiamidate morpholino oligomers with activity against ebola virus and marburg virus: results of two single-ascending-dose studies. Antimicrob Agents Chemother. 2014; 58:6639-6647.
23. Heald AE, Charleston JS, Iversen PL, *et al*. AVI-7288 for Marburg Virus in Nonhuman Primates and Humans. N Engl J Med. 2015; 373:339-348.
24. Thi EP, Mire CE, Ursic-Bedoya R, Geisbert JB, Lee ACH, Agans KN, Robbins M, Deer DJ, Fenton KA, MacLachlan I, Geisbert TW. Marburg virus infection in nonhuman primates: Therapeutic treatment by lipid-encapsulated siRNA. Sci Transl Med. 2014; 6:250ra116.
25. King LB, Fusco ML, Flyak AI, Ilinykh PA, Huang K, Gunn B, Kirchdoerfer RN, Hastie KM, Sangha AK, Meiler J, Alter G, Bukreyev A, Crowe JE, Jr., Saphire

EO. The Marburgvirus-Neutralizing Human Monoclonal Antibody MR191 Targets a Conserved Site to Block Virus Receptor Binding. Cell Host Microbe. 2018; 23:101-109 e104.
26. Mire CE, Geisbert JB, Borisevich V, *et al*. Therapeutic treatment of Marburg and Ravn virus infection in nonhuman primates with a human monoclonal antibody. Sci Transl Med. 2017; 9.
27. Kortepeter MG, Dierberg K, Shenoy ES, Cieslak TJ, Medical Countermeasures Working Group of the National Ebola T, Education Center's Special Pathogens Research N. Marburg virus disease: A summary for clinicians. Int J Infect Dis. 2020; 99:233-242.

Received July 22, 2022; Revised July 27, 2022; Accepted July 29, 2022.

[§]These authors contributed equally to this work.
**Address correspondence to:*
Hongzhou Lu, Department of Infectious Diseases, National Clinical Research Center for Infectious Diseases, The Third People's Hospital of Shenzhen, Shenzhen, Guangdong Province 518112, China.
E-mail: luhongzhou@fudan.edu.cn

Released online in J-STAGE as advance publication July 31, 2022.

BST
BioScience Trends

Guide for Authors

1. Scope of Articles

BioScience Trends (Print ISSN 1881-7815, Online ISSN 1881-7823) is an international peer-reviewed journal. *BioScience Trends* devotes to publishing the latest and most exciting advances in scientific research. Articles cover fields of life science such as biochemistry, molecular biology, clinical research, public health, medical care system, and social science in order to encourage cooperation and exchange among scientists and clinical researchers.

2. Submission Types

Original Articles should be well-documented, novel, and significant to the field as a whole. An Original Article should be arranged into the following sections: Title page, Abstract, Introduction, Materials and Methods, Results, Discussion, Acknowledgments, and References. Original articles should not exceed 5,000 words in length (excluding references) and should be limited to a maximum of 50 references. Articles may contain a maximum of 10 figures and/or tables. Supplementary Data are permitted but should be limited to information that is not essential to the general understanding of the research presented in the main text, such as unaltered blots and source data as well as other file types.

Brief Reports definitively documenting either experimental results or informative clinical observations will be considered for publication in this category. Brief Reports are not intended for publication of incomplete or preliminary findings. Brief Reports should not exceed 3,000 words in length (excluding references) and should be limited to a maximum of 4 figures and/or tables and 30 references. A Brief Report contains the same sections as an Original Article, but the Results and Discussion sections should be combined.

Reviews should present a full and up-to-date account of recent developments within an area of research. Normally, reviews should not exceed 8,000 words in length (excluding references) and should be limited to a maximum of 10 figures and/or tables and 100 references. Mini reviews are also accepted, which should not exceed 4,000 words in length (excluding references) and should be limited to a maximum of 5 figures and/or tables and 50 references.

Policy Forum articles discuss research and policy issues in areas related to life science such as public health, the medical care system, and social science and may address governmental issues at district, national, and international levels of discourse. Policy Forum articles should not exceed 3,000 words in length (excluding references) and should be limited to a maximum of 5 figures and/or tables and 30 references.

Communications are short, timely pieces that spotlight new research findings or policy issues of interest to the field of global health and medical practice that are of immediate importance. Depending on their content, Communications will be published as "Comments" or "Correspondence". Communications should not exceed 1,500 words in length (excluding references) and should be limited to a maximum of 2 figures and/or tables and 20 references.

Editorials are short, invited opinion pieces that discuss an issue of immediate importance to the fields of global health, medical practice, and basic science oriented for clinical application. Editorials should not exceed 1,000 words in length (excluding references) and should be limited to a maximum of 10 references. Editorials may contain one figure or table.

News articles should report the latest events in health sciences and medical research from around the world. News should not exceed 500 words in length.

Letters should present considered opinions in response to articles published in *BioScience Trends* in the last 6 months or issues of general interest. Letters should not exceed 800 words in length and may contain a maximum of 10 references. Letters may contain one figure or table.

3. Editorial Policies

For publishing and ethical standards, BioScience Trends follows the Recommendations for the Conduct, Reporting, Editing, and Publication of Scholarly Work in Medical Journals (*http://www.icmje.org/recommendations*) issued by the International Committee of Medical Journal Editors (ICMJE), and the Principles of Transparency and Best Practice in Scholarly Publishing (*https://doaj.org/bestpractice*) jointly issued by the Committee on Publication Ethics (COPE), the Directory of Open Access Journals (DOAJ), the Open Access Scholarly Publishers Association (OASPA), and the World Association of Medical Editors (WAME).

BioScience Trends will perform an especially prompt review to encourage innovative work. All original research will be subjected to a rigorous standard of peer review and will be edited by experienced copy editors to the highest standards.

Ethics: *BioScience Trends* requires that authors of reports of investigations in humans or animals indicate that those studies were formally approved by a relevant ethics committee or review board. For research involving human experiments, a statement that the participants gave informed consent before taking part (or a statement that it was not required and why) should be indicated. Authors should also state that the study conformed to the provisions of the Declaration of Helsinki (as revised in 2013). When reporting experiments on animals, authors should indicate whether the institutional and national guide for the care and use of laboratory animals was followed.

Conflict of Interest: All authors are required to disclose any actual or potential conflict of interest including financial interests or relationships with other people or organizations that might raise questions of bias in the work reported. If no conflict of interest exists for each author, please state "There is no conflict of interest to disclose".

Submission Declaration: When a manuscript is considered for submission to *BioScience Trends*, the authors should confirm that 1) no part of this manuscript is currently under consideration for publication elsewhere; 2) this manuscript does not contain the same information in whole or in part as manuscripts that have been published, accepted, or are under review elsewhere, except in the form of an abstract, a letter to

the editor, or part of a published lecture or academic thesis; 3) authorization for publication has been obtained from the authors' employer or institution; and 4) all contributing authors have agreed to submit this manuscript.

Cover Letter: The manuscript must be accompanied by a cover letter prepared by the corresponding author on behalf of all authors. The letter should indicate the basic findings of the work and their significance. The letter should also include a statement affirming that all authors concur with the submission and that the material submitted for publication has not been published previously or is not under consideration for publication elsewhere. The cover letter should be submitted in PDF format. For example of Cover Letter, please visit: Download Centre (*https://ircabssagroup.com/downcentre*).

Copyright: When a manuscript is accepted for publication in *BioScience Trends*, the transfer of copyright is necessary. A JOURNAL PUBLISHING AGREEMENT (JPA) form will be e-mailed to the authors by the Editorial Office and must be returned by the authors as a scan. Only forms with a hand-written signature are accepted. This copyright will ensure the widest possible dissemination of information. Please note that your manuscript will not proceed to the next step in publication until the JPA Form is received. In addition, if excerpts from other copyrighted works are included, the author(s) must obtain written permission from the copyright owners and credit the source(s) in the article.

Peer Review: *BioScience Trends* uses single-blind peer review, which means that reviewers know the names of the authors, but the authors do not know who reviewed their manuscript. The external peer review is performed for research articles by at least two reviewers, and sometimes the opinions of more reviewers are sought. Peer reviewers are selected based on their expertise and ability to provide high quality, constructive, and fair reviews. For research manuscripts, the editors may, in addition, seek the opinion of a statistical reviewer. Consideration for publication is based on the article's originality, novelty, and scientific soundness, and the appropriateness of its analysis.

Suggested Reviewers: A list of up to 3 reviewers who are qualified to assess the scientific merit of the study is welcomed. Reviewer information including names, affiliations, addresses, and e-mail should be provided at the same time the manuscript is submitted online. Please do not suggest reviewers with known conflicts of interest, including participants or anyone with a stake in the proposed research; anyone from the same institution; former students, advisors, or research collaborators (within the last three years); or close personal contacts. Please note that the Editor-in-Chief may accept one or more of the proposed reviewers or may request a review by other qualified persons.

Language Editing: Manuscripts prepared by authors whose native language is not English should have their work proofread by a native English speaker before submission. If not, this might delay the publication of your manuscript in *BioScience Trends*.

The Editing Support Organization can provide English proofreading, Japanese-English translation, and Chinese-English translation services to authors who want to publish in *BioScience Trends* and need assistance before submitting a manuscript. Authors can visit this organization directly at *http://www.iacmhr.com/iac-eso/support.php?lang=en*. IAC-ESO was established to facilitate manuscript preparation by researchers whose native language is not English and to help edit works intended for international academic journals.

4. Manuscript Preparation

Manuscripts are suggested to be prepared in accordance with the "Recommendations for the Conduct, Reporting, Editing, and Publication of Scholarly Work in Medical Journals", as presented at *http://www.ICMJE.org*.

Manuscripts should be written in clear, grammatically correct English and submitted as a Microsoft Word file in a single-column format. Manuscripts must be paginated and typed in 12-point Times New Roman font with 24-point line spacing. Please do not embed figures in the text. Abbreviations should be used as little as possible and should be explained at first mention unless the term is a well-known abbreviation (*e.g.* DNA). Single words should not be abbreviated.

Title page: The title page must include 1) the title of the paper (Please note the title should be short, informative, and contain the major key words); 2) full name(s) and affiliation(s) of the author(s), 3) abbreviated names of the author(s), 4) full name, mailing address, telephone/fax numbers, and e-mail address of the corresponding author; and 5) conflicts of interest (if you have an actual or potential conflict of interest to disclose, it must be included as a footnote on the title page of the manuscript; if no conflict of interest exists for each author, please state "There is no conflict of interest to disclose"). Please visit Download Centre and refer to the title page of the manuscript sample.

Abstract: The abstract should briefly state the purpose of the study, methods, main findings, and conclusions. For articles that are Original Articles, Brief Reports, Reviews, or Policy Forum articles, a one-paragraph abstract consisting of no more than 250 words must be included in the manuscript. For Communications, Editorials, News, or Letters, a brief summary of main content in 150 words or fewer should be included in the manuscript. Abbreviations must be kept to a minimum and non-standard abbreviations explained in brackets at first mention. References should be avoided in the abstract. Three to six key words or phrases that do not occur in the title should be included in the Abstract page.

Introduction: The introduction should be a concise statement of the basis for the study and its scientific context.

Materials and Methods: The description should be brief but with sufficient detail to enable others to reproduce the experiments. Procedures that have been published previously should not be described in detail but appropriate references should simply be cited. Only new and significant modifications of previously published procedures require complete description. Names of products and manufacturers with their locations (city and state/country) should be given and sources of animals and cell lines should always be indicated. All clinical investigations must have been conducted in accordance with Declaration of Helsinki principles. All human and animal studies must have been approved by the appropriate institutional review board(s) and a specific declaration of approval must be made within this section.

Results: The description of the experimental results should be succinct but in sufficient detail to allow the experiments to be analyzed and interpreted by an independent reader. If necessary, subheadings may be used for an orderly presentation. All figures and tables must be referred to in the text.

Discussion: The data should be interpreted concisely without repeating material already presented in the Results section. Speculation is permissible, but it must be well-founded, and discussion of the wider implications of the findings is encouraged. Conclusions derived from the study should be included in this section.

Acknowledgments: All funding sources should be credited in the Acknowledgments section. In addition, people who contributed to the work but who do not meet the criteria for authors should be listed along with their contributions.

References: References should be numbered in the order in which they appear in the text. Citing of unpublished results, personal communications, conference abstracts, and theses in the reference list is not recommended but these sources may be mentioned in the text. In the reference list, cite the names of all authors when there are fifteen or fewer authors; if there are sixteen or more authors, list the first three followed by *et al*. Names of journals should be abbreviated in the style used in PubMed. Authors are responsible for the accuracy of the references. The EndNote Style of *BioScience Trends* could be downloaded at **EndNote** (*https://ircabssagroup.com/examples/BioScience_Trends.ens*).

Examples are given below:

Example 1 (Sample journal reference):

Inagaki Y, Tang W, Zhang L, Du GH, Xu WF, Kokudo N. Novel aminopeptidase N (APN/CD13) inhibitor 24F can suppress invasion of hepatocellular carcinoma cells as well as angiogenesis. Biosci Trends. 2010; 4:56-60.

Example 2 (Sample journal reference with more than 15 authors):

Darby S, Hill D, Auvinen A, *et al*. Radon in homes and risk of lung cancer: Collaborative analysis of individual data from 13 European case-control studies. BMJ. 2005; 330:223.

Example 3 (Sample book reference):

Shalev AY. Post-traumatic stress disorder: Diagnosis, history and life course. In: Post-traumatic Stress Disorder, Diagnosis, Management and Treatment (Nutt DJ, Davidson JR, Zohar J, eds.). Martin Dunitz, London, UK, 2000; pp. 1-15.

Example 4 (Sample web page reference):

World Health Organization. The World Health Report 2008 – primary health care: Now more than ever. *http://www.who.int/whr/2008/whr08_en.pdf* (accessed September 23, 2010).

Tables: All tables should be prepared in Microsoft Word or Excel and should be arranged at the end of the manuscript after the References section. Please note that tables should not in image format. All tables should have a concise title and should be numbered consecutively with Arabic numerals. If necessary, additional information should be given below the table.

Figure Legend: The figure legend should be typed on a separate page of the main manuscript and should include a short title and explanation. The legend should be concise but comprehensive and should be understood without referring to the text. Symbols used in figures must be explained. Any individually labeled figure parts or panels (A, B, *etc*.) should be specifically described by part name within the legend.

Figure Preparation: All figures should be clear and cited in numerical order in the text. Figures must fit a one- or two-column format on the journal page: 8.3 cm (3.3 in.) wide for a single column, 17.3 cm (6.8 in.) wide for a double column; maximum height: 24.0 cm (9.5 in.). Please make sure that the symbols and numbers appeared in the figures should be clear. Please make sure that artwork files are in an acceptable format (TIFF or JPEG) at minimum resolution (600 dpi for illustrations, graphs, and annotated artwork, and 300 dpi for micrographs and photographs). Please provide all figures as separate files. Please note that low-resolution images are one of the leading causes of article resubmission and schedule delays.

Units and Symbols: Units and symbols conforming to the International System of Units (SI) should be used for physicochemical quantities. Solidus notation (*e.g*. mg/kg, mg/mL, mol/mm^2/min) should be used. Please refer to the SI Guide *www.bipm.org/en/si/* for standard units.

Supplemental data: Supplemental data might be useful for supporting and enhancing your scientific research and *BioScience Trends* accepts the submission of these materials which will be only published online alongside the electronic version of your article. Supplemental files (figures, tables, and other text materials) should be prepared according to the above guidelines, numbered in Arabic numerals (*e.g.*, Figure S1, Figure S2, and Table S1, Table S2) and referred to in the text. All figures and tables should have titles and legends. All figure legends, tables and supplemental text materials should be placed at the end of the paper. Please note all of these supplemental data should be provided at the time of initial submission and note that the editors reserve the right to limit the size and length of Supplemental Data.

5. Submission Checklist

The Submission Checklist will be useful during the final checking of a manuscript prior to sending it to *BioScience Trends* for review. Please visit Download Centre and download the Submission Checklist file.

6. Online Submission

Manuscripts should be submitted to *BioScience Trends* online at *http://www.biosciencetrends.com*. The manuscript file should be smaller than 5 MB in size. If for any reason you are unable to submit a file online, please contact the Editorial Office by e-mail at *office@biosciencetrends.com*

7. Accepted Manuscripts

Proofs: Galley proofs in PDF format will be sent to the corresponding author *via* e-mail. Corrections must be returned

to the editor (*proof-editing@biosciencetrends.com*) within 3 working days.

Offprints: Authors will be provided with electronic offprints of their article. Paper offprints can be ordered at prices quoted on the order form that accompanies the proofs.

Page Charge: Page charges will be levied on all manuscripts accepted for publication in *BioScience Trends* (Original Articles / Brief Reports / Reviews / Policy Forum / Communications: $140 per page for black white pages, $340 per page for color pages; News / Letters: a total cost of $600). Under exceptional circumstances, the author(s) may apply to the editorial office for a waiver of the publication charges at the time of submission.

Misconduct: *BioScience Trends* takes seriously all allegations of potential misconduct and adhere to the ICMJE Guideline (*http://www.icmje.org/recommendations*) and COPE Guideline (*http://publicationethics.org/files/Code_of_conduct_for_journal_editors.pdf*). In cases of suspected research or publication misconduct, it may be necessary for the Editor or Publisher to contact and share submission details with third parties including authors' institutions and ethics committees. The corrections, retractions, or editorial expressions of concern will be performed in line with above guidelines.

(As of February 2022)

BioScience Trends
Editorial and Head Office
Pearl City Koishikawa 603,
2-4-5 Kasuga, Bunkyo-ku,
Tokyo 112-0003, Japan.
E-mail: office@biosciencetrends.com